Master's Thesis

Quantitative Analysis of Flame Kinematics in Premixed Hydrogen-Air-DNG Jet Flames using PIV Measurements and Flame Front Segmentation

An Experimental Study

Ergin Cem Günçe

Delft University of Technology

Master's Thesis

Quantitative Analysis of Flame Kinematics in Premixed Hydrogen-Air-DNG Jet Flames using PIV Measurements and Flame Front Segmentation

by

Ergin Cem Günçe

Student Number 5281245

to obtain the degree of Master of Science
at the Delft University of Technology,
to be defended publicly on Friday January 26, 2024 at 10:00 AM.

Department:	Process and Energy
Faculty:	Mechanical Engineering, 3mE
University:	Delft University of Technology

Prof. Sikke Klein:	Supervisor (Chair)
Dr. Mark Tummers :	Supervisor
Dr. Gerrit Elsinga :	Examiner
Ir. Luuk Altenburg :	Daily Supervisor

TU Delft

‘Zafer, “Zafer benimdir” diyebilenindir. Başarı ise, “Başaracağım” diye başlayarak sonunda “Başardım” diyebilenindir.’

(Victory is for those who can say ”Victory is mine”. Success is for those who can begin saying ”I will succeed” and say ”I have succeeded” in the end.)

M. Kemal Atatürk
(1881 - ∞)

Acknowledgements

Fore and foremost, throughout my journey at TU Delft, I would like to start by thanking my supervisor, Sikke Klein, for supporting me throughout my internship. You provided me with the opportunity to become a teaching assistant in the turbomachinery course and involved me in this master's thesis project. During my master's project, I had the opportunity to collaborate with my supervisor Mark Tummers as well. Your in-depth understanding and style of discussion will be unforgettable to me. To my supervisors, I will always appreciate the time, effort and patience you have shown towards me. I am grateful for the guidance and insights you have provided, which greatly enhanced my understanding and skills. During my project, I spent weeks and months with Luuk inside the PIV combustion lab. I strongly believe that we created a relationship that goes beyond that of a PhD mentor and student. I also learned a lot from you, and our conversations about football, life, politics, watches and many others will be unforgettable. Throughout the course of my project, I was fortunate to receive invaluable assistance from both Bart and Edwin. Your expertise and willingness to help played a crucial role in my journey. I also seized the opportunity to work as a teaching assistant, which allowed me to collaborate with Rene Pecnik and Teja Donepudi. Working with you both was not only a learning experience but also a privilege.

I would also like to extend my heartfelt thanks to my friends who have become my family here in Delft. To Sinan, Yaren Jr., büyük Yaren, Göktürk, Mert, Arda, Hazal, Eren, Doruk, Irmak, Gökberk, Zeynep, Sezgi, Kostas, Filotas, Dimitris, Kaan, Dilay, Yasemin, Rolf, Hilal, Asuman, Alican: your companionship, support, and friendship have been invaluable to me. Each of you has contributed uniquely to my journey, making my time here not just educational, but also cheerful and fulfilling. I am deeply grateful for the moments we shared, the challenges we overcame together, and the memories we created. I would also like to express my heartfelt thanks to my friends in Turkey – Özgür, Cağdaş, Alperen, Alp, Uğur, Emre, Alimert, and Melike. Your belief in me and my goals has been invaluable, and I am deeply grateful for your unwavering friendship. Thank you for being an essential part of my life, no matter the distance.

To Serpil, Mehmet, Bulut, Berk, Barış, Pelin, Dilara, and to Zekai, Gülten, Zehra, Gülseren - my proud and lovely family, who have shown me immense kindness and support. I am profoundly grateful for having each one of you. Your warmth, guidance, and unwavering belief in me have been sources of great strength and encouragement. To my beloved parents, Sevil and Dadal Günçe, words fall short when I try to express my deepest gratitude for all that you have done for me. Your unwavering faith in me, even in the face of challenges, has been the foundation upon which I have built my dreams. Your wisdom, kindness, and strength are the greatest gifts I could have ever received. Thank you for your endless love.

Ergin Cem Günçe
Delft, January 2024

Summary

Today's electricity supply falls short of current demands, leading to the utilization of gas turbines in both ground based and avionic infrastructures. Nevertheless, these often rely on carbon-based fuels, resulting in escalating CO2 emissions. However, adopting hydrogen as a fuel eliminates carbon emissions. Aside from zero carbon emissions, hydrogen has a higher energy density by weight compared to conventional fuels. This makes it an distinct option for applications requiring efficient energy storage and delivery. Due to its wide flammability range and low ignition energy, hydrogen can combust in scenarios where traditional fuels might not. This unique characteristic, while advantageous in certain contexts, requires detailed study to ensure safe and efficient combustion in gas turbines. However, the combustion of hydrogen inherently results in elevated flame temperatures, thereby generating increased NOx levels. Furthermore, hydrogen's high mass diffusivity translates to a reduced Lewis number. Consequently, it becomes vital to grasp the local dynamic characteristics of the flames, particularly at stable and flashback points. Understanding the thermo-physical behavior of hydrogen flames, especially at stable and flashback points, therefore, requires experimental studies to reflect real life complexities. These tools can offer insights into turbulence-flame interactions, flame stabilization, and emission formation mechanisms.

In this research, an exploration was undertaken to understand the local kinematics and dynamics of Hydrogen and DNG flames, with emphasis on stable states and those approaching flashback conditions. Particle Image Velocimetry (PIV) experiments were employed on a Bunsen burner setup, facilitating the capture of the jet flames' velocity fields. Both low-speed and high-speed recordings were captured by high-speed camera, providing distinct insights into flame dynamics. Flame front detection was achieved using Mie-scattering, capitalizing on the differential seeding particle densities between the unburnt and burnt regions. Intensity differences between these regions were meticulously captured with a bilateral filter, leading to the successful extraction of the flame front. This extracted front was subsequently distinguished via segmentation and superimposed onto the velocity field. Low-speed recordings offered a generalized perspective on flame turbulence characteristics through cold flow validation, while high-speed recordings unveiled specific dynamics, inclusive of flame curvature, local flame and displacement speeds, and both normal and tangential velocities and stretches. It consistently holds the 1-D unstretched flame speed, even as the Reynolds number increases, aligning with the respective flashback points and stable conditions of the flames. As a result, in-depth comparison of DNG and H_2 fuels in terms of flame dynamics and kinematics were discerned.

Contents

List of Figures

List of Tables

Nomenclature

Abbreviations

Abbreviation	**Meaning**
PIV	Particle Image Velocimetry
DNG	Dutch Natural Gas Flame
H2	Hydrogen Flame
OH-PLIF	OH-Planar Laser Induced Fluorescence
SCN	Slope Change Notation
RMS	Root Mean Square
STP	Standard Temperature and Pressure

Non-Dimensional Numbers

Number	**Meaning**
Re	Reynolds Number
Le	Lewis Number
Ka	Karlovitz Number
Da	Damköhler Number
Ma	Markstein Number

Symbols

u_i	fluid velocity vector in the ith direction	[m/s]
u_j	fluid velocity vector in the jth direction	[m/s]
ρ	Density	[kg/m^3]
p	Pressure	[Pa] or [N/m^2]
τ_{ij}	force due to viscosity	[N/m2]
H	total enthalpy	[J]
$\overline{u}_i$	average velocity of fluid particles	[m/s]
u_i'	fluctuating velocity	[m/s]
ϵ	viscous dissipation	[m$^2/s^3$]
ν	Kinematic Viscosity	[m$^2/s$]
u_0	Integral velocity scale	[m/s]
l_0	Integral length scale	[m]
η	Kolmogorov length scale	[m]
τ_η	Kolmogorov time scale	[1/s]
u_η	Kolmogorov velocity scale	[m/s]

u_i	fluid velocity vector in the ith direction	[m/s]
$Re = \frac{u_0 l_0}{\nu}$	Integral Reynolds number	[-]
k_e	Total Turbulent Kinetic Energy	[kg m$^2/s^2$]
k'	Specific Turbulent Kinetic Energy	[m$^2/s^2$]
k	Wave number	[1/m]
ρ	Density	[kg/m^3]
ϕ	Equivalence Ratio	-
Y_i	mass fraction of the i-th species	-
D_i	binary diffusion coefficient for the i-th species	[m$^2/s$]
R_i	production rate for the i-th species	[kg/(m$^3 \cdot s$)]
δ_F	laminar flame thickness	[m]
λ_u	thermal conductivity	[W/(m·K)]
c_p	specific heat capacity at constant pressure	[J/(kg·K)]
S_L	laminar flame speed	[m/s]
$v_{n,u}$	unburned mixture's velocity	[m/s]
$S_{L,u}$	laminar flame speed through unburnt region	[m/s]
S_{L0}	unstretched laminar flame speed	[m/s]
v_u	mixture velocity	[m/s]
D	mass diffusivity	m$^2/s$
K	Flame Stretch rate	[1/s]
A	flame surface area	[m^2]
∇_t	Divergence in tangential direction on flame front	[1/s]
$\vec{V} = \vec{V_n} + \vec{V_t}$	Vectoral representation of velocities, normal and tangential	[m/s]
K_{n+t}	Total Stretch Rate	[1/s]
K_n	Stretch Rate in normal direction	[1/s]
K_t	Stretch Rate in tangential direction	[1/s]
κ	flame front curvature	[1/m]
S_f	Local Flame Speed	[m/s]
S_d	Local Flame Displacement Speed	[m/s]
L_M	Markstein length	[m]
$\dot{m}$	mass flow rate	[kg/s]
A_T	Turbulent Flame Surface Area	[m]

u_i	fluid velocity vector in the ith direction	[m/s]
S_T	Turbulent Flame Speed	[m/s]
g_c	critical velocity gradient	[1/s]
$u(\|y = \delta_p)$	Flame Speed at Flame Tip	[m/s]
δ_p	Distance of flame tip to premixed wall	[m]
κ	flame front curvature	[1/m]
S_f	Local Flame Speed	[m/s]
S_d	Local Flame Displacement Speed	[m/s]
Q_u	Total flow rate (sum of air and fuel flow rates)	[m^3/s]
Q_a	Air flow rate	[m^3/s]
Q_f	Fuel flow rate	[m^3/s]
$\dot{m}_u$	Total mass flow rate (sum of air and fuel mass flow rates)	[kg/s]
$\dot{m}_a$	Air mass flow rate	[kg/s]
$\dot{m}_f$	Fuel mass flow rate	[kg/s]
ρ_u	Mixture density	[kg/m^3]
ρ_f	Fuel mixture density	[kg/m^3]
ρ_a	Air density	[kg/m^3]
x_{H_2}	Hydrogen fraction in fuel mixture	[-]
x_{DNG}	Fraction of DNG	[-]
$f_\#$	Lens aperture size; connected to the amount of light passing through the lens	-
f	Focal length of the lens	m
D	Diameter of the lens	m
M	Magnification of the lens	-
y_i	Distance from the image to the lens	m
y_o	Distance from the object to the lens	m
s_i	Image distance from the lens	m
s_o	Object distance from the lens	m
d_g	Diameter of the geometric image formed by the lens	m
d_p	Diameter of the particle being imaged	m
d_s	Diffraction spot size of the geometric image	m
λ	Wavelength of the light used in the imaging system	m
d_{tot}	Total size of the image, incorporating geometric and diffraction spot sizes	m
$I_{\text{filtered}}(p)$	Filtered value of a pixel in a bilateral filter	-

u_i	fluid velocity vector in the ith direction	[m/s]
$g_s(i,j)$	Spatial Gaussian function weight based on pixel distance	-
$g_r(i,j)$	Tonal Gaussian function weight based on intensity values	-
σ_s	Standard deviation of the spatial Gaussian function	-
σ_r	Standard deviation of the tonal Gaussian function	-
$I(p)$	Intensity value of the current pixel	-
$I(q)$	Intensity value of the neighboring pixel	-
$W(p)$	Normalization factor in the bilateral filter	-
wd	Window size in pixels used in the interrogation window for Mie scattering	pixels

1

Introduction

1.1. Background of the research

Rapid global population growth has given rise to an escalating demand for energy. Traditionally, this need has been met through the burning of fossil fuels, industrial processes, and land-use changes, leading to a significant surge in carbon dioxide (CO_2) emissions [65]. The resulting accumulation of CO_2 in the atmosphere is causing profound societal challenges, including global warming, climate change, and severe weather events.Figure 1.1 taken from [23] shows of the global fossil CO_2 emissions until 2018, including their source distribution, geographical emission centers, and the per capita contributions. According to the preliminary estimates, there was a growth of 2.1% in CO_2 emissions between 2017 and 2018, leading to a total of 10.0 ± 0.5 GtC which stands for gigaton of CO_2 to atmosphere . The emissions were dominated by coal (40%), followed by oil (34%), natural gas (20%), and cement production (4%), with other sources contributing a minor 1.3%. On a geographical scale, the majority of CO_2 emissions originated from China (28%), the USA (15%), the EU (9%), and India (7%), cumulatively accounting for 59% of global emissions. The rest of the world contributed to the remaining 41% of the emissions, which included aviation and marine bunker fuels making up 3.4% of the total. Interestingly, per capita CO_2 emissions exhibited a large variation, with the USA showing more than double the per capita emissions of China, nearly triple that of the EU, and nine times greater than that of India [23].

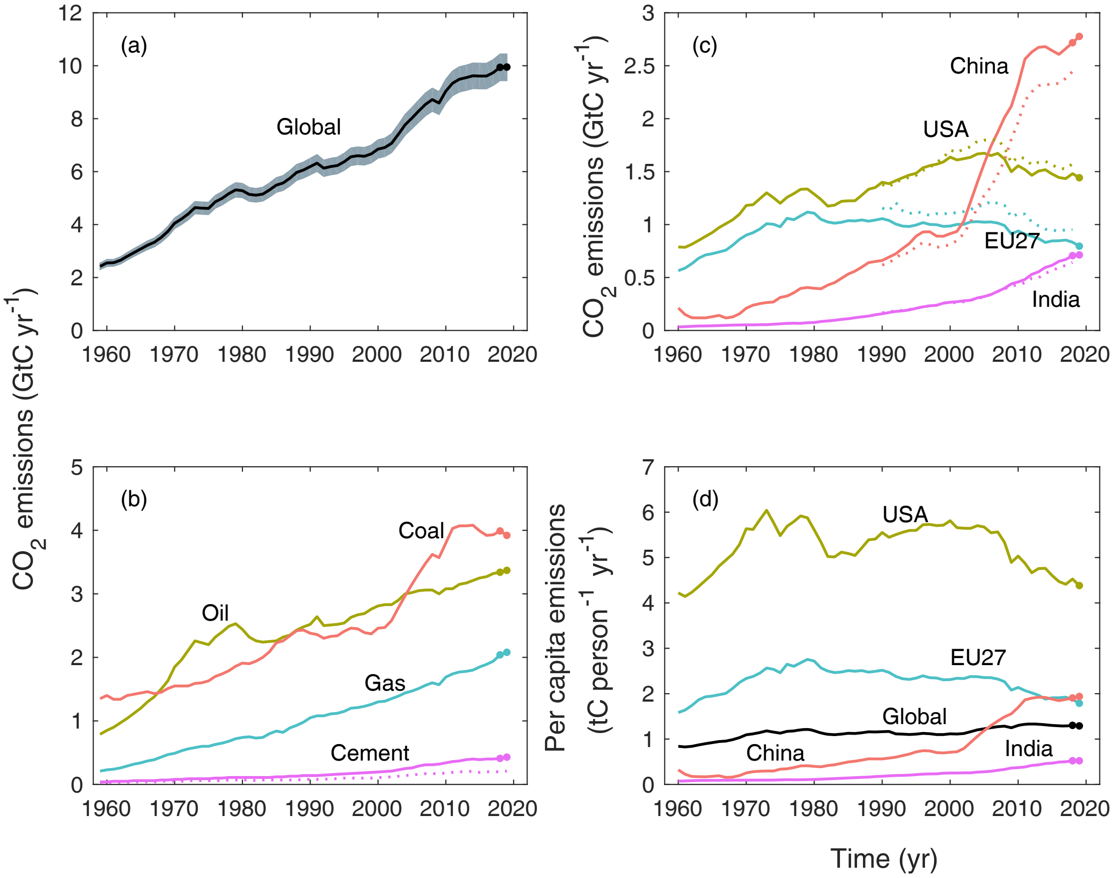

Figure 1.1: Fossil CO$_2$ emissions for (a) the globe, including an uncertainty of ±5% (grey shading), and the emissions extrapolated using BP energy statistics (black dots), (b) global emissions by fuel type, including coal (salmon), oil (olive), gas (turquoise), and cement (purple), and excluding gas flaring, which is small (0.6% in 2013). (c) Territorial (solid lines) and consumption (dashed lines) emissions for the top three country emitters (USA – olive; China – salmon; India – purple) and for the European Union (EU; turquoise for the 28 member states of the EU as of 2012) and (d) per capita emissions for the top three country emitters and the EU (all colours as in panel c) and the world (black),[23].

Given the alarming escalation in global CO$_2$ emissions, as depicted in Figure 1.1, the exploration and deployment of less carbon-intensive energy sources have become an urgent global priority. Among these, hydrogen holds significant promise. As an energy carrier, hydrogen can be used across a broad spectrum of applications, including advanced battery and fuel cell technologies, which transform the energy landscape [25]. Additionally, hydrogen serves as a balance between supply and demand, aiding in the management of intermittent renewable sources like solar and wind power. Hydrogen can also be utilized directly in gas turbines for electricity generation, paving the way for cleaner power technologies. However, despite these advantages, hydrogen combustion can lead to the formation of nitrogen oxides (NOx) under certain conditions, necessitating the development of advanced combustion strategies and emissions control technologies.

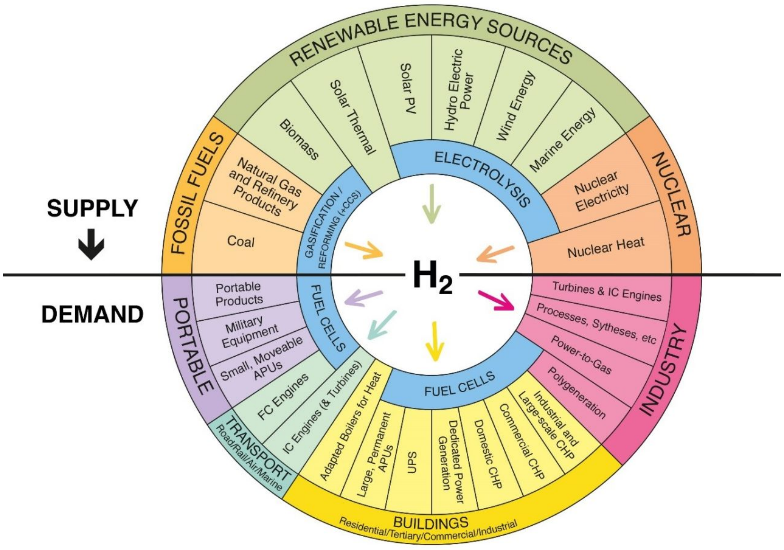

Figure 1.2: Hydrogen primary sources, conversion, applications and sectors [1]

Indeed, the combustion of hydrogen introduces several challenges. For one, hydrogen's high flame speed and low quenching distance can lead to flame flashback [38], leading to potential damage to combustion equipment and compromised safety [15]. Furthermore, due to its wide flammability range and high reactivity, hydrogen combustion can result in unstable flames, which may lead to undesired oscillations in heat release and pressure, causing operational issues and potential failures [64]. Lastly, hydrogen may produce nitrogen oxides (NOx), which is harmful pollutant due to elevated adiabatic flame temperatures. Therefore, the effective reduction of NOx emissions during hydrogen combustion is a critical requirement for its sustainable utilization. Given these challenges, there is a clear necessity for in-depth research in the field of hydrogen combustion [54]. Improved understanding of complex combustion phenomena and development of advanced combustion strategies and emissions control technologies will provide the successful integration of hydrogen into our energy systems. Ultimately, this will contribute to global efforts to mitigate CO_2 emissions and transition towards more sustainable energy solutions [61].

One major concern in gas turbine combustors arising from these characteristics of hydrogen is flashback, especially boundary layer flashback (BLF) [20], [68], [34]. The flame moves away from its intended anchored location and propagates inside the burner, This can significantly compromise the reliability and efficiency of combustion systems. Hence, managing hydrogen and natural gas flames in close to flashback and stable conditions has become a focal point for both academic research and industrial application. 1.3 shows scaled temperature with adiabatic flame temperature during different inlet velocities of lean hydrogen-air flame. Due to the reduced inlet velocities of the hydrogen-air mixture, flame speed becomes more dominant to initiate flashback transitions at $V_{in} = 2.375 m/s$. As seen, flame starts traveling downstream and detaches from the burner tip.

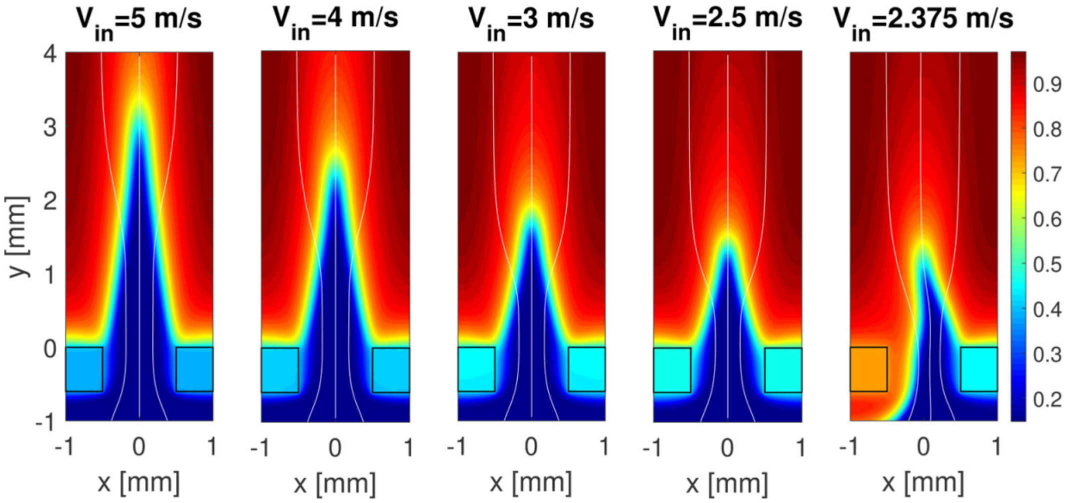

Figure 1.3: Results of normalized adiabatic flame temperature of lean hydrogen-air flame flashback transition due to varying inlet velocity [62].

1.2. Objectives

Combustion processes, fundamentally vital for energy production, have been the subject of extensive research, particularly focusing on hydrogen and Dutch Natural Gas (DNG). Understanding the combustion characteristics of these fuels is the main scope, especially as the global energy sector evolves. The shift towards cleaner and more efficient energy sources has placed hydrogen combustion at the forefront of scientific inquiry. While significant developments have been made in comparing the combustion properties of hydrogen and DNG, much of the existing research has concentrated on broader complexity, dynamics and kinematics. What remains less explored, and forms the central focus of this thesis, is an in-depth comparison of these fuels under the nuanced lens of local flame complexity, dynamics, and kinematics to utilize aspects that govern the stability and efficiency of combustion. Previous investigations on this field, although valuable, have provided limited insights into the local intricacies of flame front behaviors in hydrogen and DNG combustion.

This thesis aims to address several key research questions to provide quantitative analysis of flame kinematics in premixed hydrogen-air-DNG jet flames using PIV measurements and pattern recognition. These research questions include:

1. How do the flame characteristics differ between natural gas and hydrogen under varying conditions, specifically near flashback and stable scenarios, in terms of their dynamics and kinematics?
    (a) How does the local flame speed differ between hydrogen and natural gas flames under stable and near-flashback conditions?
    (b) How do local stretch effects compare between hydrogen and natural gas flames under the different conditions?
    (c) Are there distinct patterns or structures in the flame front for each fuel, especially when approaching flashback or under stable conditions?

1.3. Thesis Outline

This thesis consists of five chapters which explores the quantitative analysis of flame kinematics in premixed hydrogen-air-DNG jet flames using PIV measurements and flame front segmentation. Chapter 2 provides a brief overview on flame-turbulence interaction, covering topics such as turbulent flow, turbulent kinetic energy, laminar and turbulent premixed flames, flame stretch, flame flashback and literature research on flame displacement speed. Chapter 3 focuses on the experimental methodology and flame characterization with flame modelization, detailing the burner setup, flow measurement technique, flame front tracking, image processing technique and the methodology for flame front propagation. Chapter 4 presents the results and discussions, including the analysis of turbulent flow dynamics, turbulent flame characteristics and the quantitative analysis of flame kinematics. Finally, chapter 5, summarizes the findings and discusses potential avenues for future research in the field of hydrogen combustion would be given in chapter 6.

2

Flame-Turbulence Interaction

In the study of premixed flames, it is essential to understand the fundamental fluid mechanics governing the behavior of reacting flows. The basic equations of fluid mechanics are the continuity, momentum, and energy equations which will be discussed in detail. The continuity equation is given by;

$$\frac{\partial}{\partial x_i}\left(\rho u_i\right) = 0, \tag{2.1}$$

as describes conservation of mass. In the equation, ρ denotes the fluid density, u_i is the component of the fluid velocity vector in the x_i direction. The momentum equation is given by;

$$\frac{\partial}{\partial t}\left(\rho u_i\right) + \frac{\partial}{\partial x_j}\left(\rho u_i u_j\right) = -\frac{\partial}{\partial x_i} p + \rho g_i + \frac{\partial}{\partial x_j}\left(\tau_{ij}\right) \tag{2.2}$$

In this equation, p is the pressure, g_i is the component of gravitational acceleration ,n x_i direction and τ_{ij} is the viscous stress tensor and it is given by;

$$\tau_{ij} = \mu(\frac{\partial u_i}{\partial x_j} + \frac{\partial u_j}{\partial x_i}) \tag{2.3}$$

where μ represents dynamic viscosity of the fluid. Upon examining momentum conservation, it's clear that fluid element interactions are dictated not just by their momentum but also by the transport of their energy.

$$\frac{\partial}{\partial t}\left(\rho H\right) + \frac{\partial}{\partial x_j}\left(\rho H u_j\right) = -\frac{\partial q_i}{\partial x_i} + \frac{\partial}{\partial x_j}\left(u_i \tau_{ij}\right) \tag{2.4}$$

The equation above describes the conservation of enthalpy [55]. Here, q_i is the heat flux in the x_i direction. Symbol H represents the specific enthalpy (total enthalpy) where it includes chemical and sensible enthalpy. More specifically, $H_t = h + (v^2/2)$ where h is the static enthalpy and $(v^2/2)$ represents the kinetic energy per unit mass.

2.1. Reynolds and Favre Averaging in Turbulent Flows

In fluid dynamics, especially when dealing with turbulent flows, it is often necessary to employ averaging techniques to spit up an instantaneous quantity into a mean and a fluctuating component. These techniques help in simplifying the complex, chaotic nature of turbulence to make it more analyzable. There are 2 common averaging methods called Reynolds and Favre averaging. Reynolds averaging is typically used for incompressible flows where density variations are small enough to be negligible. The Reynolds averaging of a flow variable ϕ decomposes it into its mean and fluctuating components:

$$\phi = \overline{\phi} + \phi', \tag{2.5}$$

where equation represents the Reynolds decomposition. In this equation, $\overline{\phi}$ is the Reynolds averaged (time-averaged) mean of the variable, defined as $\overline{\phi} = \frac{1}{T}\int_0^T \phi(t)\,dt$, where T is the averaging period and ϕ' is the fluctuating component of ϕ, representing the instantaneous deviation from the mean. For compressible flows with density variations, Favre averaging method is useful because of the fact that method captures the density-weighted averaging process. In combustion, with its significant density changes, makes Reynolds averaging less appropriate. Thus, Favre averaging may expressed as:

$$\phi = \tilde{\phi} + \phi'', \tag{2.6}$$

where $\tilde{\phi}$ is the Favre averaged (density-weighted averaged) mean of the variable, defined as $\tilde{\phi} = \overline{\rho\phi}/\overline{\rho}$, $\overline{\rho\phi}$ is the Reynolds average of the product of density ρ and ϕ, $\overline{\rho}$ is the Reynolds average of the density ρ and last term ϕ'' represents the fluctuating component in Favre averaging, representing the deviation of ϕ from its Favre average. The Favre-averaged momentum equation reads;

$$\frac{\partial}{\partial t}\left(\overline{\rho}\widetilde{u_i}\right) + \frac{\partial}{\partial x_j}\left(\overline{\rho}\widetilde{u_i}\widetilde{u_j} + \overline{\rho u_i' u'j}\right) = -\frac{\partial}{\partial x_i}\overline{p} + \frac{\partial}{\partial x_j}\left(\overline{\tau_{ij}}\right) + \overline{\rho} g_i + S_i \tag{2.7}$$

In the presented equation, the term $\widetilde{u_i}$ depicts the Favre-averaged velocity in the x_i direction, S_i represents the source term includes various factors such as body forces, chemical reactions or heat transfer. For the turbulent flow, following term which will be further referred in results section called turbulence intensity which plays role to characterize turbulent flows, as it quantifies the relative magnitude of the turbulent fluctuations compared to the mean flow. It is typically expressed as a dimensionless quantity and can be calculated using the root-mean-square (RMS) of the fluctuating velocity components (u_i') and the mean velocity components ($\overline{u_i}$) in the flow. Mathematically, the turbulence intensity can be defined as;

$$I = \sqrt{\frac{\overline{u_i'^2}}{\overline{u_i^2}}} \times 100\% \tag{2.8}$$

In this equation, I represents the turbulent intensity where it consists of a numerator represents the RMS of the fluctuating velocity components, while the denominator represents the mean velocity components. Conversely, lower turbulence intensity values suggest that the mean flow dominates, with reduced turbulence-related effects.

2.1.1. Turbulent Dissipation and Scales

Turbulence is characterized by the presence of irregular and chaotic fluctuations in velocity and pressure. These fluctuations occur over a wide range of length and time scales but turbulent energy predominantly dissipated at smallest scales of eddies. This energy dissipation is represented by the symbol ϵ, indicating the rate at which turbulent kinetic energy is transformed into thermal energy [45]. Mathematically, the turbulent dissipation rate can be expressed as follows:

$$\epsilon = 2\nu\overline{\left(\frac{\partial u_i'}{\partial x_j}\right)\left(\frac{\partial u_i'}{\partial x_j}\right)}, \tag{2.9}$$

where equation above emphasizes that sums of the squared gradients of the velocity fluctuations in all spatial directions, scaled by the kinematic viscosity (ν), and averaged. It arises from the consideration of how turbulent kinetic energy cascades from larger to smaller scales in the flow, and how this energy is produced by large scales and dissipated at the smallest scales. For turbulent flows, the assumption that the production of turbulence scales with the dissipation is commonly used, especially in local equilibrium where production and dissipation rates are approximately equal. The general expression for the production of turbulence denoted as $P = -\overline{u_i' u_j'} \frac{\partial \overline{u_i}}{\partial x_j}$. Based on dimensional analysis, the dissipation rate may scale with the largest length scale of the turbulent flow denoted as;

$$P \approx \epsilon \sim \frac{u_0^3}{l_0} \tag{2.10}$$

In this equation, u_0 is the characteristic velocity scale (e.g., the root-mean-square of the velocity fluctuations), and l_0 is the characteristic length scale (often taken as the size of the largest turbulent eddies or the integral length scale of the turbulence). This scaling implies that turbulence dissipation is stronger for larger velocity fluctuations and smaller length scales.

Kolmogorov Scale

The Kolmogorov scales are the smallest scales of turbulent flow. These scales include the Kolmogorov length scale (η), which represents the spatial extent of the smallest eddies; the Kolmogorov time scale (τ_η), signifying the duration required for the flow to traverse the Kolmogorov length scale; and the Kolmogorov velocity scale (u_η), indicating the flow velocity at the Kolmogorov length scale. The Kolmogorov scales can be expressed mathematically as follows:

$$\tau_\eta = \left(\frac{\nu}{\epsilon}\right)^{\frac{1}{2}}, \eta = \left(\frac{\nu^3}{\epsilon}\right)^{\frac{1}{4}}, u_\eta = \left(\frac{\epsilon}{\nu}\right)^{\frac{1}{4}}, \tag{2.11}$$

The Reynolds number, derived from the fluid velocity, fluid kinematic viscosity, and a characteristic integral length scale associated with the flow, represents the ratio of inertial forces to viscous forces. By combining the scaling of the integral length scale with the Kolmogorov scales and the Reynolds number, we obtain the following relationships:

$$\frac{t_0}{\tau_\eta} \sim Re^{1/2}, \frac{l_0}{\eta} \sim Re^{3/4}, \frac{u_0}{v_\eta} \sim Re^{1/4}, \tag{2.12}$$

Here, t_0 denotes the integral time scale, l_0 corresponds to the integral length scale, and u_0 represents the integral scale of flow velocity. The integral scale, on the other hand, is the largest scale of turbulent motion, representing the size of the largest eddies present in the flow. It is often associated with the macroscale l_0, a measure of the average size of the energy-containing eddies in the flow.

Turbulent Kinetic Energy

The turbulent kinetic energy (TKE) is associated with the fluctuating velocity components that drive the chaotic motion of turbulent eddies. On the other hand, it is the energy per unit mass associated with eddies in turbulent flow. The TKE can be expressed as:

$$k = \frac{1}{2}\left(\overline{u_i' u_i'}\right), \tag{2.13}$$

Here, u_i' is the fluctuating velocity component of the velocity in x_i direction.

2.1.2. Wall-Bounded Turbulent Flows

Wall-bounded turbulent flows refer to turbulent fluid flows that occur near solid boundaries, such as the flow around an aircraft wing, inside a pipe, or along a riverbed. The presence of solid boundaries significantly affects the characteristics of turbulent flow due to the no-slip condition, which states that the fluid velocity at the wall must be equal to the wall velocity (usually zero). This leads to the formation of a thin region of fluid adjacent to the wall, known as the boundary layer, where the flow is dominated by viscous forces near the wall. In wall-bounded turbulent flows, several distinct regions can be identified based on the relative importance of viscous and inertial forces.

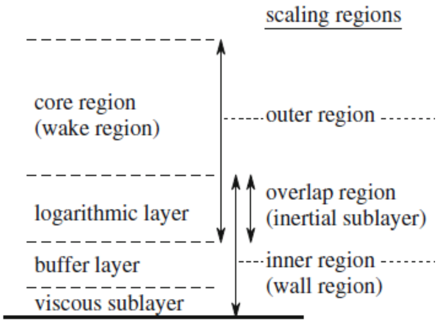

Figure 2.1: Scaling regions of wall-bounded turbulent flow
[45]

As shown in Figure 2.1, the wall-bounded flow regions are distinguished based on the distance from the wall. Additionally, in order to distinguish wall bounded turbulent flow regions, dimensionless parameters and functions can be further utilized. Dimensionless distance from wall can be simplified;

$$y^+ = \frac{\rho u_\tau y}{\mu}, \tag{2.14}$$

and dimensionless velocity of mean flow evaluates:

$$u^+ = \frac{\overline{u}}{u_\tau}, \tag{2.15}$$

where equations both capture dimensionless parameters with additional parameter called friction velocity based on wall shear stress (τ_w), denoted as $u_\tau = \sqrt{\tau_w/\rho}$.

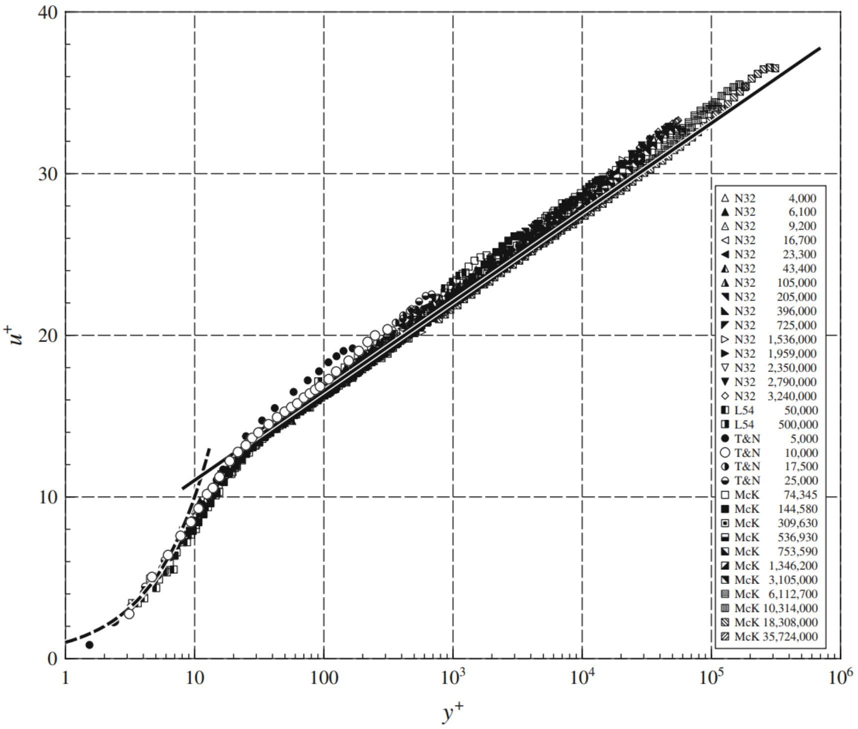

Figure 2.2: Dimensionless mean velocity profile of wall-bounded turbulent flows, [45].

Figure 2.2 presents the relationship between the dimensionless mean velocity profile u^+ and the dimensionless wall distance y^+ in turbulent pipe flow across a range of Reynolds numbers, from 4×10^3 to 36×10^6.

- **Viscous sublayer ($y^+ \leq 5$):** This is the region closest to the wall (typically within a few tens of micrometers), where the flow is predominantly influenced by viscous forces, and the velocity gradients are very high. In this area, the mean velocity characterized by the linear equation $u^+ = y^+$. This equation corresponds to the dashed line (–) in Figure 2.2.
- **Buffer layer ($5 < y^+ < 30$):** This region is located just above the viscous sublayer and is characterized by a balance between viscous and inertial forces. The velocity profile in this region exhibits a more complex behavior, with the influence of both viscous and turbulent stresses.
- **Log-law region (also known as the inertial sublayer ($y^+ > 30$)):** This region is located farther away from the wall and is dominated by inertial forces. The flow in this region follows a logarithmic velocity profile, which is a universal feature of wall-bounded turbulent flows. Equation relies on $u^+ = \frac{1}{K} \ln(y^+) + C^+$, where corresponds to the solid line (-) in Figure 2.2, where (K) is approximately 0.4 (von Kármán constant), and (C^+) is an additive constant varying with wall roughness assuming ($C^+ = 5$) for smooth pipe walls.
- **Core region:** This is the region farthest from the wall, where the effects of the wall are negligible, and the flow characteristics are similar to those of free turbulent flows. The logarithmic law of the wall does not apply at the pipe's centerline, as the derivative of Log-law region is not zero there. In the core region, the mean velocity profile is defined by $u^+ = u_0 - \frac{2}{3} u_\tau \beta \left(1 - \frac{r}{d}\right)^{\frac{3}{2}}$, where u_0 is the centerline velocity, $\beta \approx 0.13$ for the flow in turbulent pipe, and r and d are radial and diameter dimensions of the pipe, respectively.

2.2. Laminar Premixed Flames

Laminar premixed flames are a type of combustion that occurs when a fuel and an oxidizer are mixed together in a laminar flow configuration and ignited. In this configuration, the mixture is uniformly mixed and moves in a smooth, non-turbulent flow. The combustion reaction occurs at the flame front, where the reactants are rapidly consumed and converted into products. Laminar premixed flames are characterized by their distinct flame structure, which includes a thin reaction zone where the reactants are rapidly consumed, a preheat zone where the reactants are heated prior to reaching the reaction zone as seen in Figure 2.3, and an inert zone where the products have already formed. The fact that laminar premixed flames advance in an orderly and foreseeable manner, producing a flame that is relatively stable and constant [39]. Determining the laminar flame speed, which indicates the rate at which the flame propagates through a mixture of fuel and air inside a burner tube, is crucial for capturing the laminar premixed flame definition. Experimental methods, analytical methods, and numerical simulations are several techniques employed to determine the laminar flame speed [40]. Essentially, the flame advances towards the unburned reactants with the magnitude of the flame speed, denoted by s_L, in the direction of the unit normal vector orthogonal to the flame, pointing towards the reactants.

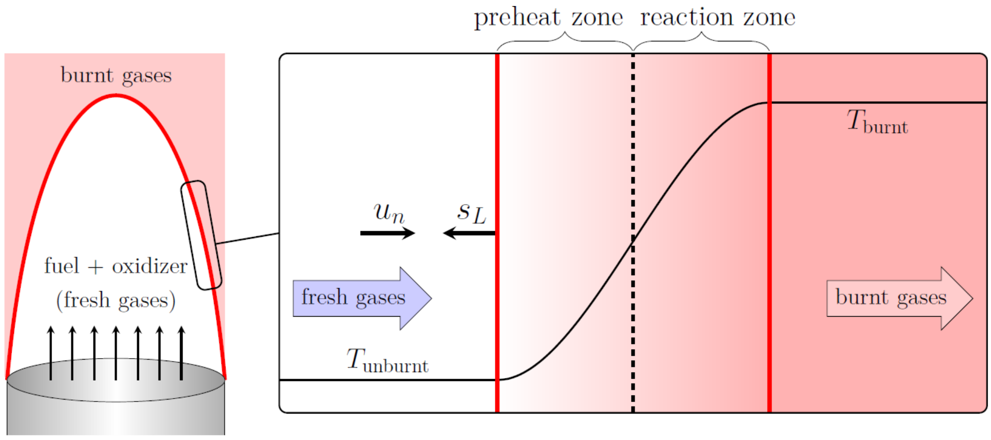

Figure 2.3: Schematic of Laminar Premixed Flames, adopted from [72]

The distinct combustion characteristics of different fuels can be examined by the global chemical reactions of hydrogen and methane when combusted with oxygen. The global reaction for the combustion of hydrogen in air primarily involves hydrogen reacting with oxygen to form water. This reaction can be represented as:

$$2H_2 + O_2 \rightarrow 2H_2O \tag{2.16}$$

This reaction is highly exothermic, releasing significant amounts of energy. Hydrogen flames are characterized by their high flame speed and low ignition energy, making hydrogen a highly reactive fuel. Additionally, the combustion of hydrogen produces water as the primary by-product, making it a clean fuel with respect to carbon emissions. Methane, the simplest hydrocarbon has been considered the main species of DNG fuel, primarily reacts with oxygen to produce carbon dioxide and water, represented by the equation:

$$CH_4 + 2O_2 \rightarrow CO_2 + 2H_2O \tag{2.17}$$

Essentially, methane combustion is a common hydrocarbon combustion, showing a complex reaction pathway compared to hydrogen due to the carbon content. Methane flames typically exhibit slower flame speeds and higher ignition temperatures than hydrogen. In both cases, the amount of heat released significantly influence the flame characteristics, including flame's laminar flame speed (S_L), temperature distribution, and overall structure. Another critical parameter called equivalence ratio while determining the combustion regime of a laminar premixed flame. It quantifies the actual fuel-to-oxidizer mass ratio in a mixture relative to the stoichiometric fuel-to-oxidizer mass ratio. The effects of varying the equivalence ratio can be analyzed in terms of three key regions: lean ($\phi < 1$), stoichiometric ($\phi = 1$), and rich mixtures ($\phi > 1$) [35].

$$\phi = \frac{[\text{Fuel/Air}]}{[\text{Fuel/Air}]_{st}}, \tag{2.18}$$

Where the equation indicates the ratio of fuel and air based on mass flows. Moreover, the equivalence ratio is a key parameter in determining the adiabatic flame temperature and the total heat released during combustion. For the maximum temperature that a flame would reach if no heat were lost to the surroundings called adiabatic flame temperature. Adiabatic flame temperature assumes that all chemical energy of the fuel is converted into thermal energy [35]. Therefore, adiabatic flame temperature depends on how much fuel is used and essentially, adiabatic flame temperature increases as the equivalence ratio increases from a lean to a stoichiometric mixture ($\phi = 1$) as seen in Figure 2.4. This happens because combustion reaction is completed, resulting in a higher amount of heat being released. In a lean mixture, the limited amount of fuel results in incomplete combustion, yielding lower temperatures and less heat release. Conversely, in rich mixtures, though more fuel is available after combustion, the excess fuel remains unburnt due to insufficient oxygen, leading again to a lower flame temperature compared to the stoichiometric case as depicted in Figure 2.4.

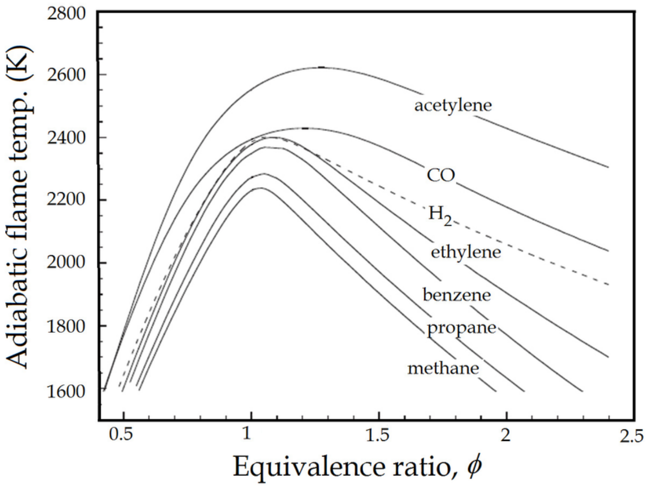

Figure 2.4: Adiabatic flame temperature with different fuels based on equivalence ratio variation, adopted from [35]

For most hydrocarbon fuels, combustion involves a complex network of elementary reactions that include fuel decomposition, oxidation, and the formation of intermediate and final products. The intricate interactions between these reactions, combined with the effects of transport phenomena result in the overall flame structure and heat release pattern.

$$\frac{\partial \rho Y_i}{\partial t} + \nabla \cdot (\rho Y_i \mathbf{u}) = \nabla \cdot (\rho D_i \nabla Y_i) + \rho R_i, \tag{2.19}$$

where equation represents the mass fraction of species contained within a particular volume element. The mass flow rate of the species across the volume element's surface, species diffusion, and the production rate of the species. To elaborate, Y_i represents the mass fraction of the i-th species, D_i signifies the binary diffusion coefficient for the i-th species, and R_i denotes the production rate for the i-th species.

2.2.1. Flame Structure

Laminar premixed flames exhibit distinct flame structures, which can be classified based on their temperature and species profiles. The temperature profile of a laminar flame is characterized by a steep temperature gradient across a thin reaction zone where the reactants are converted into products as seen by the profile of T in Figure 2.5. The thickness of the reaction zone and the shape of the temperature and species profiles depend on the properties of the fuel and oxidizer and the flame speed.

In laminar premixed flames, temperature and species concentration vary in the direction of flame propagation. As the fuel and oxidizer mixture ignites and combustion reactions occur, heat is released, and the temperature in the reaction zone increases. There are 2 main regions on the reaction called pre-reaction (unburnt) and post-reaction (burnt). The zone closer to upstream called unburnt region, contains the fuel and oxidizer before the reaction occurs. Therefore, unburnt region is highly concentrated with fuel and oxidizer, as a contrast, the reactants are depleted in the reaction zone. Afterwards, creating a region with low concentrations of both fuel and oxidizer. This low fuel and oxidizer concentration for region is called the burnt gas region or post-flame region. The thickness of the reaction zone demonstrated in Figure 2.5 including temperature and species concentration profiles in the unburnt and burnt regions. These regions are mainly influenced by several factors, including the fuel composition, fuel type, flow velocity of the mixture and the temperature and pressure of the system.

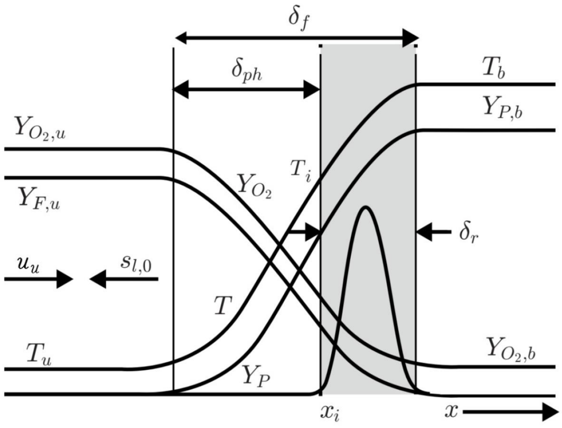

Figure 2.5: Schematic of Species and Temperature Variation of Laminar Premixed Flames

The flame front thickness in laminar premixed flames characterizes the spatial extent over which the combustion reactions take place. A common way to define the flame thickness, denoted as δ_F, is the distance between the points where the temperature rises from the unburned mixture temperature to the adiabatic flame temperature. To quantify the flame thickness, it is essential to examine the temperature and species concentration profiles along the flame front. A fundamental relation for the laminar flame thickness can be derived from the thermal-diffusive balance in the flame zone [58], which approximated by the following equation :

$$\delta_F = \frac{\lambda_u}{\rho c_p} \frac{1}{S_L}, \tag{2.20}$$

where λ_u represents the thermal conductivity, c_p denotes the specific heat at constant pressure of the unburnt mixture and S_L represents the laminar flame speed.

2.2.2. Laminar Flame Speed

The laminar flame speed is a characteristic parameter when investigating flame stability, which refers to a flame's capacity to sustain its form and intensity under varying flow conditions [63]. In order to quantify laminar flame speed , [6] purposed that S_L can be determined both experimentally and numerically under the same conditions. For experimental investigations, Bunsen burner method was specifically designed for S_L determination for free-stream jet flames [29]. Similarly, the "burner stabilized flame" method was employed to measure the flame propagation speed in a laminar burn [22]. This technique involves the flame advancing towards the unburned mixture at a particular cone angle, denoted as α in Figure 2.6. Essentially, calculation of laminar flame speed (S_L) comes based on the unburned mixture's velocity, which is perpendicular to the flame front as seen as Figure 2.6. This is because the unburned mixture's velocity ($v_{n,u}$) in this direction is equal to the laminar flame speed when the flame is operating under laminar conditions also means reaction zone of the flame (oblique flame front) is assumed stationary due to time. The laminar flame speed $S_L = S_{L,u}$ demonstrated in Figure 2.6 balance with mixture velocity (v_u) is conducted as follows [9];

$$S_{L,u} = v_u sin(\alpha) = v_{n,u} \tag{2.21}$$

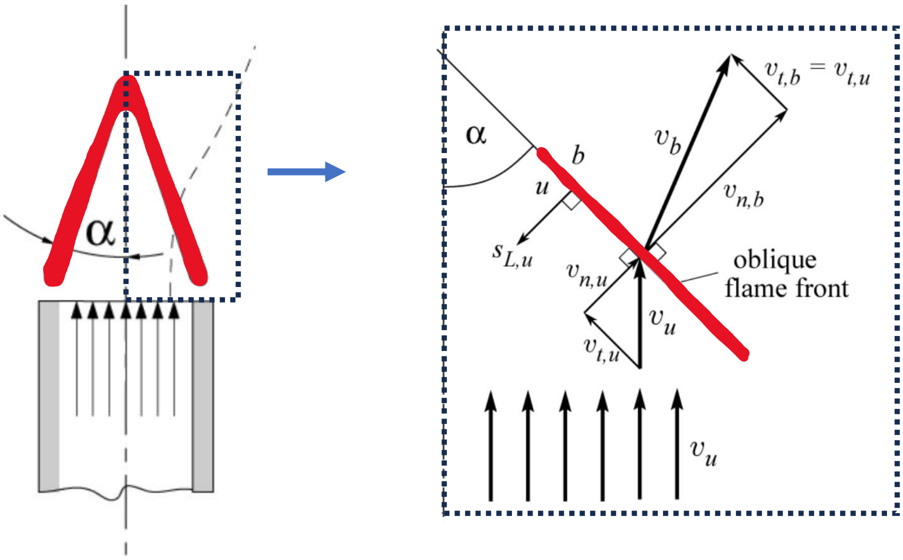

Figure 2.6: Schematic of Laminar Premixed Flame Speed

The laminar flame speed (S_L) is a metric in premixed combustion, representing the propagation velocity of an unstrained flame front in stable condition. Flame speed depends on several thermo-physical parameters: the type of fuel being combusted, the composition of the mixture (particularly in terms of the equivalence ratio), the initial temperature of the reactants, and the prevailing pressure conditions. As depicted in Figure 2.7, the interplay between these factors can lead to nuanced variations in S_L across different fuel's combustion scenarios. In the presented figures, the laminar flame speed for both methane-air and hydrogen-air mixtures are depicted across various equivalence ratios and under different pressures. In both graphs, a distinct peak in the laminar flame speed. This occurs near stoichiometric conditions, where the fuel and air are in optimal balance for combustion [17]. For the methane-air mixture, the peak flame speed is observed at an equivalence ratio slightly richer than stoichiometric. On the other hand, the hydrogen-air mixture exhibits a higher peak in flame speed at an equivalence ratio is higher than stoichiometric. Hydrogen, with its low ignition energy and wide flammability range, displays higher flame speeds under richer conditions as depicted in Figure 2.7 [35].

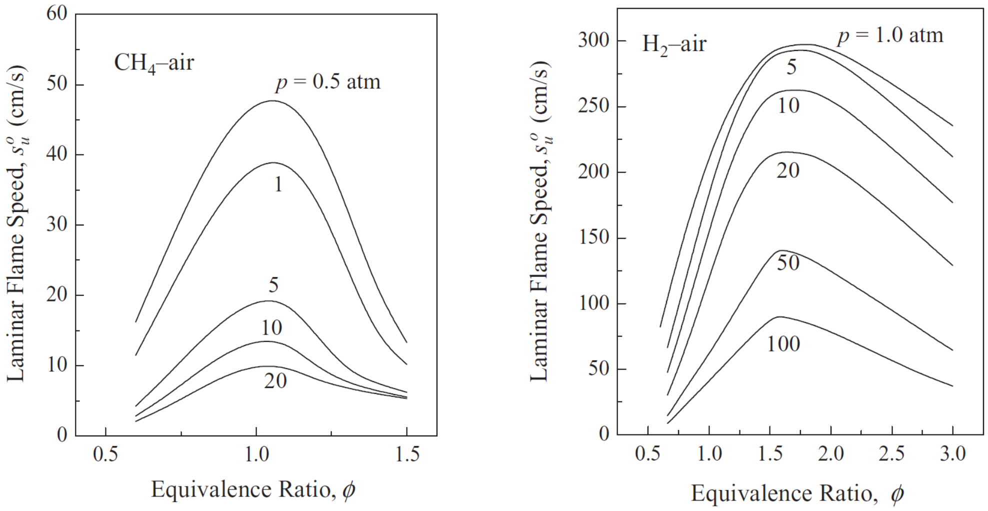

a) b)

Figure 2.7: Schematic of Laminar Premixed Flame Speed variation with equivalence ratio, a) CH4-air b) H2-air, adopted from [35]

2.3. Flame Stretch

Flame stretch is an aspect of flame dynamics, especially gives an indication of how flame surface area has been changed or deformed. Flame stretch is influenced by the flame's interaction with the surrounding flow field and can be observed under positive and negative curvatures represented by Figure 2.8.

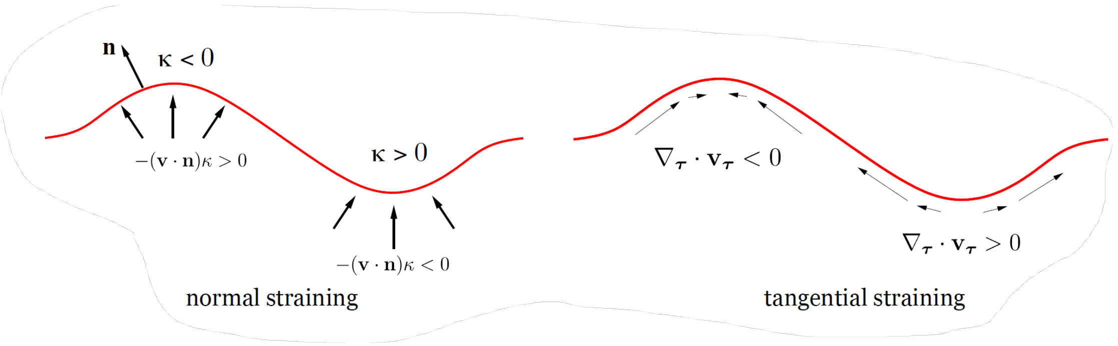

Figure 2.8: Demonstration of Normal and Tangential Stretch Effects

Figure a represents the normal stretch, which is the rate at which the flame front area changes due to the local curvature (κ). Under positive curvature, the flame front exhibits a concave shape, causing the flame to propagate into the unburned mixture. In this case, the normal stretch can enhance flame propagation, leading to an increase in the local flame speed. Conversely, under negative curvature, the flame front adopts a convex shape, which can cause the flame to propagate away from the unburned mixture yields positive stretch in normal direction of flame front. Figure b illustrates the tangential stretch, which refers to the rate at which the flame front deforms along its tangential direction due to the divergence of the flow field. In flame dynamics, it is possible to track the dynamic evaluation of a flame surface element in Lagrangian frame [11],

$$K = \frac{1}{A}\frac{\partial A}{\partial t}, \tag{2.22}$$

This equation defines the flame stretch rate, denoted as K, in terms of the change in flame surface area, A, over time, t, while emphasizing the effect of the local flow field and inherent flame properties. The evaluation of the flame surface area can also be expressed as the divergence of the local velocity on the finite surface,

$$K = \nabla_t \cdot \vec{V}, \tag{2.23}$$

where equation represents another definition of total stretch, while using divergence operator combined with a global velocity component. Furthermore, equation can be decomposed into two main components in terms of local velocity which are velocity in normal and tangential direction;

$$K = K_{n+t} = \nabla_t \cdot \vec{V_t} + \nabla_t \cdot \vec{V_n}, \tag{2.24}$$

where $K = K_{n+t}$ represents cumulative stretch on flame front surface element, $\nabla_t \cdot \vec{V_t}$ denotes stretch or aerodynamic strain rate as seen in [72] in tangential direction of flame surface due to non-uniformities in tangential velocities, $\nabla_t \cdot \vec{V_n}$ represents normal stretch experienced by non-stationary curved flame. Essentially, $\vec{V_n}$ is the local relative velocity contributions on the flame surface normal, which can be also expressed by the local dynamic nature of the flame. As seen, flame movement in the normal direction will further contribute to local curvature κ, ultimately expressing the stretch due to curvature based on flame normal propagation.

$$K_{n+t} = \underbrace{\nabla_t \cdot \vec{V_t}}_{\text{tangential stretch}} + \underbrace{(\vec{u}\cdot\vec{n} + S_f)\kappa}_{\text{normal stretch due to curvature}} \tag{2.25}$$

The interaction between flame dynamics and stretch effects can be represented using non-dimensional parameters. A non-dimensional parameter in this context is the Markstein number, Ma. Markstein number as a non-dimensional parameter characterizes the sensitivity of the flame speed to flame stretch [19], [24], [47] and is given by:

$$Ma = \frac{L_M}{\delta}, \tag{2.26}$$

where L_M is the Markstein length and δ is the laminar flame thickness. The implications are; a positive Ma signifies a decrease in flame speed with increasing stretch and a negative Ma indicates the opposite. Connecting flame speed, S_L, to stretch, the relation becomes:

$$S_L = S_{L0} - LK, \tag{2.27}$$

Incorporating Ma:

$$\frac{S_L}{S_{L0}} = 1 - Ma \cdot \frac{\mathbb{K}\delta}{S_{L0}} = 1 - Ma \cdot Ka, \tag{2.28}$$

Another non-dimensional parameter that intersects with stretch effects is the Lewis number, denoted as Le. The Lewis number indicates the ratio of thermal diffusivity to mass diffusivity. It's important to note that the Lewis number changes based on local burning speeds and the way the mixture stretches, meaning directly related to the mixture. As the flame interacts with the flow field, the flame's local flame speed is affected by the normal and tangential stretch [41].

$$Le = \frac{\alpha}{D} = \frac{\alpha}{\rho c_p D}, \tag{2.29}$$

where D is the mass diffusivity, which has units of m^2/s. On the other hand; where α is the thermal diffusivity. Lewis number greater than one (Le>1) indicates that thermal diffusion is dominant over mass diffusion, resulting in a steeper temperature profile and thinner flame front. Conversely, a low Lewis number (Le<1) means that reactants are transported to the flame front more quickly than heat is conducted away from the flame front, resulting in a thicker reaction zone [35]. Furthermore, the relationship between the local stretch/strain rate of the reaction zone and the local Lewis number is closely related. Flames characterized by Le>1 tend to be more resilient against extinction due to stretch compared to those where Le<1. This resilience holds because of the fact that dominance of thermal diffusion in flames where the Lewis number is greater than one. The rapid diffusion of heat relative to species maintains the flame's thermal stability, making it less susceptible to the effects of stretch. Local stretch/strain and the effect of Lewis number can also be characterized by local flame speed [72]. Under high stretch conditions, the local flame speed can increase, which may cause the mass diffusivity to increase more rapidly than the thermal diffusivity [69]. Consequently, this connects with decrease in the Lewis number of the mixture. Conversely, under low stretch conditions, the local flame speed may decrease, causing the mass diffusivity to decrease more slowly than the thermal diffusivity, leading to an increase in the mixture Lewis number .

2.4. Turbulent Premixed Flames

Turbulent premixed flames are characterized by complex interactions between turbulence and combustion processes, leading to enhanced mixing and more efficient energy conversion. In turbulence, eddies of different sizes are created due to the instability and chaotic nature of the flow as illustrated Figure 2.9 mostly characterizing by turbulence-flame interactions on the complex reaction zone (represented by red) in between burnt and unburnt (fresh gases) region. Therefore, the fact that red zone is evaluating by time, simplicity analysis can be imposed. For averaged flame speed on averaged flame surface area represented by gray color will be further examined in section 2.5, under turbulent flame speed.

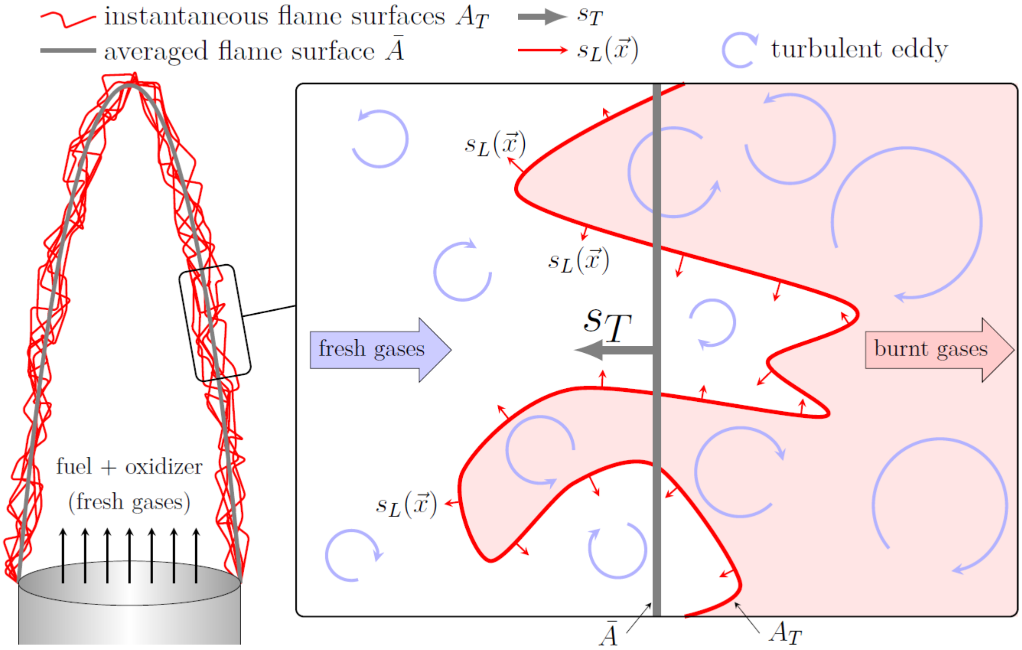

Figure 2.9: Turbulent Premixed Flame-Flow Interaction, adopted by [72]

Represented eddies in Figure 2.9 (purple colored) can significantly distort the flame front and enhance the overall combustion by increasing the surface area over which the reaction can occur. The local flame speed, denoted as $S_L(x)$ will vary along the front due to the turbulent nature of the flow.

In the study of turbulent premixed flames, the Karlovitz number (Ka) and Damköhler number (Da) are essential dimensionless parameters that describe the flame behavior. The Karlovitz number quantifies the impact of turbulence on the flame structure by comparing the characteristic time scales of flame chemistry and turbulence-induced strain. This parameter compares the characteristic chemical reaction time to the flow's characteristic Kolmogorov time scale in turbulent flows [35]. It is defined as:

$$Ka = \frac{t_{chem}}{t_K} = \left(\frac{\eta}{\delta_f}\right)^2, \tag{2.30}$$

where t_K is the Kolmogorov time scale. A high Karlovitz number signifies that the smallest eddies interfere with flame front, resulting intense mixing. Furthermore, alongside the traditional Karlovitz number, the Borghi diagram introduces the thickness-based Karlovitz number, denoted as Ka_δ. This parameter characterizes the effects of turbulence on the flame's thermal thickness. Specifically, Ka_δ contrasts the flame's thermal thickness time scale with the Kolmogorov time scale:

$$Ka_\delta = \frac{t_\delta}{t_K}, \tag{2.31}$$

Where t_δ represents the time scale associated with the flame's thermal thickness. A high Ka_δ indicates that the turbulent eddies are small compared to the flame thickness, leading to a strong interaction between turbulence and the flame structure. On the other hand, the Damköhler number relates the characteristic chemical time scale to the turbulent flow time scale, providing insights into the balance between chemical reaction rates and turbulent mixing. Damköhler number is defined as:

$$Da = \frac{t_K}{t_{chem}}, \tag{2.32}$$

A high Damköhler number implies that the chemical reactions are much faster than the fluid flow, leading to a thin flame front and faster flame propagation. The Borghi diagram effectively maps these parameters, distinguishing between combustion regimes from wrinkled flamelets to distributed reactions [49]. The diagram shown by Figure 2.10 is a valuable tool for classifying flame regimes can also determined by non-dimensional numbers. It comprises five distinct regions:

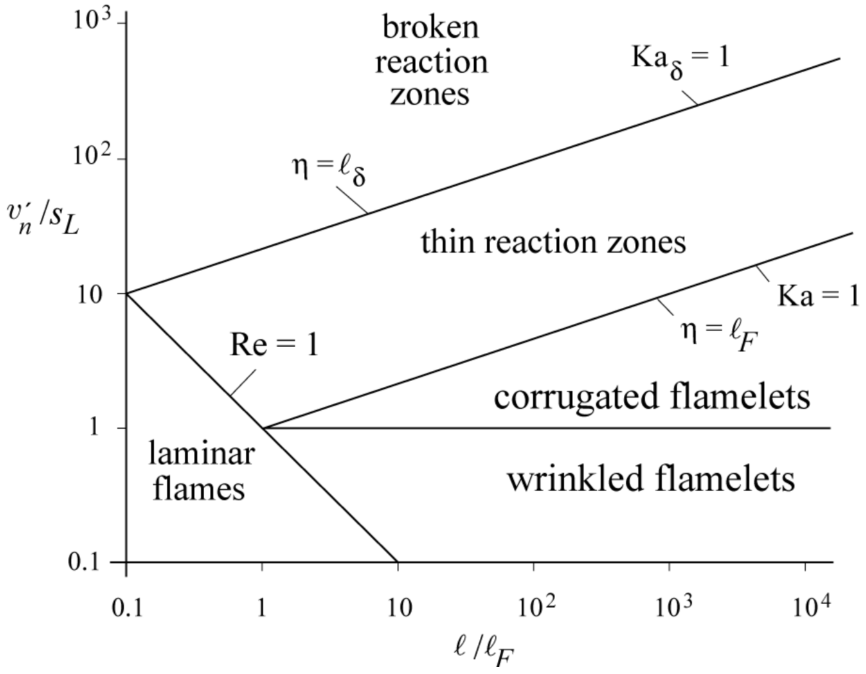

Figure 2.10: Borghi Peters Diagram

- **Weakly-turbulent premixed flames (Re<1):** These flames are characterized by low turbulence levels, resulting in limited flame wrinkling and distortion also called laminar flames.
- **Wrinkled flamelets (Re>1, Ka <1, u' < S_L):** In this regime, the Karlovitz number (Ka) is less than 1 (fast chemistry), indicating that the flame becomes wrinkled with increasing surface area.
- **Corrugated flamelets (Re>1, Ka <1, u' > S_L) :** Although the Karlovitz number remains less than 1 in this regime, the turbulence intensity exceeds the laminar flame speed. As a result, the interaction between the flame and turbulent eddies causes considerable flame wrinkling and potential island formations of unburnt and burnt mixtures.
- **Thin reaction zone (Re>1, Ka <1, Ka_δ < 1):** In this regime, the smallest turbulent eddies are about the same size or smaller than the laminar flame thickness, but notably larger than the reaction zone. Eddies can penetrate the preheat zone, increasing the rates of mass and heat transfer.

- **Broken reaction zone(Re>1, Ka_δ> 1):**In this extreme regime, turbulent eddies infiltrate the reaction zone, enhancing heat transfer into the preheat zone. This intrusion leads to a rapid decrease in flame temperature, potentially leading to flame extinction.

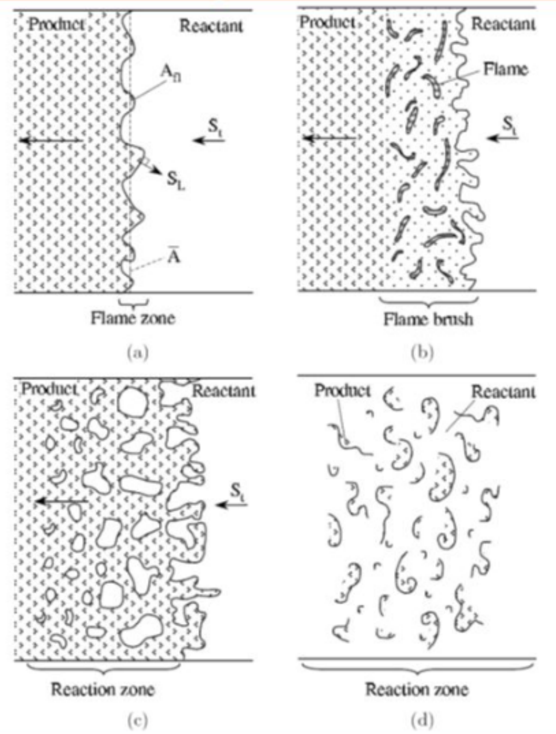

Figure 2.11: Premixed turbulent flame regimes; a) Wrinkled flamelet, b) Thin reaction zone, c) Corrugated flamelet, d) Broken reaction zone., [2]

.

Figure 2.11 illustrates 4 different zones or typical turbulent premixed flames. Upon examining the Borghi diagram, we can first observe that when Re < 1, the turbulent intensity is weak, and the scales are small. As the flow transitions to laminar, the contribution to flame wrinkling diminishes. Second, for Re > 1, Ka < 1, and $\frac{u'}{S_L}$ < 1, we enter the wrinkled flame regime, which signifies that the flame front is retained, but the flame surface becomes increasingly wrinkled. For example, hydrogen flames exhibit lower heat diffusivity, resulting in a lower Ka number. Consequently, due to the low Ka number, we expect to observe a higher occurrence of flame cusps in pure hydrogen flames, as corroborated by [18].

2.5. Turbulent Flame Speed

Turbulent flame speed denotes the rate at which a flame propagates through a fuel-air mixture under turbulent flow conditions. This speed directly affects the flame front's advancement through the mixture, which accounts for flames in turbulent settings with an increase of flame surface area. That emphasizes turbulent flow is characterized by highly chaotic and disordered fluid motion, with eddies and vortices continuously interacting with the reaction zone. The turbulent flame speed S_T is typically computed by taking into account of average flow velocity over the flame front. This gives an overall measure of how fast the flame is propagating on average. In the study of turbulent premixed flames, it is essential to consider the conservation of mass flow rate, assuming no additional intake or exit of fluid in the flow.

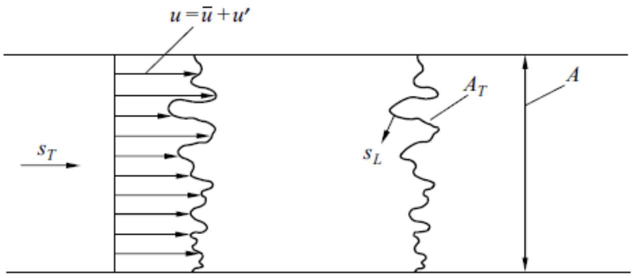

Figure 2.12: Turbulent burning velocity definition for wrinkled/turbulent flame fronts

Here, Figure 2.12 shows a wrinkled flame front due to turbulence. Due to the flame turbulence interaction, flame area demonstrated by A_T becomes higher than tube cross section, A. Nevertheless, the mass flow rate remains constant throughout the tube due to continuity law. The equation to determine the relationship between the flame surface area and the tube cross-sectional area for premixed flames is as follows:

$$\dot{m} = \rho_u S_L A_t = \rho_u S_T A \tag{2.33}$$

Here, ρ_u denotes the unburned region's density, while S_L and S_T represent laminar and turbulent flame speeds, respectively. A_T corresponds to the flame surface area, and A is the normalized channel area obtained by averaging A_T, which contributes to the turbulent flame speed. Assuming ρ_u is constant due to conservation laws:

$$\frac{S_T}{S_L} = \frac{A_T}{A} \tag{2.34}$$

Using a common burner type, such as the Bunsen Burner, we employ a geometrical analogy to determine the scaling of turbulent intensity and turbulent flame speed:

$$\frac{A_T}{A} = \frac{u'}{S_L}, S_T \propto u' \tag{2.35}$$

This expression represents the kinematic scaling, given by $(\frac{u'}{S_L})$. For small-scale turbulence, it is necessary to identify thin reaction zones to understand the behavior of turbulence-flame interactions, as small-scale turbulence alters the transport between the reaction zone and unburnt gas [35].

2.6. Flame Flashback

Flame flashback is a critical safety issue in combustion processes, defined as the undesirable upstream propagation of the flame into the burner. In other words, instead of the flame staying stably at the intended location, it 'flashes back' into the incoming fuel-air mixture, resulting in potential damage to the combustion equipment. The flashback phenomenon can occur due to a number of reasons, such as turbulence, flame holder geometry, flow velocity, fuel type, equivalence ratio, burner material, and burner tip temperature [20]. Flame flashback can be broken down into four distinct types, based on where the flashback occurs and the parameters influencing these regions.

- Core Flow Flashback: This type of flashback happens when the turbulent flame speed surpasses the local flow velocity. A decrease in air or mixture mass flow can significantly impact the flame propagation in the core flow.
- Combustion Instability-Induced Flashback: This type of flashback is a result of significant pressure fluctuations within the combustor. The instability linked to pressure and velocity can drive flame movement, and the generation of large vortices could result in the backward propagation of the turbulent flame front [33].
- Combustion-Induced Vortex Breakdown: This form of flashback is especially relevant for swirl-stabilized burners. The vortex breakdown structure refers to the stagnant axis of the vortex moving in the opposite direction of the axial flow line. This structure moves from the burner exit region deep into the burner [37].
- Boundary Layer Flashback: A low velocity gradient close to the wall leads to decreased local flow velocity due to the no-slip condition. Hence, flame speed exceeds the local flow velocity and further increases the flashback propensity.

2.6.1. Boundary Layer Flashback

Boundary layer flashback usually occurs in the laminar and turbulent boundary layer near the wall of a duct or a burner. The boundary layer, formed due to the no-slip velocity condition at the wall boundary where viscous effects are significant. Indeed, high viscous effects results a decrement in flow velocity as it approaches the wall. Ultimately, local flame speed exceeds the flow near the wall which initiates flame detach from its intended position and propagate upstream.

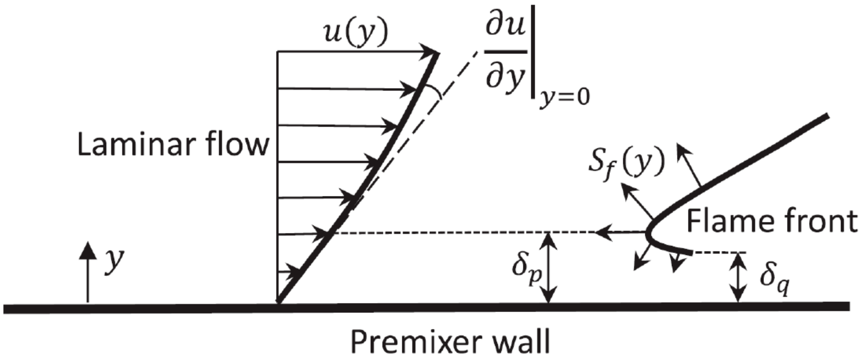

Figure 2.13: Illustration of Boundary Layer Flashback
[31]

Figure 2.13 shows a visual depiction of boundary layer flashback. Here, a flow with a velocity profile $u(y)$ is shown propagating to the right with no-slip velocity at premixed wall. The local flame speed denoted by $S_f(y)$ and the interaction between the flow and the flame front creates a specific region, marked as δq, known as the quenching distance. This distance represents the closest point the flame can approach the wall before it is extinguished due to heat loss to the wall. Various factors come into play that can influence the occurrence and characteristics of boundary layer flashback. Some of the key factors include:

- Quenching Distance: This is the minimum thickness of the flame at which combustion can occur. If the boundary layer thickness becomes smaller than the quenching distance, flashback can be triggered.
- Critical Velocity Gradient: Corresponds to the bulk velocity at the condition of flashback which is also an indication of flame's flashback propensity [31].
- Fuel-Oxidizer Composition: The fuel and oxidizer's relative proportions affect the flame speed and stability, influencing the likelihood of flashback.
- Burner Material and Geometrical Configuration: The material of the burner and its shape can influence the thermal properties of the burner and the flow characteristics, respectively, both of which can affect flashback.
- Preheat Temperature: An increase in preheat temperatures can lead to faster flame speeds, thus heightening the probability of a flashback occurrence.
- Operating Pressure: Generally, when operating pressures are increased, the flame speed also tends to decrease, which, in turn affects the likelihood of flashback.

The genesis of systematic experimental investigations into boundary layer flashback was marked by studies examining the propensity of flashback in premixed natural gas-air flames within tube burners of varying diameters [39]. This led to the formulation of the widely accepted critical velocity gradient model, a straightforward model that utilizes the wall's velocity gradient to forecast boundary layer flashback. As depicted in Figure 2.13, a flame can stabilize near the wall. However, due to heat loss, the flame speed decreases as it approaches the wall and eventually gets quenched at a specific quenching distance, denoted as δ_q. The velocity gradient at the wall serves as an indicator of potential flashback. The model suggests that the flame will advance upstream when the local flame speed surpasses the local flow velocity near the wall. The distance δ_p represents the point at which the flame speed matches the flow velocity. Consequently, the critical velocity gradient, symbolized as g_c, is formulated as:

$$g_c = \frac{u(|y = \delta_p)}{\delta_p} = \frac{S_L}{\delta_p} \tag{2.36}$$

2.6.2. Flashback Maps

Flashback maps are providing a quantitative interpretation of the conditions leading to flashback. These maps are created by flames when flashback happens. They highlight the relationships among flame speed, Reynolds Number, bulk velocity, and equivalence ratio, all of which cause flame flashback. These parameters significantly influence flame dynamics, often having an indirect yet profound impact on flame speed.

In experimental lab settings, the procedure for creating these flashback maps are followed; Initially, flames are operated with a Reynolds number (Re) just marginally above the anticipated flashback points, while maintaining consistent flame properties such as fuel composition and type. As the experiment progresses, the Reynolds number is gradually decreased up to when the flashback eventually takes place. The corresponding conditions, particularly the Reynolds number at which the flashback occurred, are simultaneously recorded. This process helps in accurately plotting the flashback points on the map [20][68].

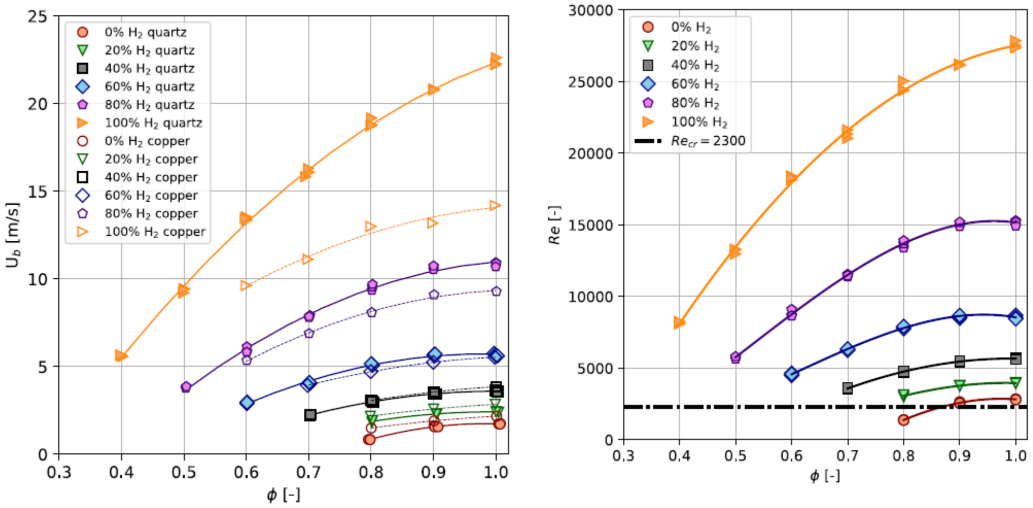

Figure 2.14: (a) The bulk velocity flames flashback points are plotted against the equivalence ratio for six distinct fuel mixtures and different burner material. (b) Reynolds numbers of flames flashback points charted against the equivalence ratio for six varied fuel mixtures.[20]

As shown in Figure 2.14, flame's flasback points have been marked. For Figure 2.14 a) consist of 6 different mixtures with gradually increasing hydrogen content into fuel mixture has also been investigated for different burner materials which are copper and quartz tube captured by [20]. Figure 2.14 b) provides flame's Reynolds numbers during flashback transition. Additionally, dashed line corresponds to the flame where exists in laminar conditions as referred as $Re_{cr} = 2300$. It is obvious that increasing hydrogen content into the mixture also necessitates as increment of system's Reynolds number because of hydrogen's higher propensity of flashback. Moreover, increasing equivalence ratio up to stoichiometric conditions adds more fuel into the mixture as discussed earlier. This suggests that the system must function at a higher Reynolds number, resulting in greater contributions from bulk velocity, while also elevating the equivalence ratio of the identical fuel mixture.

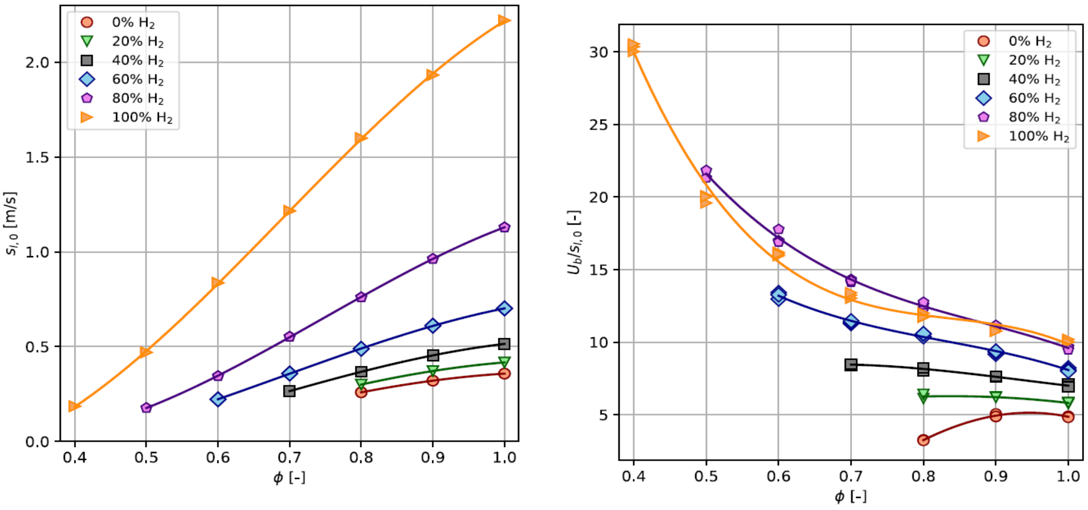

a)

b)

Figure 2.15: (a) The laminar flame speed is plotted against the equivalence ratio for six distinct fuel mixtures. *Cantera*, employing the GRI 3.0 model, is used to compute this laminar speed for fuel compositions containing up to 80% H2. For 100% hydrogen, the Ó Conaire reaction method [46] was utilized [68]. (b) Flashback bulk velocity, normalized using the unstretched laminar flame speed is charted against the equivalence ratio for six varied fuel mixtures.[20] [34]

Figure 2.15, a) showcase the unstretched laminar flame speed as a function of the equivalence ratio, where corresponding detected points are the indications of flame‘s flashback conditions. These results were obtained from 1-D simulations using *Cantera*. Figure 2.15, b) depict the bulk velocity, which has been normalized with the unstretched laminar flame speed, plotted against the equivalence ratio. This provides insights into the behavior of the flame as the mixture becomes richer or leaner. An illustrative example of this can be observed when examining the DNG flame at an equivalence ratio of 1 and operating at both $Re = 3000$ (close to flashback) and $Re = 4000$ (stable). Specifically, H2 flames at an equivalence ratio of 0.49 and operating at $Re = 12000$ (close to flashback) and $Re = 16000$ (stable) mirror consistency on the unstretched laminar flame speed. Importantly, the unstretched laminar flame speed is consistently calculated with Cantera 1-D simulation which results from $0.365 m/s$ across all discussed scenarios.

2.7. Literature Research on Local Flame Displacement Speed

The primary goal of this section is to discuss alternative methods for determining flame displacement speed have been found in literature. After discussing the methods and anticipated outcomes, the current method for displacement speed presented afterwards. The method for calculating flame displacement speed will be explored in more depth in chapter 3.5, titled "Local Velocity Contributions," where we will detail the orientations of the flame front segments.

Other researchers have made significant contributions to examining the local flame displacement speed in the past based on experimental and numerical methods. Poinsot, Echekki, and Mungal [51] based their definition of displacement speed on the asymptotic analysis by Clavin and Joulin [12], formulating the displacement speed as the normal flame front velocity with respect to the unburned gas. Their formulation, which took into account the laminar flame speed, a correction parameter for high stretch values, a characteristic length scale, and fluid velocity, was applied in the numerical simulation of a quasi-one dimensional model of a two-dimensional Bunsen flame tip [51]. Despite the necessity to assume unity Lewis numbers in this early calculation, they concluded that the primary correlation was to stretch, with no report of negative displacement speeds due to the flame's concave nature to the reactants.

Following from the work of Poinsot, Echekki, and Mungal, Najm and Wyckoff [44] in 1997, characterized the displacement speed of an isocontour of methane mass fraction (Y_{CH4}). They used a method for calculating the fluid velocity in normal direction of flame front to approach flame speed and also they determined mass fraction of methane (Y_{CH4} = 0.1) to determine predicted flame front position. Their exploration yields on how changes in displacement speed correlated with shifts in flame thickness, influenced by compressive tangential strain. Clearly, they observed negative displacement speeds when the flame was sharply convex towards reactants.

A particularly similar method was put forth by Gran, Echekki, and Chen [50] in 1998 during a computational study of a premixed, stoichiometric methane-air flame.

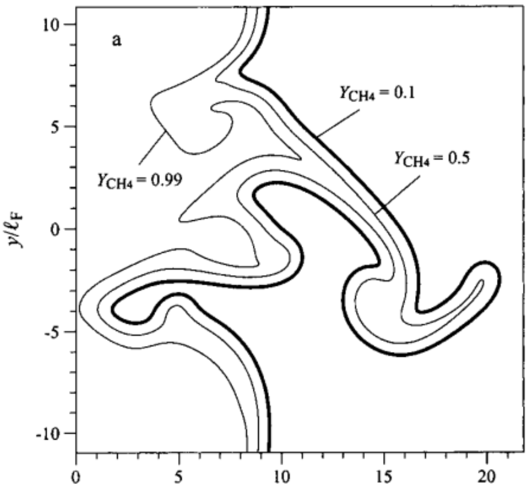

Figure 2.16: Iso-mass fractions of YCH4 represents flame propagation right to left, [50]

As illustrated in Figure 2.16, the unburned gas was preheated to 800 K and the displacement speed was defined considering methane mass fraction (Y_{CH4}). Selecting the isocontour (Y_{CH4} = 0.02) to define the flame surface, Gran and his colleagues discovered a correlation between displacement speed and curvature. Similarly, they noted that the displacement speed, Sd, could become negative in areas of positive curvature where the flame is convex to the reactants. In an attempt to dissect these findings further, Gran et al. splitted up Sd into tangential and normal components on flame surface. Their analysis showed that the negative displacement speed in high positive curvature areas was primarily controlled by the tangential component of unburnt side.

A distinct experimental approach was adopted by Sinibaldi, Mueller, and Driscoll [57] in their study of displacement speed in premixed laminar flames interacting with a toroidal vortex ring.

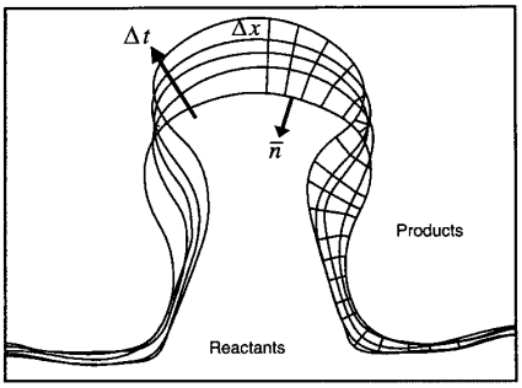

Figure 2.17: Flame interface at five different times at 2.5-ms intervals, flame velocity in laboratory coordinates (v_f). Velocity to normal reactants denoted as (v_r), [14]

Their investigation focused on lean methane and propane flames. They employed Particle Image Velocimetry (PIV) technique to ascertain the quantities needed to define the displacement speed, which they formulated as ;

$$S_d = v_f \cdot n{-}v_r \cdot n. \tag{2.37}$$

In this formula, v_f denotes the local flame speed, and v_r represents the unburned gas velocity ahead of the flame. The unit normal to the flame surface, oriented toward the reactants, is represented by n. Their findings contribute valuable data to the broader understanding of local flame displacement speeds.

Another paper adopts approach to evaluating displacement speed in a premixed methane flame [14]. The authors proposed a method that identifies the Tf = 1200K isotherm as the flame surface represented in Figure 2.18 which represents the location where methane consumption rate. The authors also identified the cold boundary of the thermal zone ahead of the flame surface at the Tc = 350 K isotherm. Using this methodology, they establish a thermal flame thickness, T, of approximately 0.6 mm, measured as the distance between the Tf and Tc isotherms. The displacement speed, Sd, is then determined based on the difference in distances along the integral curves of reaction progress, divided by the time difference between consecutive data snapshots with an interval of Δt = 0.4 ms. The approach ultimaltely follows an equation provides a measure of the local flame displacement speed under time-dependent approaches.

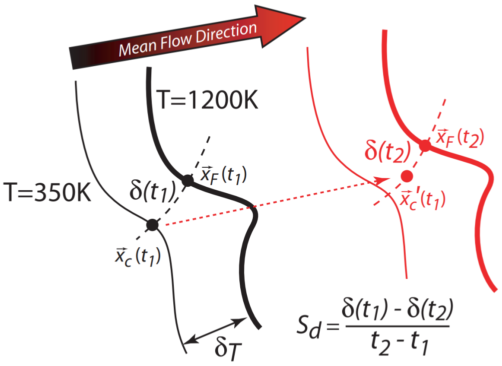

Figure 2.18: Computation of displacement speed based on isotherms using discrete snapshots, [14]

The approach ultimaltely follows an equation provides a measure of the local flame displacement speed under time-dependent approaches and the formulation yields;

$$S_d \approx \frac{\delta(\vec{x}_F(t_1), \vec{x}_c(t_1)) - \delta(\vec{x}_F(t_2), \vec{x}_c'(t_1))}{\Delta t} \tag{2.38}$$

where the positions of the isotherms are demonstrated in Figure 2.18 for initial and subsequent time steps with black and red colors, respectively. Considering the normalized statistics of displacement speed by the flame speed, as illustrated in Figure 2.19, reveal a wide-ranging distribution with significant variations, in line with findings experimental and computational studies. A closer look at the data highlights that extreme values in the distribution have even more pronounced fluctuations, with displacement speeds reaching up to 20 times the laminar flame speed. Notably, a minor portion of the flame displays negative values for S_d.

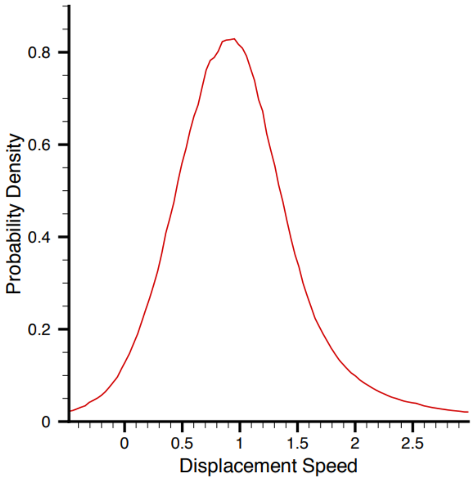

Figure 2.19: PDF distribution of numerical results for turbulent displacement speed (S_d), $[m/s]$ [14]

Another work published by Long et al.,[41] used asynchronous particle image velocimetry (APIV) to understand interaction in between a flame front and a single toroidal vortex for premixed stoichometric methane and air combustion. In the provided Figure 2.20, the relationship between advection and propagation in flame front displacement is visually captured. Initially, we observe flame 'A', which, when solely subjected to the effects of bulk flow, advances to position

’A’ - illustrating the advective behavior of the flame. Concurrently, a separate flame, termed ’B’, emerges. The spatial gap between ’A” and ’B’ encapsulates the flame’s propagation, signifying the movement due to the intrinsic combustion processes. Thus, the figure clearly demarcates the individual contributions of advection and propagation to the overall flame front displacement, offering a lucid comprehension of these intertwined phenomena.

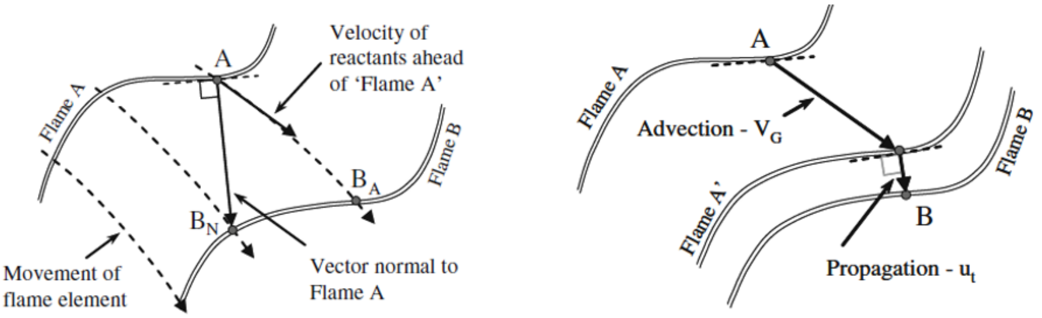

Figure 2.20: Schematic of time sequence of flame front, Flame A at time t, Flame B at time t+dt [41]

After setting up initial conditions of athmospheric pressure and temperature, they continue with following formulation to calculate local burning velocities;

$$u_t = [V_F.n] - [V_G.n] \tag{2.39}$$

Basis of this equation corresponds to, local flow velocity in normal direction (u_t), local flame speed (V_F) on measured flame front in normal direction and flow velocity in the same direction (V_G) shown by Figure 2.20. This approach is based on using data on the speed of particles to predict how the flame will spread over a short period of time. This allows for the creation of a simulated flame front. This virtual flame is then compared with the actual flame translation during this same time interval. The difference between the actual and virtual flame fronts provides the local flame displacement due to propagation, and thus can be used to calculate flame speed.

3

Experimental Methodology and Flame Front Characterization

3.1. Experimental Apparatus

3.1.1. Hardware

The hardware setup for the experiment consists of several components, that are illustrated in Figure 3.1. The first component is the Mass Flow Controller (MFC) (1), which is used to regulate the flow rate of three different gases: air, DNG (Dutch Natural Gas), and hydrogen. The mass flow controllers are manufactured by Bronkhorst and have an uncertainty of 0.1% of the full scale (FS) plus 0.5% of the flow rate reading (RD) [3]. The mass flow controllers measure the flow in normal liters per minute, which has to be converted into liters per minute using the ideal gas law:

$$Q_{\text{actual}} = Q_{\text{read}} \left(\frac{p_n}{p} \right) \left(\frac{T}{T_n} \right), \tag{3.1}$$

where Q_{actual} is the actual flow rate in normal liters per minute and Q_{read} is the reading measured flow rate in normal liters per minute, p is the lab pressure and T is the lab temperature. The subscript n denotes the normal reference values of the pressure and temperature, where $p_n = 101325$ Pa and $T_n = 273.15$ K. The lab conditions were continuously measured by a portable weather station. Air pipeline is connected to the Seeder (2) that introduces seeding particles into the airflow. There are two pipes in the setup, one with length L_h and another one with L_v, which guide the flow of gases in horizontal and vertical directions, respectively. The UV sensor (4) depicted in Figure 3.1 serves as a safety mechanism within the experimental setup. Its primary function is to ensure safe operation by enabling the opening of the main fuel valves only when a flame is detected [68], [20], [34].

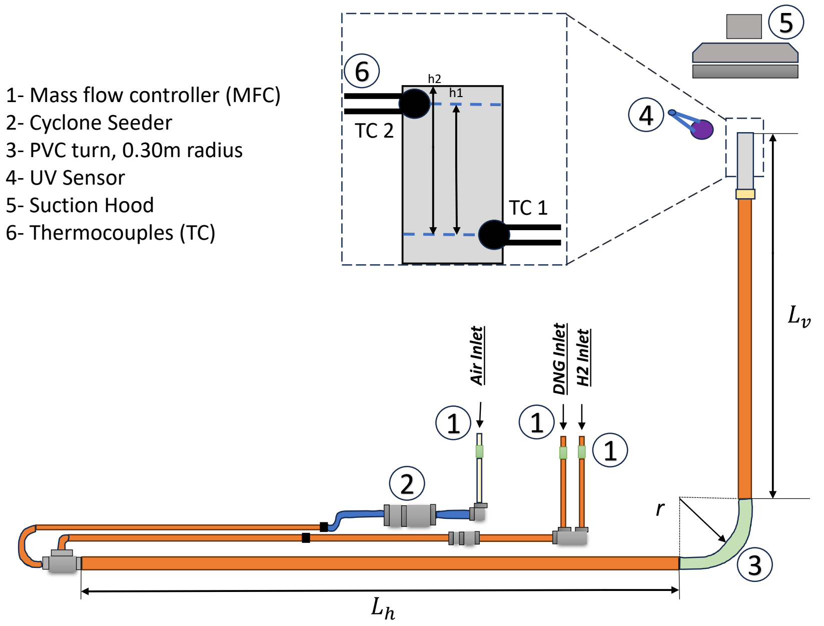

Figure 3.1: Experimental Setup: Bunsen Burner System - A depiction of the overall assembly and components involved in the Bunsen burner setup used for experimentation.

Above the burner, there is a suction hood (5), which captures combustion products and seeding particles. In order to monitor temperature changes accurately, two K-type thermocouples (6) made of self-adhesive polymide material were employed in this study. The thermocouples were strategically placed to investigate temperature convergence, meaning once stable temperature is reached for TC 1 over time, we further proceed with PIV recording. Thermocouple 1 (TC 1) positioned approximately 88 mm (h2) from the burner rim, and Thermocouple 2 (TC 2) placed around 10 mm (h2- h1) from the burner rim. These thermocouples exhibited a fast reaction time of 0.08 s and operated within a temperature range spanning from 40°C to +250°C during the experiments.

Table 3.1: Dimensions and Material of the Experimental Setup Components

Burner	**Horizontal Tube**	**Vertical Tube**	**Turn**	**Final Tube**
Inner diameter d_i [mm]	25.0	25.67	-	25.16
Wall thickness t [mm]	2	1.1	-	1.47
Lenght [mm]	2300	1000	-	219
Length to diameter ratio l/d_i [-]	92	39		8.7
Material	copper	copper	PVC	Quartz

In order to establish a fully developed turbulent flow within the burner tube, it is crucial to determine the appropriate length-to-diameter ratio. This ratio serves as a key parameter in achieving the desired flow characteristics. According to a study conducted by Çobanoğlu et al. in 2020 [13], this ratio can be effectively estimated from;

$$\frac{l}{d_i} = 1.359\, Re^{\frac{1}{4}}, \tag{3.2}$$

where l represents the length of the tube and d_i is the inner diameter of the tube. The Reynolds number is determined from $Re = \frac{u_b d_i}{\nu}$, where u_b is the bulk velocity and kinematic viscosity of the fluid denoted by ν. By incorporating the Reynolds number into the equation, the appropriate length-to-diameter ratio can be calculated for ensuring the establishment of a fully developed turbulent flow within the burner tube.

3.2. Flow Measurement Technique

3.2.1. Particle Image Velocimetry (PIV)

Particle Image Velocimetry (PIV) is non-intrusive, laser-based measurement technique to capture instantaneous velocity fields within a planar cross-section of the flow [4], in this case, the flow of hydrogen-air-dilute natural gas (DNG) jet flames. This technique relies on the imaging of tracer particles seeded within the fluid. These particles, small enough to follow the fluid motion and survive during combustion reaction. The particles are illuminated by a laser light and their scattered light is recorded by a digital high-speed camera [53]. In essence, PIV provides a comprehensive picture of flow patterns, capturing velocity vectors over a large area in a single instant [32].

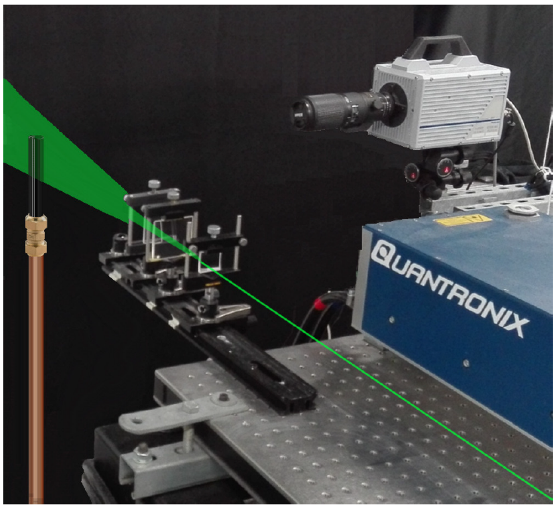

Figure 3.2: Particle Image Velocimetry (PIV) Setup - A demonstration of the PIV system on the Bunsen burner, including a high-speed camera and laser light for capturing particle movement. [68] [20]

In the combustion lab at TU Delft, the PIV apparatus consists of several key components: a laser, optics for creating a light sheet, seeding particles, a high-speed camera, and specialized software named DaVis for equipment management and image-to-velocity field conversion using correlation algorithms. As depicted in Figure 3.2, the laboratory's PIV system uses a high-speed Photron Fastcam SA1.1 camera in tandem with a Quantronix Nd:YLF dual-cavity laser, known as the DarwinDuo Pro 52780M. The laser produces a green light beam with a wavelength of 527 nm. Initially, this beam is broadened into a vertically directed light sheet with the help of a horizontal plano-concave lens. Subsequently, a vertical plano-convex lens is used to narrow down the light sheet to an approximate thickness of 1 mm. This refined light sheet ultimately passes through the quartz tube portion of the burner, concurrently casting light on the air overlying the burner's edge.

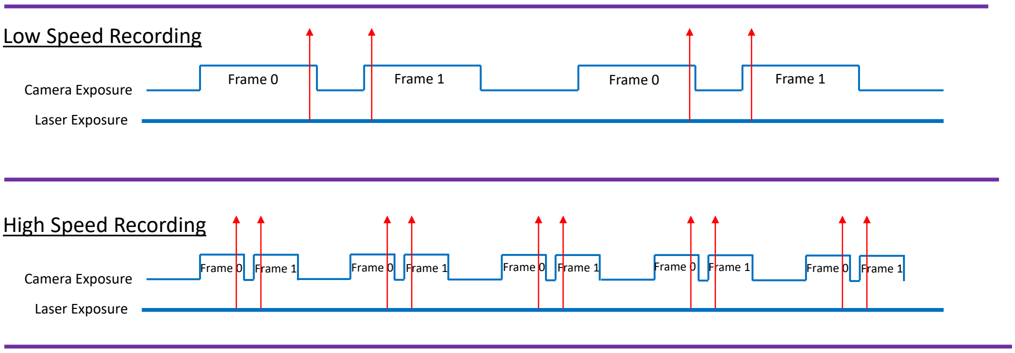

Figure 3.3: Double frame timing configuration for low-speed and high-speed: A diagram detailing the synchronization between the double frame camera exposure (blue colored step function) and laser pulse (red arrow). [28]

Figure 3.3 demonstrates the timing configuration in double frame PIV, indicating the synchronization between pulsed laser emissions and camera exposures. High-speed recordings, with their shorter camera exposure intervals, permit sharp image captures of even rapidly moving particles with effecting the frequency of laser pulse timings. In terms of high-speed recording, the frequency of laser pulses might be higher to illuminate the particles more frequently during the recording period. This synchronization, alongside high-speed recording benefits, allows for an accurate and precise for the particle positions and their subsequent flow fields at specific intervals [66] [36].

In our experiment, the flow is seeded with aluminium oxide (Al_2O_3) particles, that have a diameter of approximately 1 μm by using a cyclone seeder. In techniques such as PIV or Laser Doppler Velocimetry (LDV) [60], micron sized particles are commonly employed to trace fluid motion [4, 59]. These tracer particles, when introduced in an appropriate quantity, are assumed to not alter the flow properties. The concentration of these seeding tracers typically ranges between 10^9 and 10^{12} particles/m^3 [53]. Beyond this upper limit, the tracers may start to influence the flow due to multi-phase flow effects. The governing principle of this process is the mass ratio of fluid to particles, which should not exceed the order of 10^{-3} for micron-sized droplets in airflows [59].

The motion dynamics of tracer particles in a fluid flow can be understood from a force balance perspective. Fundamentally, the balance between the forces acting on the particle ensures that it follows the fluid motion faithfully. These forces include the drag force, gravitational (or buoyancy) force, Basset (history) force, lift force, and pressure gradient force. For PIV applications, especially with small tracer particles, the drag force or Stokes drag, and the gravitational (or buoyancy) force are dominant [59]. The balance between these forces, under Stokes' flow conditions, yields:

$$3\pi d_p \mu (V(t) - U(t)) = (\rho_p - \rho_f) g \frac{4}{3} \pi (\frac{d_p}{2})^3, \tag{3.3}$$

where $V(t)$ and $U(t)$ represents velocity of the particle and fluid, respectively. As given by the equation, μ denotes the dynamic viscosity, d_p tracer particle's diameter , and ρ_p and ρ_f correspond to the densities of the seeding particles and fluid, respectively [4, 53].

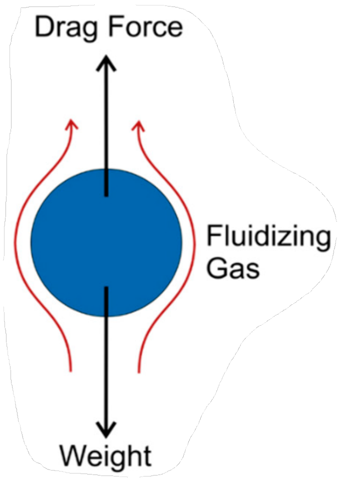

Figure 3.4: Drag and Gravity forces acting on a spherical particle, [56]

In relation to slip or settling velocity (represented as $(V(t) - U(t))$), tracer particles can track fluid flow accurately, provided the condition $(\rho_p >> \rho_f)$ is satisfied. This condition is easily met in liquid flows. However, in gas flows, where the typical density ratio value is $\rho_p/\rho_f = O(10^3)$, smaller diameter particles $(0.5\mu m < d_p < 5\mu m)$ are utilized [59]. The temporal evolution of the particle velocity can be described by the following equation, in which V_∞ is the steady-state velocity and τ_p is the particle response time (to see full derivation, see appendix A.2):

$$V(t) = V_\infty(1 - e^{-t/\tau_p}), \tag{3.4}$$

The response time of the particle τ_p is given by,

$$\tau_p = \frac{\rho_p d_p^2}{18\mu}, \tag{3.5}$$

where the response time is a measure of how quickly a particle can respond to changes in the fluid flow. The particle response time, or the characteristic time scale, specifies the duration needed for a stationary particle to reach approximately 63 percent of the ambient air velocity. For the experiments conducted, aluminium oxide (Al_2O_3) particles were employed as the seeding particles. These particles have a mean diameter of 1 μm and a density of 3200 kg/m^3. Given the dynamic viscosity of air is 18.7×10^{-6} Pa.s at a temperature of 300 K, the particle response time is computed to be 9.5 μs. A useful determinant in assessing whether the particles will act as tracers is the Stokes number (St) which is a valuable measure in determining the efficiency of particles as tracers. It is obtained by comparing the particle response time (τ_p) with the Kolmogorov time scale of the flow (τ_η) [52];

$$St = \tau_p/\tau_\eta \tag{3.6}$$

If St « 1, it suggests that the seeding particles are able to accurately trace the flow, behaving as ideal tracers. Conversely, if St » 1, the particles remain unresponsive to the flow. This indicates that for the smallest scales of the flow, the seeding particles may not perfectly trace the fluid motion. However, on larger flow scales, the employed seeding particles served as excellent tracers [68].

3.3. Flame Front Tracking

3.3.1. Mie-Scattering

Mie scattering refers to the scattering of light by particles that are similar in size, or even larger than the wavelength of the incident light [16]. In the context of combustion diagnostics, Mie scattering is often used to visualize and measure the velocities of small particles (like seeding particles) in a flow, using techniques like Particle Image Velocimetry (PIV) [70], [21], [71]. In this study, PIV will be used to determine veloicty fields [42] in premixed H2-DNG-air flames produced by Bunsen burner. Raw images from Mie scattered light are used to distinguish between burnt and unburnt regions within the premixed flames. In Figure 3.5, the flame is shown as those two distinct sections. The unburnt section appears white in the 3.5a, indicating a high concentration of particles. In contrast, the burnt section has fewer particles and is where gases have expanded following the combustion process [30]. We have proposed the presence of an interface between these two sections, known as the flame front, which we have attempted to capture using image processing techniques. This flame front is illustrated in blue in Figure 3.5b after applying Bilatheral filter on raw images.

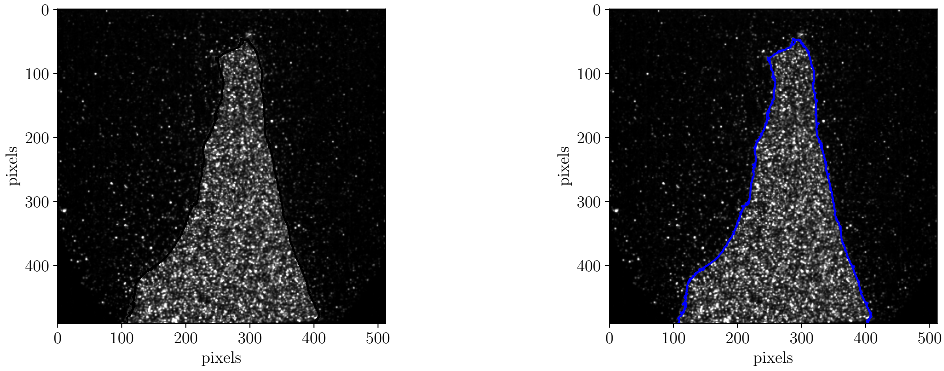

(a) A raw image of the flame under Mie scattering conditions. **(b)** The resultant image after applying bilateral filtering.

Figure 3.5: Flame analysis using Mie scattering and flame front detection

3.3.2. Image Processing

Accurate estimation of the flame front in Mie scattering images necessitates the application of image processing techniques. Due to the complex nature of flame dynamics and the presence of noise and artifacts in the images, direct interpretation of raw data can be challenging. In this study, the bilateral filter was proposed as a key image processing technique for enhancing Mie scattering images. The bilateral filter is a non-linear smoothing filter that takes into account both the spatial and intensity similarities of neighboring pixels. By incorporating spatial and intensity information, the bilateral filter can effectively enhance the flame front features in Mie scattering images, allowing for more accurate estimation and analysis. Essentially, the bilateral filter is a non-linear edge-preserving smoothing filter that removes noise and preserves edge information in the image.

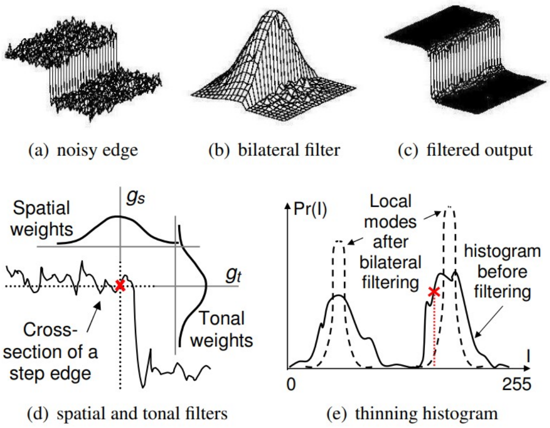

Figure 3.6: Bilateral Filter Illustration - Detailed diagrams explaining the function and effect of the bilateral filter used in the image processing.

To have a look at the steps, Figure 3.6 displays the effectiveness of the bilateral filter in removing noise from an image. Figure 3.6 a) shows a noisy edge, which can obscure important details in the image. The bilateral filter, shown in Figure 3.6 b) will further filters the noisy pattern on Figure 3.6 a) and produce less noisy image as seen in Figure 3.6 c), where Figure 3.6 c) displays the filtered output after applying the bilateral filter. As we can see, the filtered image has much less noise and a smoother appearance, while still retaining the essential edges and details. Figure 3.6 d) and e) show different aspects of the bilateral filter's operation. Figure 3.6 d) represents the bilateral filter's ability to filter both spatial and intensity information in two dimensions. The spatial filtering component accounts for the distance between neighboring pixels, while the tonal component considers the difference in intensity values between pixels. Figure 3.6 e) shows the thinning histogram of the bilateral filtering process, which highlights the local modes present in the filtered image. Local modes represent the peaks in the histogram, indicating the regions where the filter has preserved the most information.

3.4. Flame Front Segmentation

After extracting the flame front using Mie-Scattering and Bilateral Filter techniques, we achieved a high degree of precision in identifying the reaction zone for our flames. Current methodology for flame front segmentation or discretization, primarily leans on the framework proposed by Bribiesca in his work, ”A Geometric Structure for Two-Dimensional Shapes and Three-Dimensional Surfaces” [7] [8]. Bribiesca introduces an innovative geometric structure, the Slope Change Notation (SCN), that presents a novel approach to describing two-dimensional (2D) shapes and three-dimensional (3D) surfaces within a discrete representation based on chain code approach.

In the context of our research, this methodology is visualized by superimposing a series of circles along a curve describing the flame front. The intersection points between the curve and the circles define the discrete shape of the flame front, as illustrated in Figure 3.7. The radius of each circle corresponds to the length of the previously defined segment, offering a quantitative measure for our analysis.

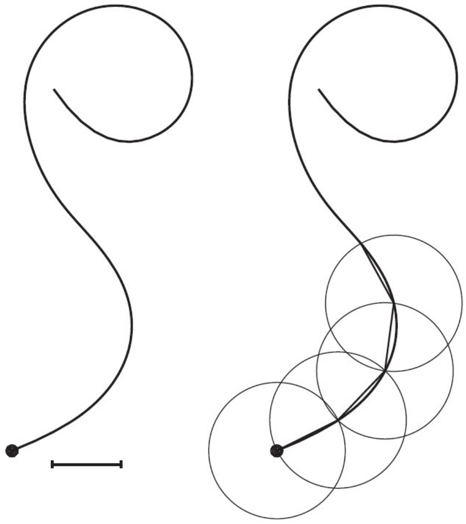

Figure 3.7: Flame Front Segmentation - A display of flame front segmentation implemented on an arbitrary spline, showcasing the segmentation’s effectiveness and precision.

[7]

3.4.1. Slope of line segments

The slope of a line segment represents its steepness or inclination and is defined as the ratio of the vertical change (change in the y-coordinate) to the horizontal change (change in the x-coordinate) between the segment’s endpoints. This concept is useful for determining the rate of change of a curve over a specific interval, enabling the construction of discrete straight-line segments that approximate the smooth, continuous curve. The slope in between consecutive line segments are then calculated and scaled to a continuous range from -1 to 1 which corresponds to -180 and +180 degrees, respectively. After calculating the slope notation in between 2 consecutive segments, we further impose the algorithm to all segments which determine flame front. As demonstrated in Figure 3.8, the slope of the segments determined by using the endpoints, assuming that the segments are represented by the points A, B, C, with B being the intersection of the segments and A and C as the endpoints. Therefore, two segment orientation further results one slope. After construction the numerical identification in between 1 and -1 as seen in Figure 3.9a, we can ultimately determine the slopes of the chain Figure 3.9b.

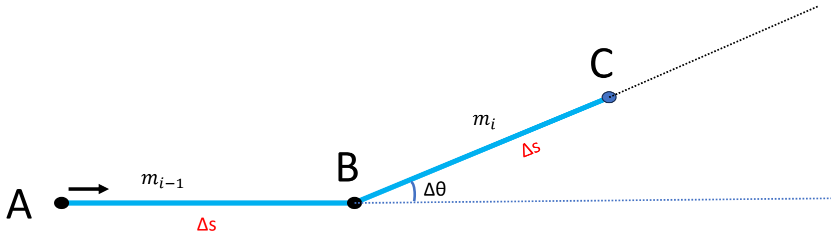

Figure 3.8: Slope representation of 2 consecutive line segments

Mathematically, this can be expressed as;

$$\Delta\theta = arctan(\frac{m_i - m_{i-1}}{1 + m_i m_{i-1}}), \tag{3.7}$$

where $\Delta\theta$ represents the slope difference between two consecutive line segments, while m_i and m_{i-1} denote the slopes of the i-th and $(i-1)$-th segments, respectively. Figure 3.9a illustrates the concept of slope change. The left-hand side arrow indicates the initial slope location, which remains constant regardless of the actual flame front orientation.

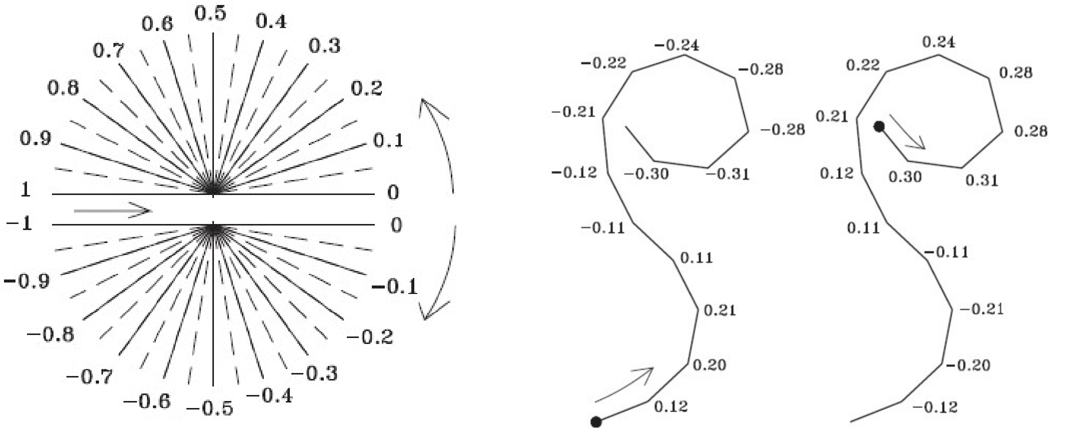

(a) Slope Definition: A graphical definition of the slope concept used in the analysis.

(b) Slope Chains: A depiction of the slope and its chain on an equally discretized curve.

Figure 3.9: Slope analysis of 2 concecutive segments, [7]

3.4.2. Local curvature of flame front

To calculate the curvature of the flame front segments, we consider 3 consecutive segments, meaning 4 different points instead of 3 have been employed. The main reason is most of the flame front segments will be eliminated due to the criterias which will be discussed in following chapters. Therefore, if we assumed that the main segment is represented by m_i in Figure 3.10, we taken into account of one segment above and one segment below and checked the slope change notations. In order to be consistent with the units, we divided slope change into the segment length represented by following:

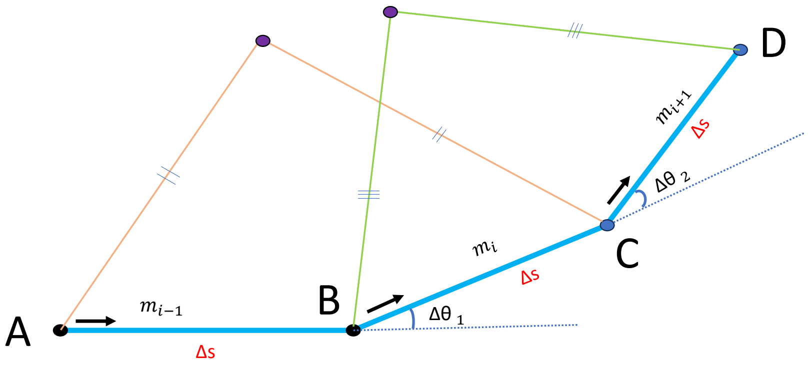

Figure 3.10: Curvature representation of 3 consecutive line segments to calculate curvature of segment m_i

$$\kappa_{m_i} = \frac{\frac{\Delta\theta_1}{\Delta s} + \frac{\Delta\theta_2}{\Delta s}}{2} \tag{3.8}$$

where κ_{m_i} denoted the curvature of the segment (m_i), $\Delta\theta_1$ represents the slope orientation below (in between points A - C) and $\Delta\theta_2$ is the slope orientation of the segment above (in between points B - D) as illustrated in Figure 3.10. In this study, we have assumed that the arc length of each segment is equal to 1 mm, meaning that $\Delta s = 1$ mm.

3.5. Local Velocity Contributions

The Particle Image Velocimetry (PIV) measurements captured in the starting illustrations focus on a DNG (Dutch Natural Gas) jet flame with a Reynolds number $Re = 3000$. This specific setup is of interest as it is proximate to the flashback limit. The PIV methodology employed utilizes an interrogation window size of 16×16 with a 75% overlap, a technique implemented to enhance the predicted accuracy of particle shifts.

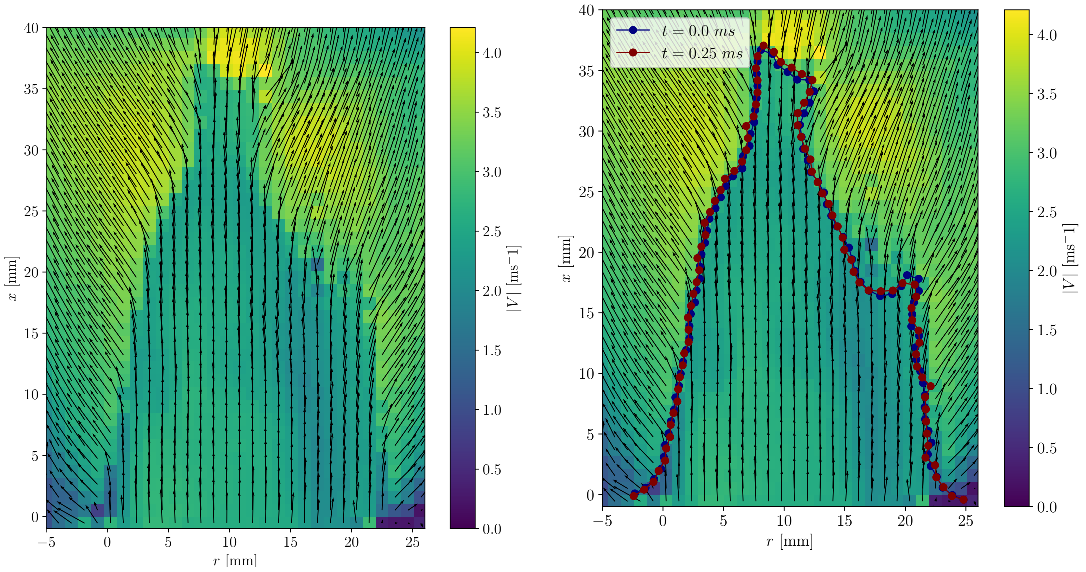

(a) The corresponding contour map showcasing spatial variations in velocity.

(b) Superimposed velocity field and detected flame fronts from Mie scattering.

Figure 3.11: Velocity Vectors and Contour Mapping

Figure Figure 3.11a offers a visual interpretation of the magnitude of these velocity vectors using a color map. Upon examination, it can be observed that the velocity field appears smoother in the unburnt region, exhibiting less complexity and variability. However, upon entering the burnt region, the velocity field exhibits greater complexity. This complexity can be attributed to the velocity jump that occurs as the flow encounters the reaction layer. This velocity jump, caused by the drastic change in properties as the flow transitions from unburnt to burnt regions. Figure 3.11b illustrates the overlay of velocity field data with temporally differentiated flame front locations. Utilizing the same velocity field for reference, flame fronts from two distinct time frames are superimposed, captured via a Bilateral filter applied to Mie-scattered images. In our experimental setup, we employ specific camera exposure timings to facilitate a double-frame mode on the camera. This mode captures two successive Mie-scattered images, referred to as frame 0 and frame 1. These flame fronts are temporally separated by 0.25 ms for DNG flames, offering a visual snapshot of flame front evolution within this brief time interval. The initial flame front is delineated by blue dots whereas the subsequent flame front is highlighted by red dots, capturing its position 0.25 ms later.

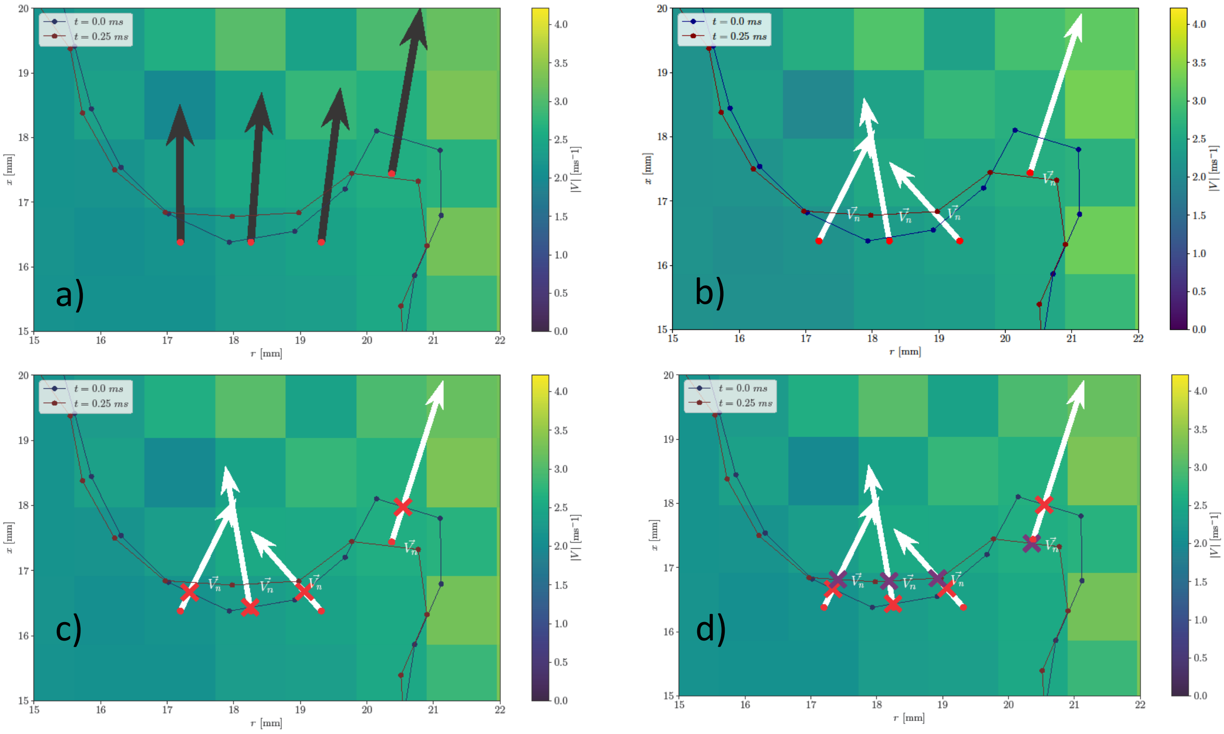

Figure 3.12: a) Velocity vectors crossing Frame 0. b) Decomposed velocities in the normal direction, based on segment orientation, which originally crossed Frame 0. c) Validation of decomposed normal velocities that also cross Frame 0 (t=0 ms). d) Normal velocity vectors that continue to cross Frame 1 (t=0.25 ms) after their initial intersection with Frame 0.

Figure 3.12 a) emphasizing the flow dynamics at $t = 0$ ms (Frame 0), showing velocity vectors that intersect with frame 0. In the subsequent step, based on the orientations of different segments, the velocity vectors from figure a are decomposed into their components in the normal direction on each segments. Figure 3.12 b) displays this decomposition in normal direction with white colored velocity vectors, allowing for a deeper analysis of velocities that align with the propagation direction which assumed normal to the front. Moving forward to Figure 3.12 c), a verification step occurs where the decomposed normal velocities from Figure 3.12 b) are cross-referenced to confirm their intersection with Frame 0 (t= 0 ms). The intersection of these segments with Frame 0 and the corresponding normal velocity is marked with a red cross. This step acts as a validation checkpoint, affirming that the decomposition has been executed accurately and that the pertinent velocities have been pinpointed correctly. Building upon the verified set of normal velocity vectors from Figure 3.12 c), Figure 3.12 d) showcases which among them advance to intersect at $t = 0.25$ ms (Frame 1). The intersection with Frame 1 is highlighted as a purple cross. This progression is instrumental in comprehending the continuity and evolution of flow dynamics across these sequential frames, elucidating how specific velocity vectors transition from their initial interaction with Frame 0 to their subsequent engagement with Frame 1.

3.5.1. Flame Front Propagation

In a premixed combustion environment, the progression of the flame front can either be against the incoming flow (upstream) or with the flow (downstream). In this part of the study, the primary focus is on determining the local displacement speed, S_d, and the consequent direction of movement based on double frames within the corresponding local velocity field calculated on selected segments. S_d is not simply a measure of the flame front's absolute movement speed; rather, it represents how the flame front progresses relative to its environment. This relative speed is computed by measuring the change in flame front position between two successive images and dividing it by the time interval between these images, as demonstrated in the following equation:

$$S_d = \frac{\sqrt{(x_{t1} - x_{t0})^2 + (y_{t1} - y_{t0})^2}}{t_1 - t_0} \tag{3.9}$$

Here, x_{t0}, y_{t0}, x_{t1}, and y_{t1} represent the coordinates of intersection points of consecutive flame front segments and the local flow's normal velocity component, while $t_1 - t_0$ denotes the time interval between the two frames. The essence of S_d lies in its ability to capture the flame front's movement speed relative to the reactant mixture and its position at a previous time point. To determine the direction of the flame front's displacement using these coordinates, the following logic is applied:

- **Positive Downstream Propagation ($S_d > 0$):** If coordinates $|x_{t1}|$ and $|y_{t1}|$ exhibit the flame front at a later point than coordinates $|x_{t0}|$ and $|y_{t0}|$, it indicates downstream propagation following the flow direction (+ displacement).
- **Upstream Propagation ($S_d < 0$):** Conversely, if at t_0 the coordinates of $|x_{t0}|$ and $|y_{t0}|$ is higher than later frame segment (t_1) coordinates ($|x_{t1}|$ and $|y_{t1}|$), suggests the flame is propagating upstream or against the flow (- displacement).

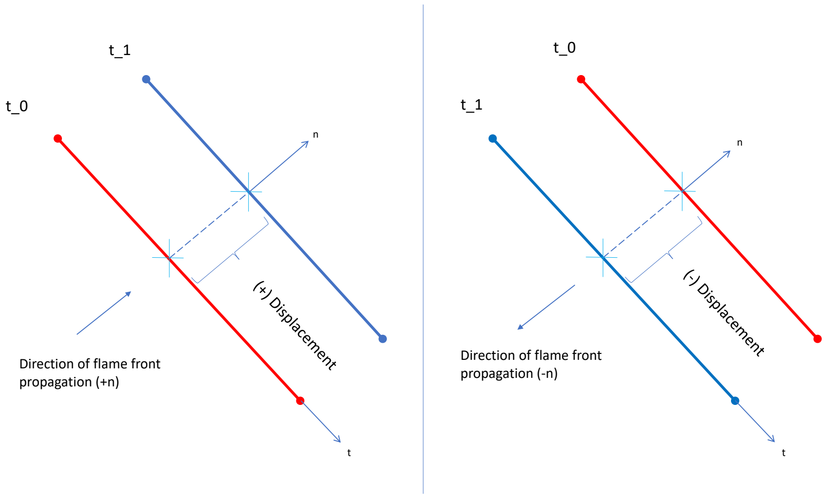

Figure 3.13: Displacement change due to flame front propagation: A graph demonstrating how the flame front's progression affects spatial displacement in the observed field.

As seen in the Figure 3.13, reg segment corresponds to the initial time step of the flame front and blue is the subsequent. Based on the red segment, normal and tangential directions have been drawn. Blue segment does not orient parallel to red segment, therefore, projection of the normal line of the red segment has been taken into account for the relative displacement. This calculation rests upon indeed two primary conditions while considering the flow normal velocity on the segment (V_n) and local flame speed (S_f). In the first scenario, the flame front advances against the flow velocity, yielding an upstream propagation (- displacement) in equation 3.10.

$$S_f = V_n - (-S_d) \tag{3.10}$$

Furthermore, downstream (+ displacement) propagation yields;

$$S_f = V_n - (+S_d) \tag{3.11}$$

It is noteworthy that the tangential component of the velocity vector, which indicates the fluid velocity parallel to the flame front, is not incorporated at this stage of the analysis. While it plays a significant role in characterizing flame deformation and local strain and stretch effects in the tangential direction, its calculation demands a distinct approach. This different approach, towards the analysis of tangential stretch which has been derived from tangential velocities, making it intrinsically a flow behaviour. Details about this approach and its integration into the larger analysis will be addressed in the subsequent chapter. This ensures a more detailed and comprehensive exploration of both normal and tangential influences on flame behavior.

4

Results and Discussion

This chapter presents the results of an experimental investigation into various flow and flame types using different experimental strategies. Sections 4.1 and 4.2 focus on turbulent flow dynamics and turbulent flame characteristics, respectively. Section 4.3 focuses on the developed in-house code results to analyze slope change and local curvature, local velocity contributions, and local flame kinematics of the hydrogen and DNG flame front's.

4.1. Measurement Campaign

The measurement campaign comprises three main parts: Cold Flow, Turbulent Flames with Low Speed Recording, and Turbulent Flames with High Speed Recording. Each section focuses on different aspects of the experimental investigation to gain insights into the characteristics and behavior of the Dutch Natural Gas (DNG) and Hydrogen (H_2) flames under varying conditions. PIV experiments start with calibrating target positioned above burner with an inner diameter of 25.16 mm. The raw PIV images for both cold flow and flame recordings were processed by using 16x16 pixels and an overlap of 75% with enabling multi-pass method.

4.1.1. Cold Flow Measurements

The first part, Cold Flow, serves as a reference point for the subsequent sections in order to validate experimental setup. It involves measurements in the absence of combustion. The results of cold flow measurements will be determined in Section 4.2 including a comparison in between LDA measurement from Tummers et al. [60], was based on a tube with an inner diameter of $d_i = 37$ mm and a Reynolds number of 23000.

Table 4.1: Cold Flow Campaign

$T\ Lab$ ($°C$)	$P\ Lab$ (kPa)	$ImageRate$ (kHz)	Δt (μs)	Re_D -	U_B (m/s)	$Flow$ -
23.8	102.32	0.05	250	4000	2.49	C1
24.1	102.35	0.05	80	12000	8.73	C2
24.0	102.35	0.05	60	16000	12.51	C3
24.2	102.35	0.05	45	23000	14.38	C4

The experiment involved utilizing Particle Image Velocimetry to measure profiles of the mean velocity and turbulence statistics of the cold flow. This study examined four different flow conditions. To verify that the turbulent pipe flow was fully developed, the acquired data will be compared with fully developed flow data available from literature. Table 4.1 lists the characteristics of different cases that have been considered in Cold Flow campaign. Collected data captures laboratory temperature ($T\ Lab$), laboratory pressure ($P\ Lab$), image rate of camera for high and low speed (kHz), time interval of laser pulses (Δt), Reynolds number (Re_D), bulk velocity (U_{Bulk}), and flow name. These cold flow recordings have been completed with adjusting f-stop $(f_{\#})$ equals to 11 and an approximated magnification of $1/3$. Each of the Cold Flow measurements were completed by capturing 2500 images for each Reynolds number.

4.1.2. Low and High Speed Recordings

In this section, we direct our attention towards the measurement of flames from two perspectives: low speed and high speed recordings for flames. Keep in mind that selected fuel compositions were chosen a constant unstretched laminar flame speed as seen in Figure 2.15. These experiments were analyzed based on 5000 images by each fuel each Reynolds number, ensuring a high level of accuracy. These flame recordings have been conducted by adjusting f-stop $(f_{\#})$ equals to 8 and similarly with a magnification of $1/3$. These recordings were used to compute the average flow field of the flames, a topic that will be discussed in greater detail in Section 4.2.

The difference between the low speed and high speed recordings lies in the settings of the camera exposure, which governs the imaging frequency of the particles within the flames. For the level of illumination for low speed recordings was sufficient to capture the average flow field of the flames effectively over the longer recording period.

Table 4.2: Low Speed and High Speed Recordings

$T\ Lab$ ($°C$)	$P\ Lab$ (kPa)	$Image\ Rate$ (kHz)	Δt (μs)	Re_D -	$EqRatio$ (ϕ)	$H2$ (%)	U_B (m/s)	$Fuel$ -
23.1	102.16	0.05	250	3000	1.00	0	1.85	DNG
23.3	102.16	0.05	250	4000	1.00	0	2.49	DNG
23.5	102.19	0.05	80	12000	0.49	100	9.1	H_2
23.8	102.08	0.05	60	16000	0.49	100	11.64	H_2
23.6	102.30	2	250	3000	1.00	0	1.85	DNG
23.3	102.52	2	250	4000	1.00	0	2.49	DNG
23.7	102.76	6.25	80	12000	0.49	100	9.1	H_2
24.1	102.24	6.25	60	16000	0.49	100	11.64	H_2

Table 4.2 provides the settings for low and high speed recordings in terms of (kHz) for DNG and hydrogen flames including equivalence ratio (ϕ), hydrogen concentration and corresponding bulk velocity (U_{Bulk}) of the flames. Low-speed recordings in our experiments are primarily aimed at capturing the averaged flow characteristics of the flames and the results from low speed recordings will be discussed in Section 4.3. This method is effective in determining the overall behavior of turbulent flames. In contrast, high-speed recordings focus on the dynamic aspects of flame behavior while increasing image rate. The primary goal here is to capture rapid, transient formations within the flame. The use of a 6.25 kHz image rate for hydrogen flames in high speed recordings is primarily attributed to their more dynamic nature because of their higher operating Reynolds numbers in these measurements. This higher frequency imaging results in smaller differences between successive images, thus allowing the detection of segment intersections with velocity vectors for double frame mode to more accurately determine local velocity variations

for flame-turbulence interaction.

4.2. Results of Cold Flow Campaign

The settings depicted in Table 4.2, four different cold flow with increasing Reynolds number were captured. These Reynolds numbers cover the spectrum which represent the lower and higher levels of turbulence. By analyzing fully developed flow conditions, the study aimed to gain insights into the normalized velocity and Reynolds stress profiles of turbulent flow dynamics, providing valuable information for validation of the experiments.

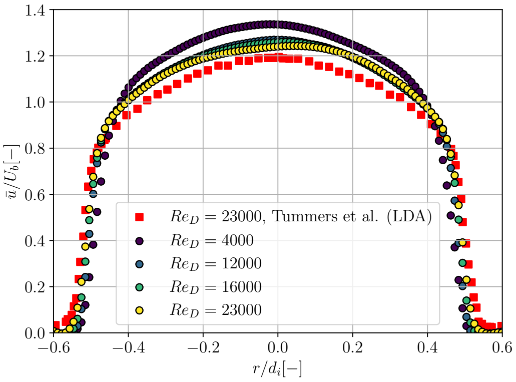

(a) The dimensionless mean in axial velocity profile $\overline{u}/U_b$, was obtained $0.19d_i$ downstream from the exit of the tube. The reference LDA data used for these measurements was provided by Tummers et al. [60]

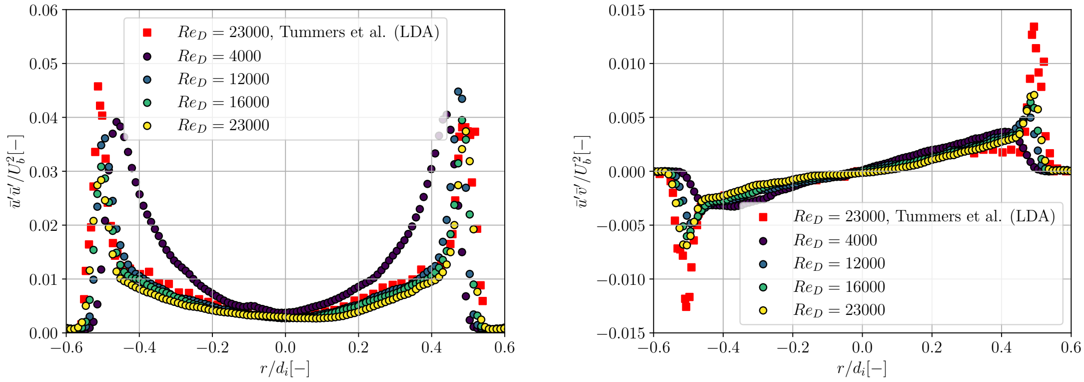

(b) The dimensionless Reynolds stress profile in axial direction $\overline{u}'\overline{u}'/U_b$, was obtained $0.19d_i$ downstream from the exit of the tube. The reference LDA data used for these measurements was provided by Tummers et al. [60].

(c) The dimensionless Reynolds shear stress profile $\overline{v}'\overline{v}'/U_b$, was obtained at a distance of $0.19d_i$ downstream from the exit of the tube. The reference LDA data used for these measurements was provided by Tummers et al. [60].

Figure 4.1: Cold Flow Results

Figure 4.1 represents dimensionless results of the turbulent pipe flow were compared with measurements taken $0.19d_i$ downstream from the tube exit. Primarily, the focus was on the profile of dimensionless mean axial velocity. Figure 4.1a shows the dimensionless mean axial velocity profiles ($\overline{u}/U_b$) as measured both PIV for four Reynolds numbers between 4000 and 23000 and the reference data at Re_D = 23000 were taken from Tummers et al [60]. There is an expected deviation in the centerline of the flow, where PIV results on centerline decreases with increasing Reynolds number. However, values of r/di between -0.4 and -0.6, as well as 0.4 and 0.6 (outside tube region), accurately captured the flow normalized velocity characteristics. Particularly, in the regions of r/di between -0.4 and -0.6, as well as 0.4 and 0.6, the PIV and LDA results converged closely, thereby accurately capturing the flow's normalized velocity characteristics. The Reynolds stress as shown in the axial direction in Figure 4.1b, denoted by $\overline{u}'\overline{u}'/U_b$, was investigated. It provides a measure of the intensity of turbulent fluctuations along the flow direction. The core flow was accurately captured, with peaks observed around $r/di = \pm 0.5$. The magnitude of the differences for these peaks in terms of fluctuations in the axial direction was smaller than 0.01, indicating a good agreement. Notably, these peaks, indicative of the heightened turbulent activity within the flow, are largely attributable to the higher spatial resolution of LDA. The analysis also incorporated the shear Reynolds stress Figure 4.1c, denoted as $\overline{v}'\overline{v}'/U_b$. This parameter represents the interactions between the velocity components in radial direction. It provides a measure of the intensity of turbulence that contributes to the momentum transfer in radial direction of the pipe. The flow core and the approximately linear behavior between $r/di = \pm 0.4$ were well captured. Similarly with Figure 4.1b, peaks around $r/di = \pm 0.5$ exhibited a maximum deviation of 0.005, representing accurate measurement of both radial and axial fluctuations.

4.3. Turbulent Flames Characteristics

After accomplishing the validation studies based on turbulent flow dynamics, primary focus turned to the variations in turbulent characteristics between different fuel types, specifically H_2 and DNG flames. The research encompassed an in-depth study of four distinct flames categorized by considering 4.2, while keeping unstretched laminar flame speed as constant for each flame cases as previously mentioned as previously mentioned. Within the scope of different fuel type, utilizing the same quartz tube with an inner diameter of 25.16 mm, premixed flames have been performed with fully developed flow and without preheating. Each of these was further differentiated based on their stability condition. To further analyze and document the flame characteristics, contour maps were generated by averaging 5000 images with an interrogation window size of 16x16 pixels and zero overlap between consecutive windows.

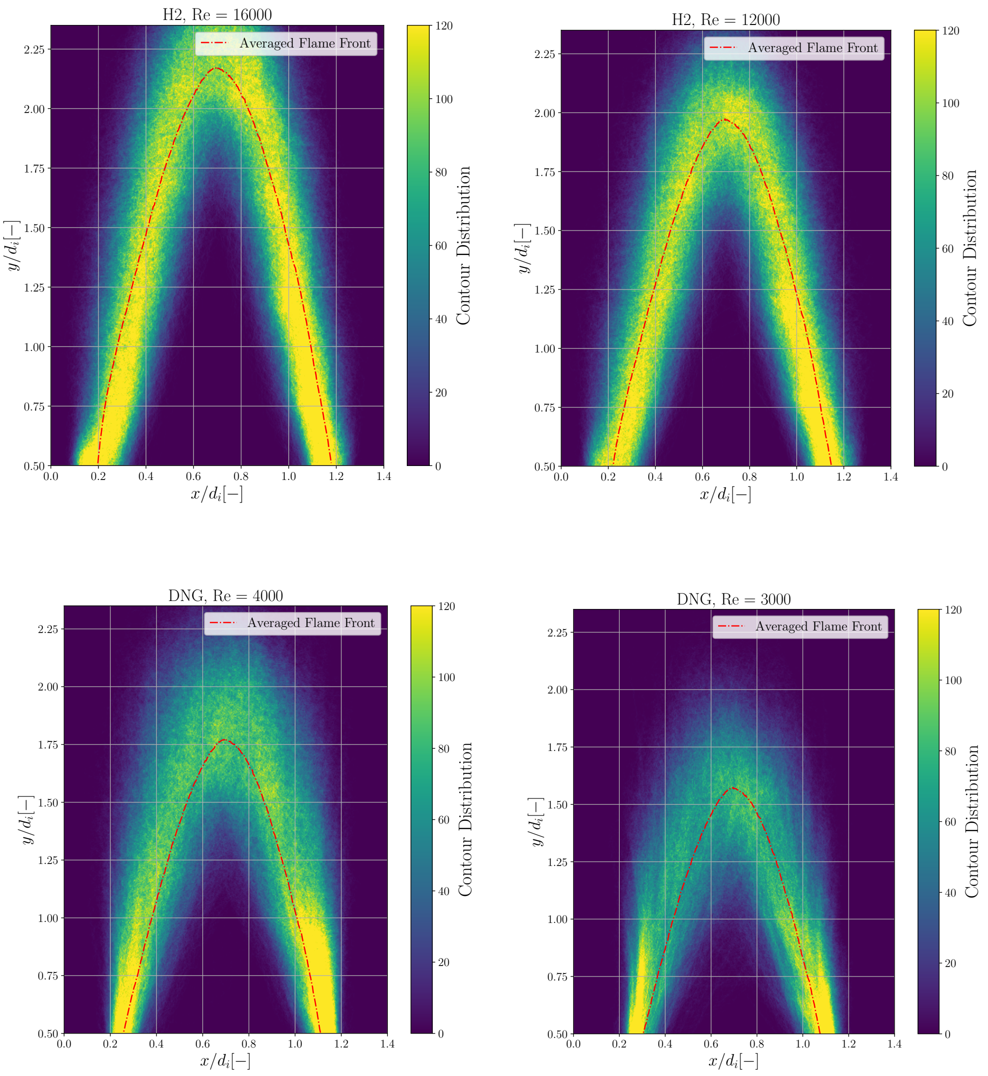

Figure 4.2: Comparative Analysis of Flame Front Distributions: Each subplot showcases intensity distribution (left), the corresponding averaged flame front (right)

The presented Figure 4.2 shows Mie-scattering intensity for flame front contour distribution [-] across 1000 images and averaged positioning of the segmented flame front with red dashed line. Upon analyzing the Mie-scattering intensity, it has observed that H_2 flames exhibit notably higher intensities, reaching around a value of 120. This increased intensity is indicative of the scattering characteristics of H_2 flames considering elevated Reynolds number. On the other hand, DNG flames show a reduced image intensity, particularly noticeable at the flame tip. Another aspect revealed contrasting the distribution of the flame front contours, where H_2 flames exhibit a more stationary Mie-scattering intensity. In contrast, DNG flames demonstrate a higher degree of variability in the positions of their flame front contours. In terms of the averaged flame front, H_2 flames demonstrate a tendency to cover larger areas, a phenomenon that can be attributed to their operation at higher Reynolds numbers. It is important to note that as the Reynolds number decreases, there's a corresponding reduction in the average flame front area. This reduction is not just limited to the size but also influence to its positioning along the axial and radial axes. Additionally, an agreement yields on flame contour distributions and averaged flame front positioning. This agreement is mostly captured in the vicinity of the approximate flame front, where the contours from different flame types show a remarkable degree of overlap.

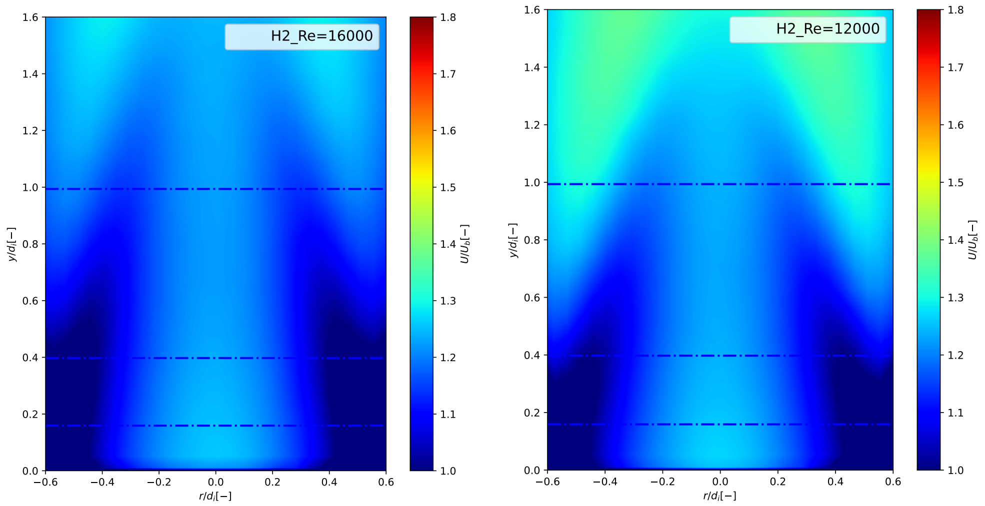

(a) Dimensionless Absolute Velocity Field U/U_b for Stable H2 Flame, $\Phi = 0.49$, $S_{l0} = 0.365ms^{-}1$, and $Re = 16000$

(b) Dimensionless Absolute Velocity Field U/U_b for H2 Flame Close to Flashback, $\Phi = 0.49$, $S_{l0} = 0.365ms^{-}1$, and $Re = 12000$

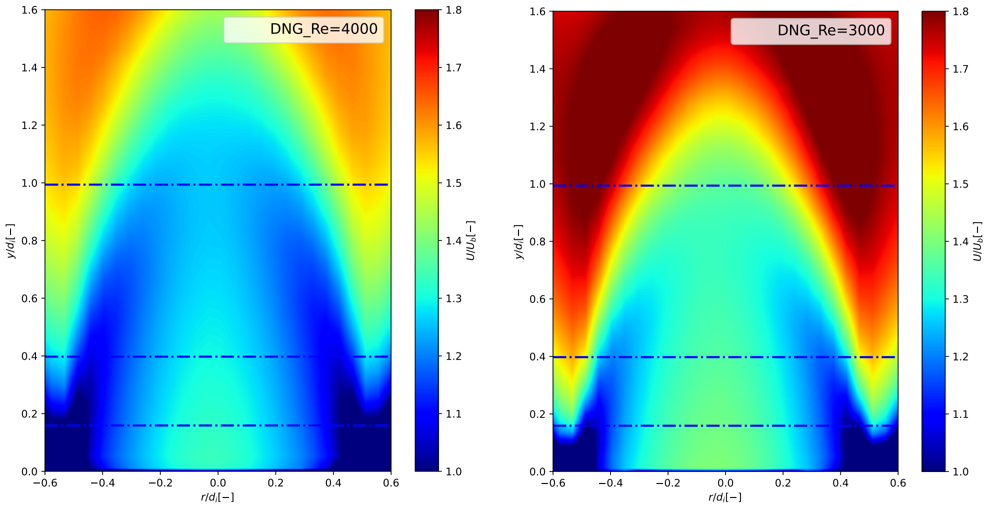

(c) Dimensionless Absolute Velocity Field U/U_b for Stable DNG Flame, $\Phi = 0.49$, $S_{l0} = 0.365ms^{-}1$, and $Re = 16000$

(d) Dimensionless Absolute Velocity Field U/U_b for DNG Flame Close to Flashback, $\Phi = 1$, $S_{l0} = 0.365ms^{-}1$, and $Re = 3000$

Figure 4.3: Comparative visualization of the dimensionless absolute velocity contours for H2 and DNG flames.

Figure 4.3 shows the dimensionless absolute velocity contours for hydrogen (H2) and DNG flames under conditions close to flashback and stable combustion. Axes of both y/di and r/di denote the dimensionless axial and radial coordinates for all flames, respectively. The absolute velocity was dimensionless by the corresponding bulk velocities as depicted in Table 4.2. Upon an examination of the contour diagrams, a clear pattern of progression is discernible in the normalized absolute velocities as transitioned from the H2 case to DNG while decreasing Re number, specifically in the regions approximate the flame front vicinity. Higher dimensionless absolute velocities indicate that the local velocity at specific points in the flow field is higher compared to the bulk velocity. These variations in velocity within the flow field may lead to velocity gradients, which can contribute to the generation of turbulence. For the DNG flames, there is a marked increase in velocity in the vicinity of the flame front, notably more substantial than that observed for the H_2 flames. This heightened velocity gradient in the DNG flames is primarily due to the stoichiometric equivalence ratio ($\phi = 1$), which indicates complete combustion reactions and consequently leads to a steep increase in velocity. In contrast, the H_2 flames are characterized by a leaner mixture with an equivalence ratio of $\phi = 0.49$, resulting in a more gradual velocity profile. The differences in the equivalence ratios of the two fuels result in distinct combustion dynamics, as evidenced by the variation in the velocity contours, with the stoichiometric DNG flame creating conditions that complete combustion and increased potential tendency of flashback compared to the leaner H_2 flame. In Figure 4.3, the dimensionless absolute velocity contours have overlaid with dashed lines which demonstrate the cross-sections taken at three specific heights—namely y/di [-] ratios of 0.19, 0.38, and 1. These cross-sections offer invaluable insight into the evolution dimensionless mean velocity in order to capture identical consistency as completed in cold flow profiles.

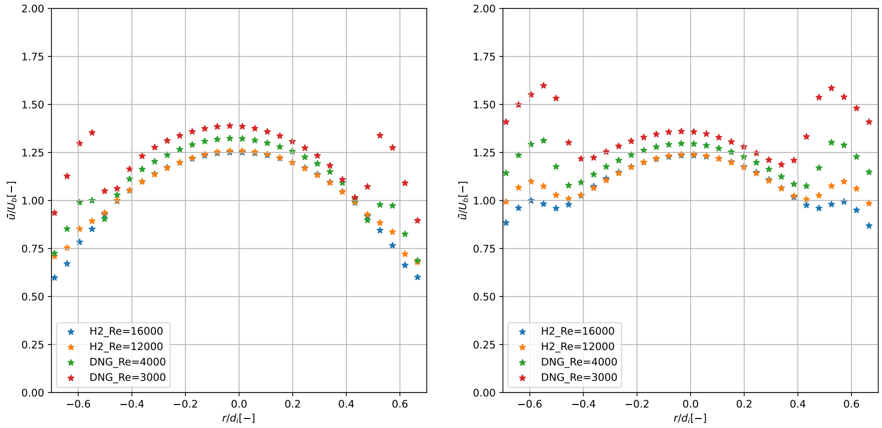

(a) Comparison of the normalized mean velocity profiles $\overline{u}/U_b$ for DNG and H2 flames. Graph was obtained at a distance of $0.19d_i$ downstream of the tube's exit.

(b) Comparison of the normalized mean velocity profiles $\overline{u}/U_b$ for DNG and H2 flames. Graph was obtained at a distance of $0.4d_i$ downstream of the tube's exit.

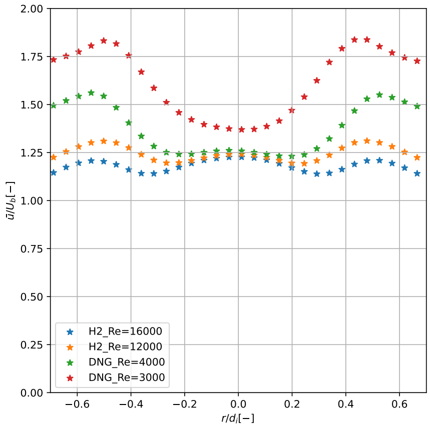

(c) Comparison of the normalized mean velocity profiles $\overline{u}/U_b$ for DNG and H2 flames. Graph was obtained at a distance of $1d_i$ downstream of the tube's exit.

Figure 4.4: Comparative display of normalized velocity profiles at three different cross-sections in hydrogen and DNG flames.

Figure 4.4 represents velocities are normalized by their corresponding bulk velocities. To demonstrate the similarity of the cold flow mean velocity profiles as seen in Figure 4.3 and flame characteristics, it is observed that the flame with the lower Reynolds number presents a higher dimensionless mean velocity profile along the center-line region of the burner. An examination of the lower cross-section $y/di = 0.19$ for DNG flame with Re=3000 case reveals highest non-uniformity between the core region and shear layer. This deviation from uniformity suggests an unstable flame condition and signifies a reaction zone is closest to the burner rim due to lower Reynolds number. Comparing the center-line characteristics to those of the cold flow reveals a distinct trend. The normalized mean velocities predominantly lie within the range of 1.2 to 1.4. As the Reynolds number increases, the ratio $\overline{u}/U_b$ decreases, mirroring the observations made in the cold flow characteristics. Specifically, examining the shear layer of the plot reveals obvious flame behaviors. For hydrogen flames, due to the higher Reynolds number, velocity jumps on the shear layer are smaller than DNG flames. Especially for DNG flame with Re = 3000, anomalies at the shear layer suggest the occurrence of the flame front at $0.19d_i$ close to the burner rim. However, as we move to higher cross-sections (y/di = 0.4), the shear layer's for normalized velocity starts to dominate over the core region across all flame types. This dominance becomes more apparent at the top cross-section (y/di = 1), suggesting intensified flame-environment interactions at these higher positions.

Another physical property of the flow called divergence, a vector operation that captured on a vector field, providing a scalar field as a unit of [1/s]. In fluid dynamics, divergence is often used to describe the extent to which a flow expands or compresses. More specifically, the divergence at a given point in the vector field describes the rate at which ”density variation” exits at that point. In 2-D Cartesian (x, y) and cylindrical coordinates (r,θ). The divergence field can be determined as;

$$\nabla \cdot (u, v) = \frac{\partial u}{\partial x} + \frac{\partial v}{\partial y} = \frac{1}{r}\frac{\partial (rV_r)}{\partial r} + \frac{1}{r}V_\theta \tag{4.1}$$

Normalized divergence offers a way to compare flow properties across different flames, taking into account variations due to tube diameter and bulk velocity. The normalization procedure is based on the equation:

$$\nabla \cdot (u*, v*) = \frac{1}{U_b/d_{in}}\left(\frac{\partial u}{\partial x} + \frac{\partial v}{\partial y}\right) = \frac{1}{U_b/d_{in}}(\frac{1}{r}\frac{\partial (rV_r)}{\partial r} + \frac{1}{r}V_\theta) \tag{4.2}$$

This equation provides a non-dimensional view of divergence, normalizing with respect to the bulk velocities and the tube's inner diameter.

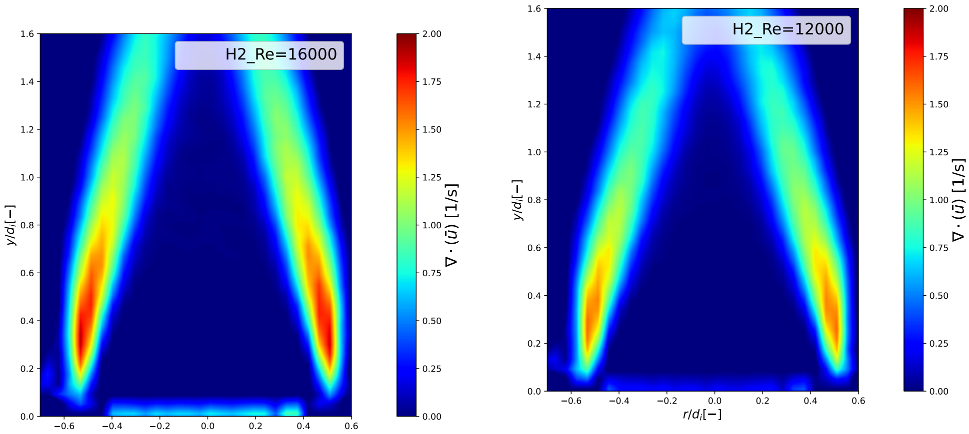

(a) Divergence field $\nabla \cdot (u, v)$ for stable H2 flame, $\Phi = 0.49$, $S_{l0} = 0.365ms^{-}1$, and $Re = 16000$

(b) Divergence field $\nabla \cdot (u, v)$ for H2 flame close to flashback, $\Phi = 0.49$, $S_{l0} = 0.365ms^{-}1$, and $Re = 12000$

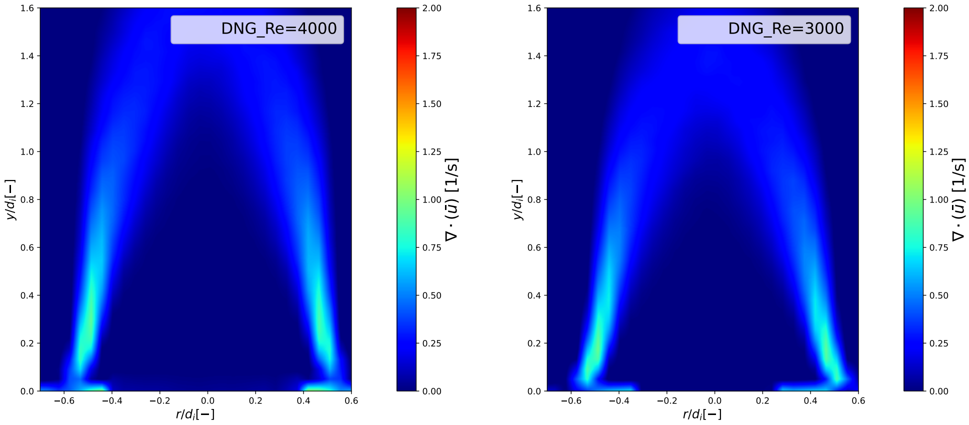

(c) Divergence field $\nabla \cdot (u, v)$ for stable DNG flame, $\Phi = 1$, $S_{l0} = 0.365ms^{-}1$, and $Re = 4000$

(d) Divergence field $\nabla \cdot (u, v)$ for DNG flame close to flashback, $\Phi = 1$, $S_{l0} = 0.365ms^{-}1$, and $Re = 3000$

Figure 4.5: Visualization of the divergence field within DNG and H2 flames, illustrating the variations in flame spreading and diffusive behavior.

The analysis of the divergence contours, as displayed in Figure 4.5, reveals zones of high divergence predominantly on the sides of the flames rather than their tips. Notably, H_2 flames exhibit pronounced divergence values with reaching up to $1.89[1/s]$ and $1.607[1/s]$, as seen in Table 4.3. These high values can be attributed to its sharp velocity gradients without normalization between burnt and unburnt regions, resulting in the observed high rates of flow expansion. While H_2 flames initially display pronounced velocity jumps characterized by significant divergence values, a closer examination of the dimensionless divergence values reveals that it is actually the DNG flames that exhibit higher velocity jumps.

Table 4.3: Max Divergence and Normalized Divergence Values for Each Flame

Flame	Max Divergence [1/s]	Max Normalized Divergence [-]
H_2, Re = 16000	1.89	0.0041
H_2, Re = 12000	1.61	0.0046
DNG, Re = 4000	0.93	0.0094
DNG, Re = 3000	0.96	0.0130

A closer look at the data in Table 4.3 shows that the DNG flame at Re=3000 exhibits the highest normalized divergence. High normalized divergence values underscore enhanced flow expansion rates, indicating complex interplay between turbulent flow and flame. The variation observed in both divergence and normalized divergence across the different flames can be significantly influenced by their equivalence ratios. Complete combustion evolves at stoichiometric conditions for DNG flames, is characterized by a higher adiabatic flame temperature due to the complete combustion of DNG flames. In turn, this elevated flame temperature amplifies the kinetic energy of the gas molecules [43], causes a more robust expansion of the combusted gases.

TKE was identified as a measure of changes in fluid velocity. For clear comparison across different flame setups, TKE values were made dimensionless with the flame's corresponding bulk velocity U_b. In H_2 flames, changes in flame behavior were seen in areas with high TKE. The normalized TKE for the four flame cases ranged from 0.02 in the H_2 Re=16000 flame to 0.18 in the DNG Re=3000 flame. The normalized TKE, different from the absolute TKE values, reflects the turbulence intensity level. This distinction positions it as an indication for gauging turbulence levels across various flames and flow conditions, regardless of their inherent dimensions.

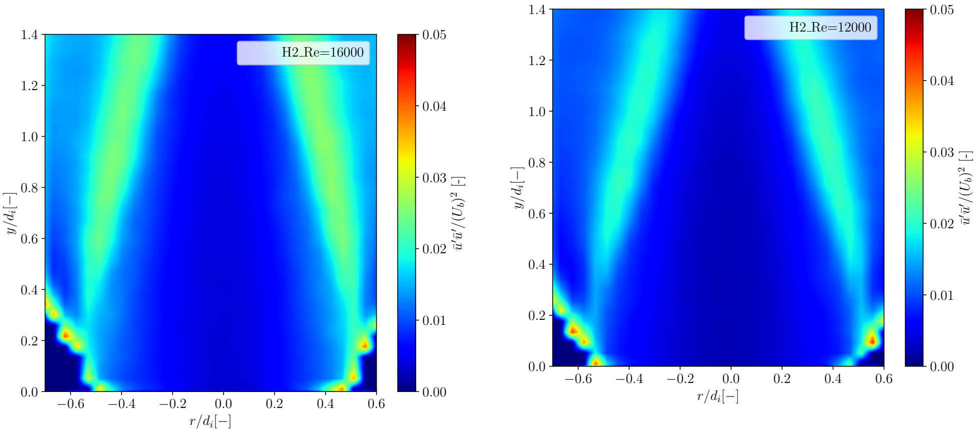

(a) Turbulence Kinetic Energy for stable H2 flame, $\Phi = 0.49$, $S_{l0} = 0.365ms^-1$, and $Re = 16000$

(b) Turbulence Kinetic Energy for H2 flame close to flashback, $\Phi = 0.49$, $S_{l0} = 0.365ms^-1$, and $Re = 12000$

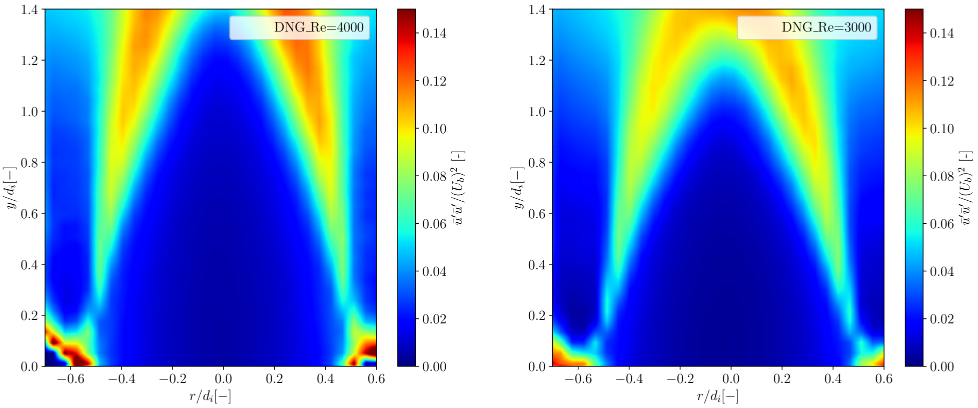

(c) Turbulence Kinetic Energy for stable DNG flame, $\Phi = 1$, $S_{l0} = 0.365ms^-1$, and $Re = 4000$

(d) Turbulence Kinetic Energy for DNG flame close to flashback, $\Phi = 1$, $S_{l0} = 0.365ms^-1$, and $Re = 3000$

Figure 4.6: Comparative depiction of the turbulence kinetic energy within DNG and H2 flames, highlighting differences in the energy dissipation due to turbulence.

As depicted in Figure 4.6, the contours represent the normalized Turbulent Kinetic Energy

(TKE) within DNG and H_2 flames, showcasing the differences in kinetic energy dissipation due to turbulence. Normalization of the TKE has been carried out using the bulk velocities. In this particular study, the unstretched laminar flame speed (S_{L0}) is held constant for both DNG and H_2 flames, by varying the Reynolds number. When examining DNG flames, it is observed that higher Reynolds numbers correlate with higher normalized TKE especially around flame tip, suggesting that increased turbulence levels enhance normalized kinetic energy within the flow field. However, a contrast is evident when comparing DNG to H_2 flames. Despite DNG flames operating at lower Reynolds numbers, they exhibit a higher level of normalized TKE than H_2 flames. It can be connected to the equivalence ratio adjustments, made to achieve constant unstretched laminar flame speeds, result in different stoichiometric mixtures that naturally effects the combustion dynamics. The faster chemistry and thinner reaction zones associated with hydrogen combustion tend to be less influenced by turbulence, thus exhibiting lower normalized TKE.

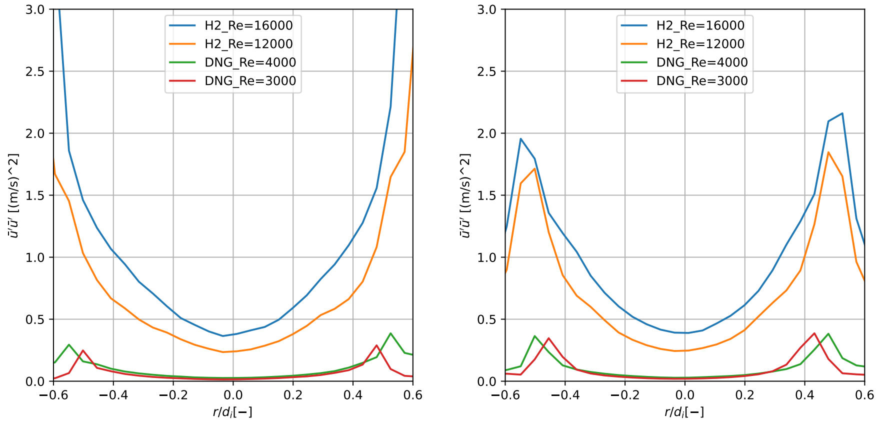

(a) Comparison of the TKE m^2/s^2 profiles for DNG and H2 flames. Graph was obtained at a distance of $0.19d_i$ downstream of the tube's exit.

(b) Comparison of the TKE m^2/s^2 profiles for DNG and H2 flames. Graph was obtained at a distance of $0.4d_i$ downstream of the tube's exit.

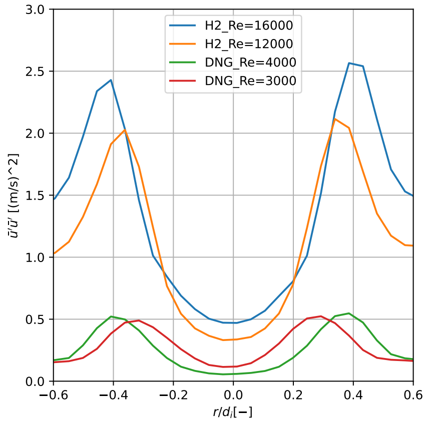

(c) Comparison of the TKE m^2/s^2 profiles for DNG and H2 flames. Graph was obtained at a distance of $1d_i$ downstream of the tube's exit.

Figure 4.7: Comparative display of TKE m^2/s^2 profiles at three different cross-sections.

Figure 4.7 shows measured TKE values from different heights above burner. Non-dimensional values of the TKE represent the raw turbulence levels or intensities within each flame. An increasing Reynolds number usually correlates with enhanced turbulence levels. Therefore, higher Reynolds number flames might display increased TKE values due to more pronounced velocity fluctuations and subsequent turbulent mixing. While H_2 flames consistently register higher turbulence intensities, the DNG flames exhibit a nuanced behavior, especially in the core region. An intriguing contrast is witnessed in the core region, where H_2 flames with a higher Reynolds number produce more TKE. In contrast, for the DNG flames, with the flame of lower Reynolds number showing a higher TKE.

4.3.1. Turbulent Flame Regimes

To construct the Borghi diagram, four fundamental parameters were calculated for each flame in this study. First, the root-mean-square velocity fluctuation ($u_{rms} = \sqrt{u'^2}$) was determined to quantify turbulent intensity. (u_{rms}) were calculated to quantify with employing the formula $u_{\text{rms}} = (0.004U_b^2)^{0.5}$, in alignment with [5]. For the correction of the u_{rms}, results in cold flow measurements has been checked considering the $\bar{u}'\bar{u}'/U_b^2$ values at centerline. For the flows with Reynolds number 4000 and 12000, u_{rms} values becomes 0.176 m/s and 0.550 m/s, respectively. In the current formulation with $u_{\text{rms}} = (0.004U_b^2)^{0.5}$, flames with Reynolds number 4000 and 12000 results u_{rms} = 0.117 m/s and 0.575 m/s aligning closely with the observed data, as further listed in Table Table 4.4 for the other flames. Furthermore, the laminar flame speed (S_{L0}) was computed with Cantera 1D simulation, resulting in $S_{L0} = 0.365m/s$ for each mixture. The approach towards the turbulent flame regimes began with the computation of turbulent length and velocity scales for each flame mixture. The integral length scale (l_0), indicative of the characteristic size of turbulent eddies, was computed as $l_0 = 0.13\frac{d_i}{2}$ [45]. For the computation of flame thickness (δ_F), three non-dimensional parameters were considered necessary.

$$Le = \frac{\alpha}{D}, \quad Sc = \frac{\nu}{D}, \quad Re = \frac{u'l_0}{\nu} \tag{4.3}$$

Where The Schmidt number is the ratio of kinematic viscosity (ν) to mass diffusivity (D). While the Reynolds number of the flames was known, the computation of Lewis Number (Le) and Schmidt Number (Sc) required reference to empirical approximations suggested by [27], assumed values further depicted in Table Table 4.4. Subsequently, δ_F was computed using the formula:

$$\delta_F = \frac{\alpha}{S_{L0}} = \frac{Le \cdot D}{S_{L0}} = \frac{Le \cdot \frac{\nu}{Sc}}{S_{L0}} = \frac{Le \cdot \frac{u'l_0}{Sc \cdot Re}}{S_{L0}} = \frac{Le \cdot u'l_0}{Sc \cdot Re \cdot S_{L0}} \tag{4.4}$$

The computed flame thickness values for the respective flames are as follows:

Flame	Lewis Number (Le) [-]	Schmidt Number (Sc) [-]	Flame Thickness (δ_F) [m]	u_{rms} [m/s]
$DNG_{Re=3000}$	0.98	0.68	2.518×10^{-7}	0.117
$DNG_{Re=4000}$	0.98	0.68	2.542×10^{-7}	0.157
$H2_{Re=12000}$	0.29	0.21	2.968×10^{-7}	0.576
$H2_{Re=16000}$	0.29	0.21	2.847×10^{-7}	0.736

Table 4.4: Computed values of Lewis Number, Schmidt Number, Flame Thickness, and u_{rms} for each flame.

As a summary, the table Table 4.4 shows the key parameters for four different flames, each identified by its respective Reynolds number. The Lewis Number (Le) and Schmidt Number (Sc) for each flame are provided, based on empirical approximations [27]. The flame thickness (δ_F) is calculated using formulation that incorporates these numbers along with other flame-specific variables. Additionally, the root mean square velocity fluctuations (u_{rms}) for each flame are listed and constructed into Borghi diagram.

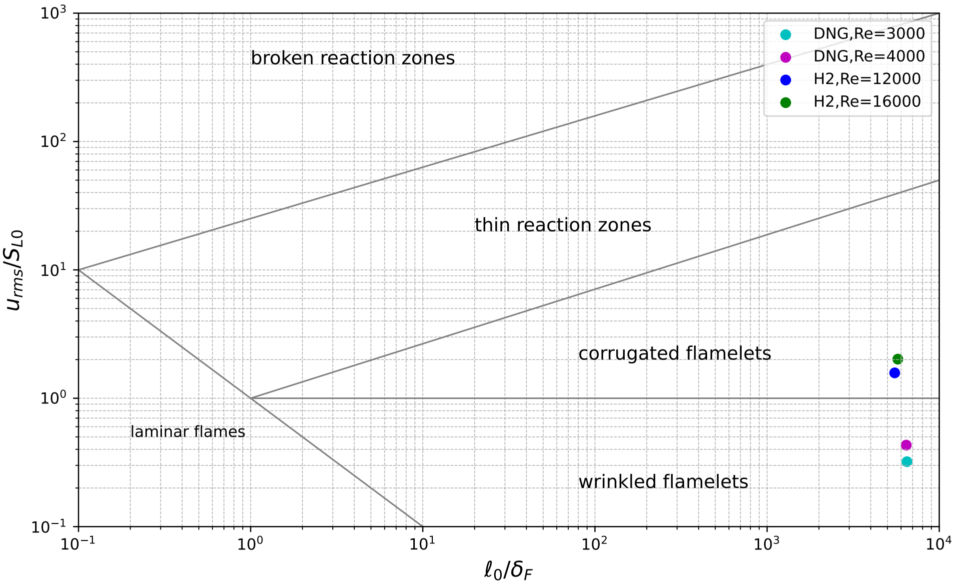

Figure 4.8: Borghi Diagram of the corresponding flames; DNG Re = 3000 (cyan), DNG Re = 4000 (purple), H2 Re = 12000 (blue), H2 Re = 16000 (green).

As previously discussed Figure 2.10 in Section 2.4, the position of H_2 and DNG flame regimes in the Borghi diagram indicates different turbulence-flame interaction and flame front characteristics in the perspective of characteristic velocity and length scale ratios. H_2 flames for the given conditions, fall within the **corrugated flamelets** regime (Re > 1, Ka < 1, $u' > S_L$). In this regime, the turbulence intensity u' being greater than the laminar flame speed S_L causes the flame front to become corrugated with smaller flame cusps. This leads to an increased total surface area of the flame, which can enhance the turbulent flame speed. Conversely, natural gas flames, as seen in Figure 4.8, are located in the **wrinkled flamelets** regime (Re > 1, Ka < 1, $u' < S_L$). Here, the turbulence intensity is less than the laminar flame speed, resulting in a flame front that is wrinkled but not intensely corrugated.

4.4. Quantitative Analysis of Flame Kinematics

In this section, the flame kinematics of the flames referred to as DNG and H_2 will be discussed. DNG and H_2 flames have been recorded using high-speed imaging technique to enable more accurate evaluation of the flame front. Ultimately, superimposing captured flame fronts with corresponding velocity maps from PIV experiment will structure the basis of the methodology. In the Section (3.4) and Section (3.5), the data statistics are based on the selected segments each 1 mm of constant longitude.

4.4.1. Flame Slope-Change and Local Curvature Analysis

The discussions are based on the flames which represent DNG and H_2 flames under stable conditions and flames close to the point of flashback. Following the application of a segment selection procedure to the flame front images which has been captured in Section (3.5), majority of the segments have been eliminated due to no intersection detected in between segments and flow velocity components. That results a refined set of individual segments for analysis. In order to assess the complexity of these remaining segments, a method was employed to quantify the magnitude of slope change in Section (3.6.2). For each individual segment, slope change calculation has been identified in Section (3.4.1) with Equation 3.7 considering spatial orientation of 2 consecutive segments. Furthermore, local curvature of the flame front which is examined in Section (3.4.2) with Equation 3.8 determines detected segment's local curvature value which will be discussed under histogram representation for each flame.

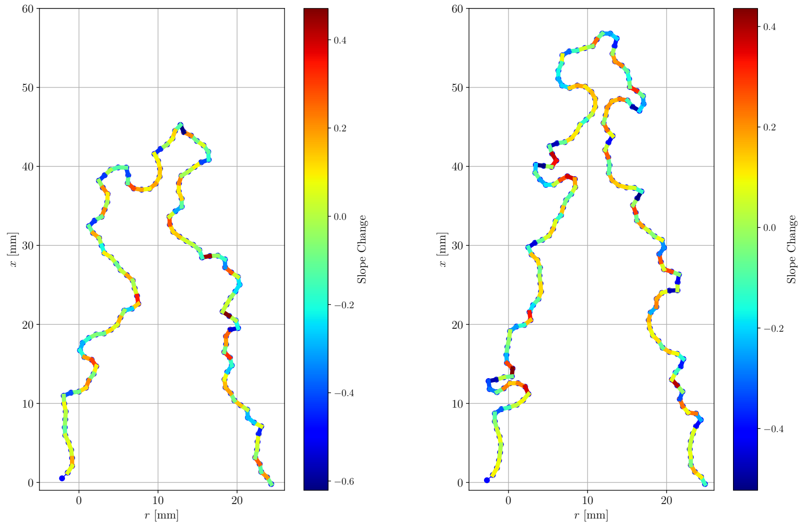

(a) Contour representation of slope change on flame front for H2 Flame at Re = 12000, $\phi = 0.49$

(b) Contour representation of slope change on flame front for H2 Flame at Re = 16000, $\phi = 0.49$

Figure 4.9: Instantaneous flame fronts of H_2 flames. The color denotes the local value of slope change.

Figure 4.9 shows H_2 flames slope change values based on instantaneous flame front. The H_2 flames are characterized by the formation of smaller flame cusps. There are regions on the flame front that experience both maximum and minimum slope changes, underlining the fluctuating slope change values of the H_2 flame front. As a result, this leads to a higher degree of variability in the slope change between segments.

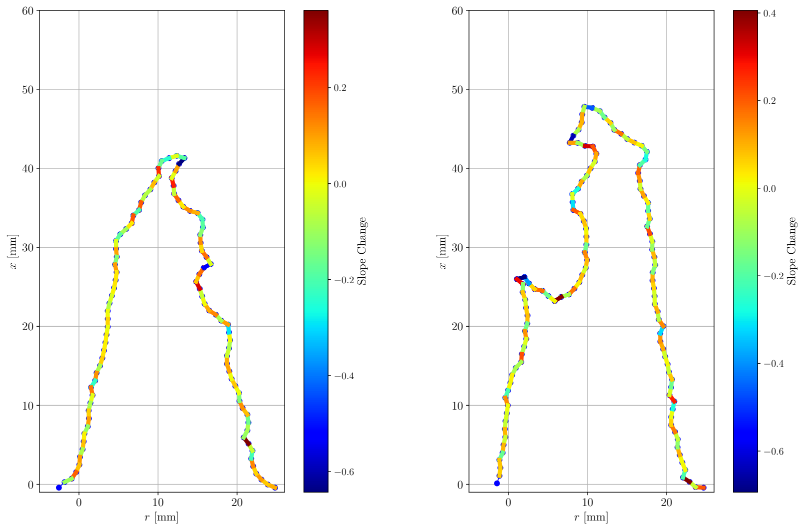

(a) Contour representation of slope change on flame front for DNG Flame at Re = 3000, $\phi = 1$

(b) Contour representation of slope change on flame front for DNG Flame at Re = 4000, $\phi = 1$

Figure 4.10: Instantaneous flame fronts of DNG flames. The color denotes the local value of slope change.

Figure 4.10 shows instantaneous snapshots of DNG flames. DNG flames exhibit maximum slope change predominantly in regions with larger flame cusp formations. Notably, the sides of the DNG flames display a relatively flat segment formation, resulting in a uniform slope change. This uniformity in segment formation suggests a higher likelihood of encountering areas on the flame front with near-zero curvature. An observation for H_2 and DNG flames yields on the effect of Reynolds number on flame front area, exhibits a correlation with the Reynolds number. As the Reynolds number increases, the number of segments on the flame front also increases. This suggest that higher Reynolds numbers contribute to an increment the overall flame front area and elevation of flame tip.

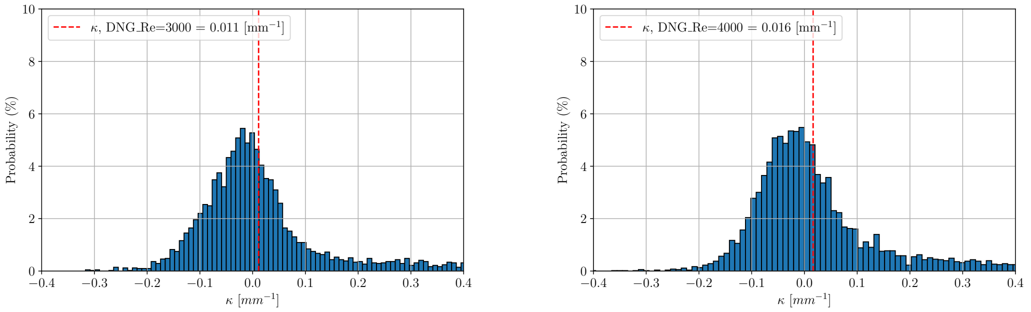

(a) Probability Distribution of κ for DNG Flame at Re = 3000, $\phi = 1$

(b) Probability Distribution of κ for DNG Flame at Re = 4000, $\phi = 1$

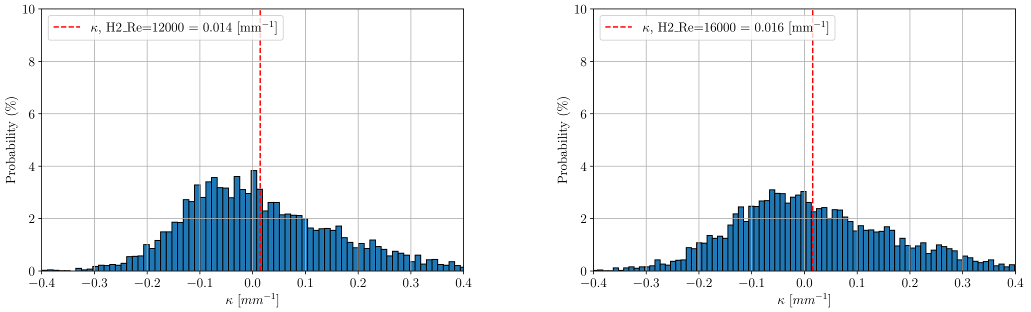

(c) Probability Distribution of κ for H2 Flame at Re = 12000, $\phi = 0.49$

(d) Probability Distribution of κ for H2 Flame at Re = 16000, $\phi = 0.49$

Figure 4.11: κ distribution on x-axis considering slope change average on detected segments, represented by 4 different flames. Probability on y-axis represents the amount of values corresponding probability out of 100%.

Figure 4.11 represents four histograms to show the distribution of a quantity called local curvature of flame front segments denoted as κ measured in $mm^{-}1$. The data is presented as a probability distribution, with the probability on the y-axis and the κ values on the x-axis. The dotted red vertical lines indicate the average value of κ for each distribution. In Figure 4.11a and in Figure 4.11b, the average shifts slightly right as the Re increases from 3000 to 4000, implying a change in the average local curvature with flow conditions. Similarly, in Figure 4.11c and Figure 4.11d, the average is at the same location, which could suggest that changes in Reynolds number from 12000 to 16000 did not affect the central tendency of κ for the H_2 flame. A positive mean value in the histograms indicate that, on average, the flame front segments tend to curve towards to the unburnt side. In the physical sense, this could suggest that the predominant direction of curvature is concave when looking from a certain side of the flame front.

In terms of skewness values of the histograms, the spread of the histograms in Figure 4.11a and Figure 4.11b seems to increase with a higher Reynolds number, suggesting more variability in κ at Re = 4000 compared to Re = 3000. There is a slight positive skewness in both DNG flames, indicating that linear segments have been detected is more probable than segments with curved formations on DNG flame front. For hydrogen flames, both Figure 4.11c and Figure 4.11d have similar spreads, suggesting consistent variability in κ with changes in the Reynolds number. These distributions also appear slightly positive-skewed. Additionally, the broader histograms for H_2 flames compared DNG flames suggest that the H_2 flame fronts experience a wider range of local curvature values. The broader distribution indicates that both large positive and large negative curvature values are more common in H2 flames than in DNG flames. This broader range of curvature could be indicative of a direct correlation between the rate of slope change and local curvature, as illustrated in Figure 4.9 and Figure 4.10.

4.4.2. Local Flame Dynamics

In addition to analyzing flame front segmentation, we also examined the histograms for local flame dynamics to gain insights into the characteristics of the flames. The histograms provide valuable information about the distribution and variations in the local flame speed, local displacement speed and local flow velocity in normal and tangential directions to the segments across the flame fronts.

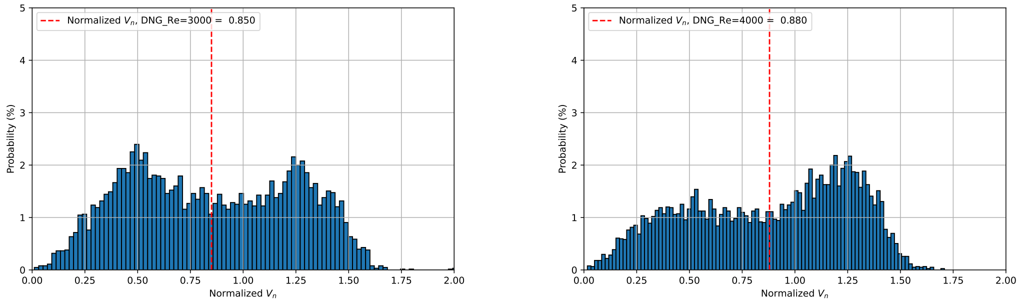

(a) Probability Distribution of normalized local flow normal velocity (V_n) for DNG Flame at Re = 3000, $\phi = 1$

(b) Probability Distribution of normalized local flow normal velocity (V_n) for DNG Flame at Re = 4000, $\phi = 1$

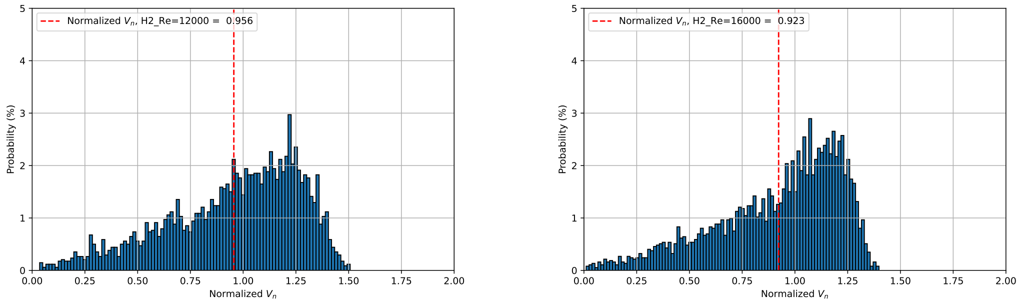

(c) Probability Distribution of normalized local flow normal velocity (V_n) for H2 Flame at Re = 12000, $\phi = 0.49$

(d) Probability Distribution of normalized local flow normal velocity (V_n) for H2 Flame at Re = 16000, $\phi = 0.49$

Figure 4.12: Dimensionless flow normal velocity V_n/U_b distribution for different flames. Probability on y-axis represents the amount of values corresponding probability out of 100%.

Figure 4.12 shows the distribution of the dimensionless local flow velocity values for DNG and H_2 flames, which was previously described in Chapter (3.5). A slight increase in the averaged values of dimensionless V_n with rising Reynolds numbers was observed in DNG flames as seen in Figure 4.12a and Figure 4.12b. H_2 flames at Re of 12000 and 16000 have been demonstrated in Figure 4.12c and Figure 4.12d, where the average V_n remains relatively unchanged. This could imply that within the Re range, the average dimensionless V_n is not markedly influenced by the turbulence intensity.

Comparing the skewness of the distributions for DNG flames, we observe a similar probability density around a V_n value of 1.25. However, for the DNG flame at the lower Re of 3000, there is a noticeable increase in probability around a V_n value of 0.5, indicating that lower V_n values are more prevalent. Looking at the skewness of the distributions for H_2 flames, the histograms show a narrower spread of dimensionless local flow normal velocity (V_n) compared to the DNG flames. This means that for H_2 flames, there is less variability in the flow velocities across the flame front. The histograms are still negatively skewed, indicating there are higher dimensionless (V_n) values more probable than lower values.

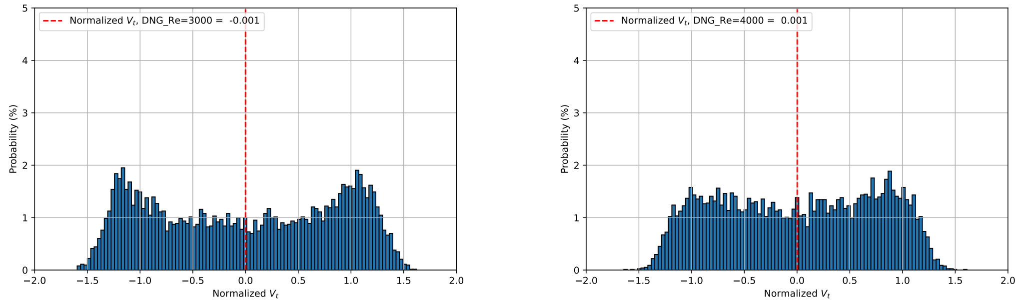

(a) Probability Distribution of normalized local flow tangential velocity (V_t) for DNG Flame at Re = 3000, $\phi = 1$.

(b) Probability Distribution of normalized local flow tangential velocity (V_t) for DNG Flame at Re = 4000, $\phi = 1$.

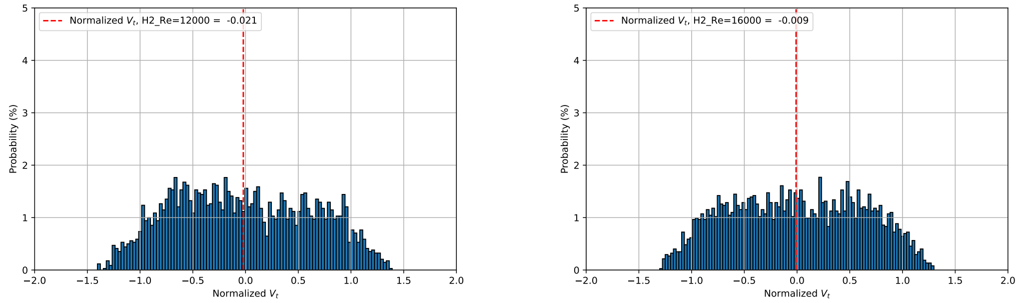

(c) Probability Distribution of normalized local flow tangential velocity (V_t) for H2 Flame at Re = 12000, $\phi = 0.49$.

(d) Probability Distribution of normalized local flow tangential velocity (V_t) for H2 Flame at Re = 16000, $\phi = 0.49$.

Figure 4.13: Normalized Vt with U_b distribution on x-axis considering flow velocity decomposition in tangential direction on detected segments, represented by 4 different flames. Probability on y-axis represents the amount of values corresponding probability out of 100%.

Figure 4.13 shows the distribution of dimensionless tangential velocity component V_t, which reveals that the tangential velocities. Flow velocities have been constructed in Chapter (3.5) and V_t as a tangential component of flow velocity which assumed to be parallel to the flame front segments. The average dimensionless V_t values close to zero for all flames as seen in the histograms, further affirming the balanced nature of the tangential velocities in between right and left hand side of the flames. All flames displayed symmetrically skewness in their dimensionless V_t values for DNG and H_2 flames. Particularly, negative dimensionless V_t values are located on the right-hand side of the flame origin, and positive values on the left, adhering to the conventions of the cartesian or cylindirical coordinate system.

The histograms suggest that DNG flames as seen in Figure 4.13a and Figure 4.13b exhibit a broader range of dimensionless tangential velocity (V_t) values compared to H_2 flames as illustrated in Figure 4.13c and Figure 4.13d. The existence of broader ranges in dimensionless V_t values for DNG flames suggests that large positive and large negative V_t are more probable when compared to the bulk velocities. This could imply that the local dynamics of the flow field have a stronger influence on the flame front for DNG flames than for H_2 flames. Recalling the turbulent characteristics of the flames as previously discussed in Figure 4.4, it is observed that at lower Reynolds numbers, the contribution of non-dimensional numbers, which characterize the flow's turbulence level relative to viscous forces, becomes more increased.

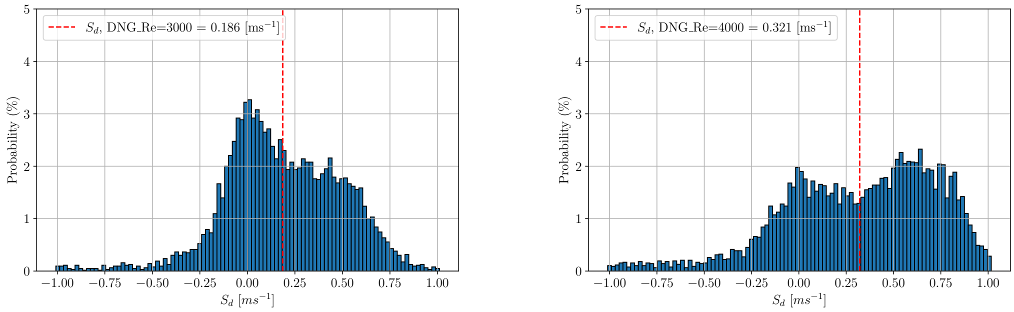

(a) Probability Distribution of local flame displacement speed (S_d) for DNG Flame at Re = 3000, $\phi = 1$.

(b) Probability Distribution of local flame speed (S_d) for DNG Flame at Re = 4000, $\phi = 1$.

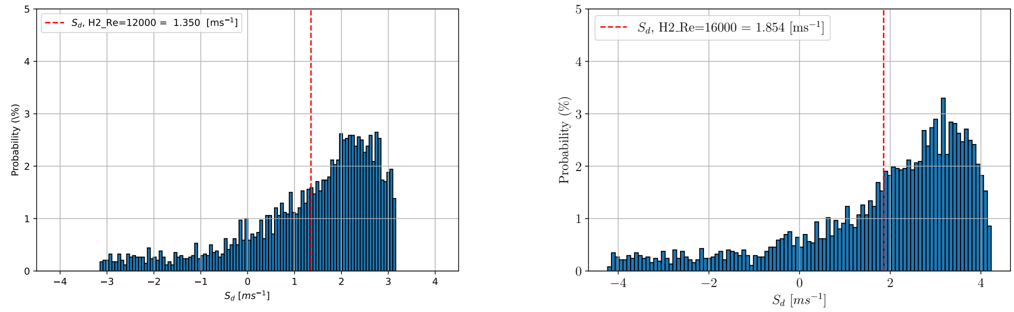

(c) Probability Distribution of local flame speed (S_d) for H2 Flame at Re = 12000, $\phi = 0.49$.

(d) Probability Distribution of local flame speed (S_d) for H2 Flame at Re = 16000, $\phi = 0.49$.

Figure 4.14: Sd distribution on x-axis considering positive and negative propagation on detected segments, represented by 4 different flames. Probability on y-axis represents the amount of values corresponding probability out of 100%.

Figure 4.14 captured the probability distribution of local displacement speed S_d for flames. Drawing on the methodologies from Section (3.5.1) on flame front propagation calculation, the local displacement speeds were computed to capture positive and negative propagation of flame front segments.

For DNG flames as seen in Figure 4.14a and Figure 4.14b, the averages of S_d found relatively lower than unstretched laminar flame speed (S_{L0} = 0.365 m/s), indicating a slower average propagation speed of the flame front. In contrast, H_2 as given by Figure 4.14c and Figure 4.14d show significantly higher average S_d, aligning with the expected increase in flame local displacement speed, due to the hydrogen's higher mass diffusivity. Furthermore, the average value of S_d not being zero for all flames, despite the flame fronts being stationary overall, can be attributed to local variations along the flame front. While the average position of the flame front may be stationary in the lab frame, individual segments can exhibit local movement. These local movements have been attributed to the reflection of local displacement speeds of different segments which detected along the flame front.

The range of the histograms represent the distribution of local flame speeds, with broader distributions indicating more variability of flame front displacement speed. The probability distributions for both DNG and H_2 flames exhibit a tendency for the flame fronts to propagate to the burnt region, as indicated by the most probable speeds being positive. This suggests that segments of the flame fronts are advancing in the positive direction of the flame propagation. However, the dynamic nature of the H_2 flames results in a wider spectrum of S_d values, with a significant occurrence of both larger negative and larger positive speeds. Comparatively, the DNG flames demonstrate a narrower range of S_d values, indicating less variability in the local flame front propagation speeds. It has been important to note that the PDF distribution of the numerical results for the turbulent displacement speed (S_d), as depicted in Figure 2.19, the PDF distribution of the numerical results for the turbulent displacement speed (S_d), shows an alignment with the findings of [14], where a similar variation in S_d is presented. While the distribution does extend into the negative range, indicating instances of negative propagation, these are less probable compared to the positive displacement speeds.

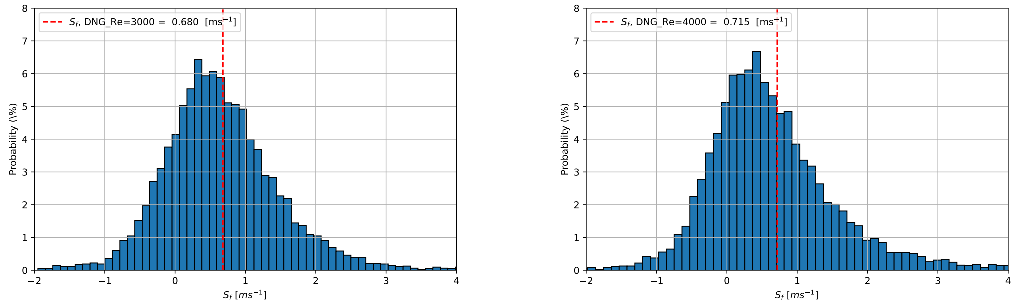

(a) Probability Distribution of local flame speed (S_f) for DNG Flame at Re = 3000, $\phi = 1$.

(b) Probability Distribution of local flame speed (S_f) for DNG Flame at Re = 4000, $\phi = 1$.

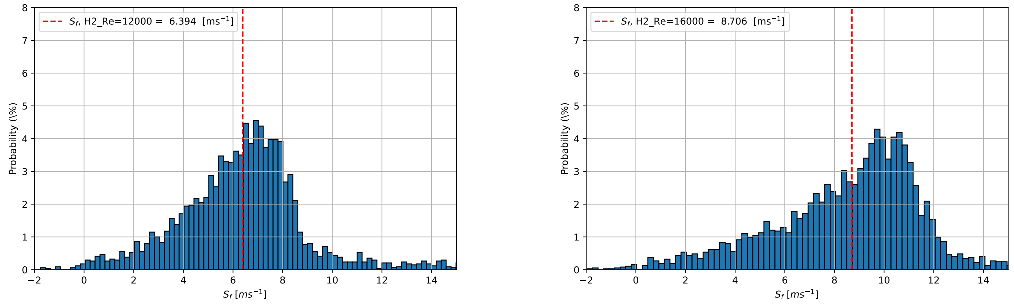

(c) Probability Distribution of local flame speed (S_f) for H2 Flame at Re = 12000, $\phi = 0.49$.

(d) Probability Distribution of local flame speed (S_f) for H2 Flame at Re = 16000, $\phi = 0.49$.

Figure 4.15: Sf distribution on x-axis considering flame balance on detected segments, represented by 4 different flames. Probability on y-axis represents the amount of values corresponding probability out of 100%.

Figure 4.15 illustrates the probability distributions of the local flame speed (S_f) for DNG and H_2 flames. These histograms are constructed by computing S_f based on the displacement speed and flow normal to the flame front segments as previously described in Equation 3.10 and 3.11 depending on the front propagation direction.

The average S_f values show differences between DNG and H_2 flames, as well as between different Re conditions and constant unstretched laminar flame speed. For the DNG flames as shown by Figure 4.15a and Figure 4.15b, the increase in Re for DNG flames appears to slightly elevate the average S_f, which remains both DNG flames exhibit slightly higher average S_f value than unstretched laminar flame speed. In contrast, the H_2 flames shown by Figure 4.15c and Figure 4.15d, exhibit average S_f values that are significantly higher, especially at $Re = 16000$, suggesting that average local flame speed is 10 times higher due to the effects of turbulence compared to the DNG flames particularly when comparing conditions close to flashback with those under stable combustion. This observation is in line with the findings of [14], which also suggest that local flame speed can be up to 20 times higher than the displacement speed.

The range of S_f values within the histograms reflects the diversity in local flame speed experienced by the flame front. DNG flames show a relatively narrow range, indicating a more uniform behavior in local flame speed. Meanwhile, H_2 flames display a broader range, highlighting the impact of turbulent flow conditions that contribute to a wider spectrum of local flame speeds. On the other hand, DNG flames show a near symmetrical distribution close to their average values. Furthermore, H_2 flames exhibit negative skewness, implying a greater occurrence of higher local flame speeds.

For all flames under investigation, the histograms predominantly feature positive local flame speeds, yet there is a notable occurrence of negative speeds as well. The predominance of positive speeds reflects segments of the flame front that are propagating rapidly in the flow's direction, signifying high S_d values. Instances where segments exhibit high local S_d but encounter low local V_n can lead to the calculated local flame speed being negative. This outcome, while mathematically possible within the computational framework, does not align with the physical expectation that flame front segments should not propagate in the reverse direction under normal combustion conditions. Therefore, these negative local flame speeds can be regarded as an unphysical artifact of the overlap between high displacement speeds and slower normal velocities in the computational model.

4.4.3. Local Flame Normal and Tangential Stretch

Local flame stretch in this study has been distinguished into two components: stretch in the normal and tangential directions to the flame front. The normal stretch, also referred to as stretch due to curvature, is computed considering both the local flame propagation speed and the local curvature of the flame front, in line with the framework established in Chapter (2.3). To compute the tangential stretch, a computational methodology involving interpolation and extrapolation techniques was employed, details of which are elaborated in Appendix A.6.

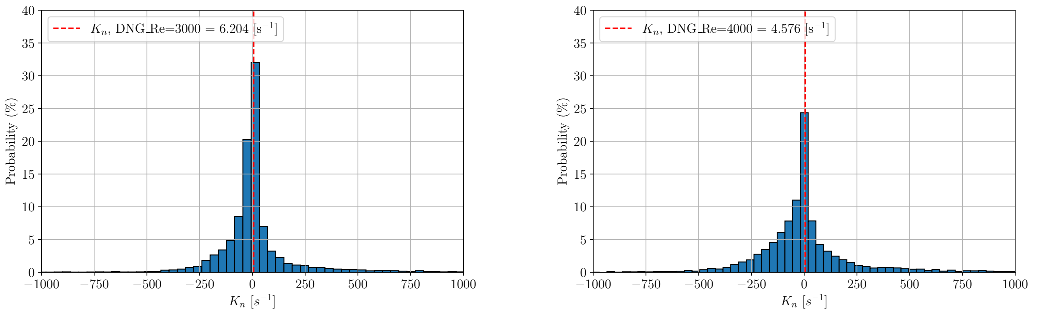

(a) Probability Distribution of normal stretch (K_n) for DNG Flame at Re = 3000, $\phi = 1$

(b) Probability Distribution of normal stretch (K_n) for DNG Flame at Re = 4000, $\phi = 1$

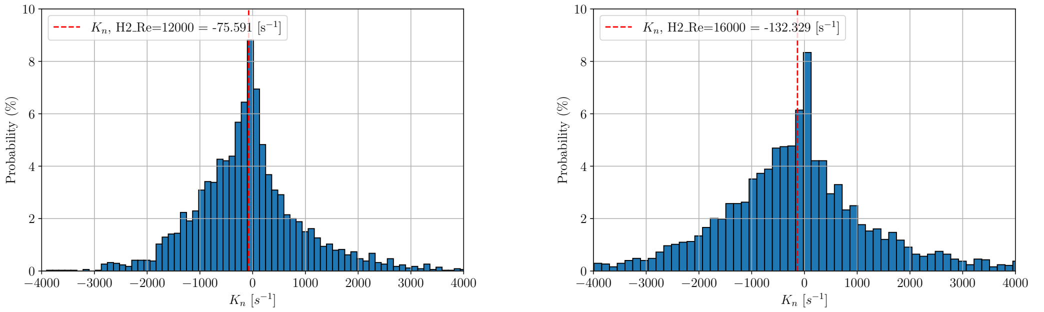

(c) Probability Distribution of normal stretch (K_n) for H2 Flame at Re = 12000, $\phi = 0.49$

(d) Probability Distribution of normal stretch (K_n) for H2 Flame at Re = 16000, $\phi = 0.49$

Figure 4.16: Kn distribution on x-axis considering flame stretch due to curvature on detected segments, represented by 4 different flames. Probability on y-axis represents the amount of values corresponding probability out of 100%.

Figure 4.16 presents the probability distribution of normal stretch (K_n) for DNG and H_2 flames. The vertical dotted red lines mark the average K_n values for each flame condition. Notably, the DNG flames Figure 4.16a and Figure 4.11b display average K_n values that are positive, suggesting a small tendency towards flame front expansion, suggesting a propensity for local flame expansion. This contrasts with H_2 flames as seen in Figure 4.16c and Figure 4.11d, where the average normal stretch values are negative, indicative of a prevailing local flame compression. The H_2 flames at higher Re exhibit even more substantial average K_n values, reflecting a significant influence of flame front curvature and propagation dynamics in turbulent conditions.

Due to the elevated local flame speeds and more intense turbulence experienced by H_2 flames, a wider range of normal stretch values is observed, with both higher maximum and more extreme minimum values. This trend is consistent for both DNG and H_2 flames; as the level of turbulence increases, the occurrence of both the highest and lowest normal stretch values observed. Interestingly, all histograms exhibit a symmetrical distribution around zero. This observation is consistent with the analysis of local curvature values for the flames as previously discussed in Figure 4.11, where peak probabilities in the histograms were also close around zero curvature values. The alignment of peak probabilities around zero for both stretch and curvature indicates that the flame fronts tend to maintain a neutral curvature, reflecting segments that are neither significantly stretched nor compressed.

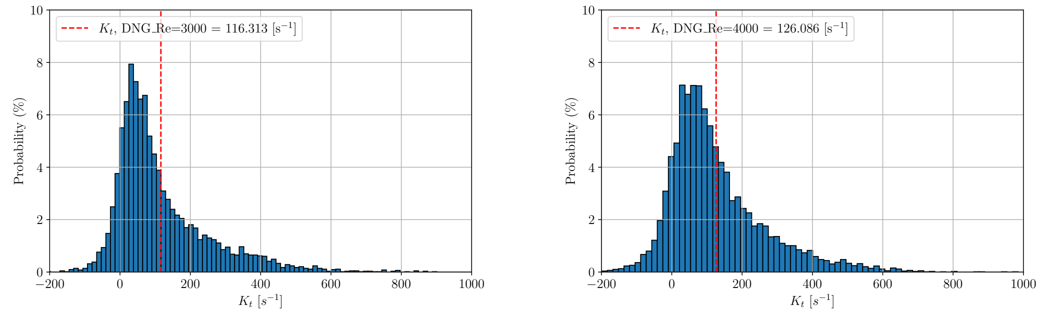

(a) Probability Distribution of tangential stretch (K_t) for DNG Flame at Re = 3000, $\phi = 1$.

(b) Probability Distribution of tangential stretch (K_t) for DNG Flame at Re = 4000, $\phi = 1$.

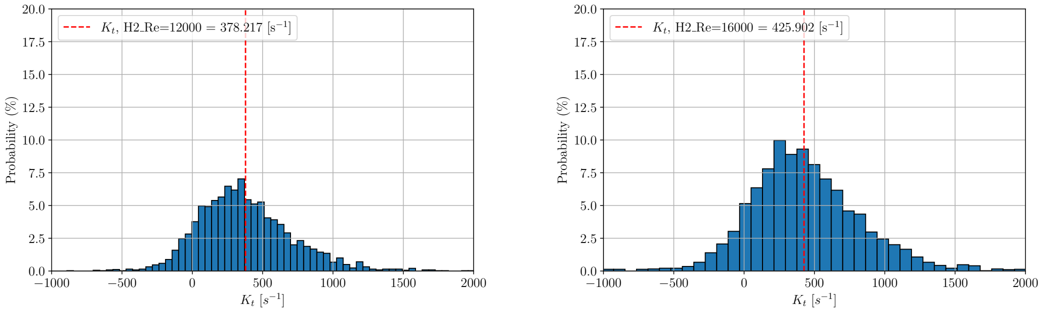

(c) Probability Distribution of tangential stretch (K_t) for H2 Flame at Re = 12000, $\phi = 0.49$.

(d) Probability Distribution of tangential stretch (K_t) for H2 Flame at Re = 16000, $\phi = 0.49$.

Figure 4.17: Kt distribution on x-axis considering flame stretch due to divergence of tangential velocities calculated from extrapolation on detected segments, represented by 4 different flames. Probability on y-axis represents the amount of values corresponding probability out of 100%.

Figure 4.17 shows the probability distributions of tangential stretch (K_t) for DNG and H_2 flames. The tangential stretch is a measure of the strain experienced by the flame front due to the divergence of tangential velocities along it. Unlike other flame properties, tangential stretch is affected solely by the flow dynamics around the flame front, independent of the combustion process.

The average K_t values provide insight into the general tendency of the flame front to either stretch or compress tangentially. For DNG flames as seen in Figure 4.17a and Figure 4.17b, the average K_t values are positive across different Reynolds numbers. Similarly, the H_2 flames exhibit in Figure 4.17c and Figure 4.17d with larger average K_t values, indicative of more significant tangential stretching influenced by the elevated turbulence levels. Increasing turbulence intensity also effects the range of the histograms, we observe that the H_2 flames possess a wider spread in K_t values compared to DNG flames, particularly at the higher Re. While the histograms for DNG flames demonstrate a positive skewness, indicating a higher frequency of lower tangential stretching, the H_2 flame histograms are relatively symmetrical.

All histograms reveal the presence of a tail of negative tangential stretches, signifying sections of the flame front where the tangential velocity has diminished, resulting in a negative stretch rate. This can be attributed to the intricacies of the computational framework employed. Specifically, the algorithm designed to identify the closest neighboring points may locate points that are still within the burnt region, thereby calculating a negative stretch rate.

4.4.4. Correlation Analysis of Physical Parameters

This correlation analysis aims to capture these physical relationships across four flames. In this section, the relationships between key flame parameters as discussed with histograms such as κ, S_f, S_d, V_n, V_t, K_n, and K_t in four different flames will be analyzed. It is aimed to understand how these parameters influence each other and what insights can be derived about DNG and H_2 flame's characteristics.

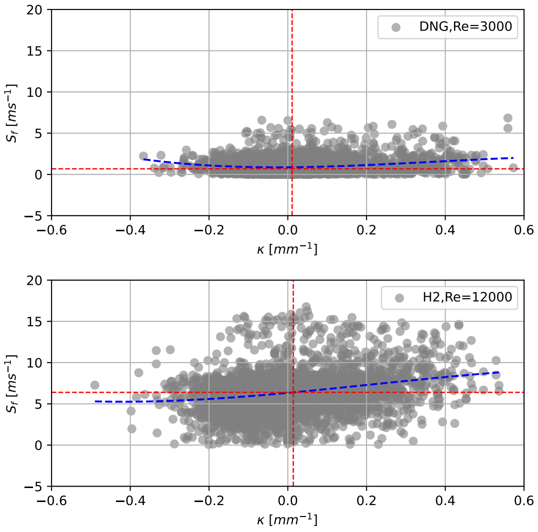

Figure 4.18: Correlation Analysis for $\kappa - S_f$ for DNG and H_2 flames. The blue dashed line indicates a second-order polynomial fit to the data. The vertical and horizontal red dashed lines represent the mean values from histograms.

Figure 4.18 illustrates the correlation between local curvature (κ) and local flame speed (S_f) in DNG and H_2 flames. For DNG flames, segments of the flame where the local curvature transitions from zero to -0.5 indicating that the front is curved towards the unburnt region where there is a slight increase in local flame speed. This trend is similarly observed for points corresponding to curvature transitions from zero to $+0.5$. As the curvature shifts to positive, signifying that the front is curved towards the burnt region, an increase in flame speed is also observed. This observation suggests that an increase in local curvature, whether towards the burnt or unburnt regions, is associated with an increase in local flame speed. One possible explanation for this phenomenon is that increasing local curvature is correlated with an increase in the local speed of the flow normal, which in turn contributes to the acceleration of the local flame speed. A notable observation in H_2 flames is the decrement in local flame speed as the local curvature transitions from zero to -0.5. Conversely, when the curvature transitions from zero to $+0.5$, an improvement in the local flame speed of H_2 flames is observed, a pattern that aligns with the behavior seen in DNG flames.

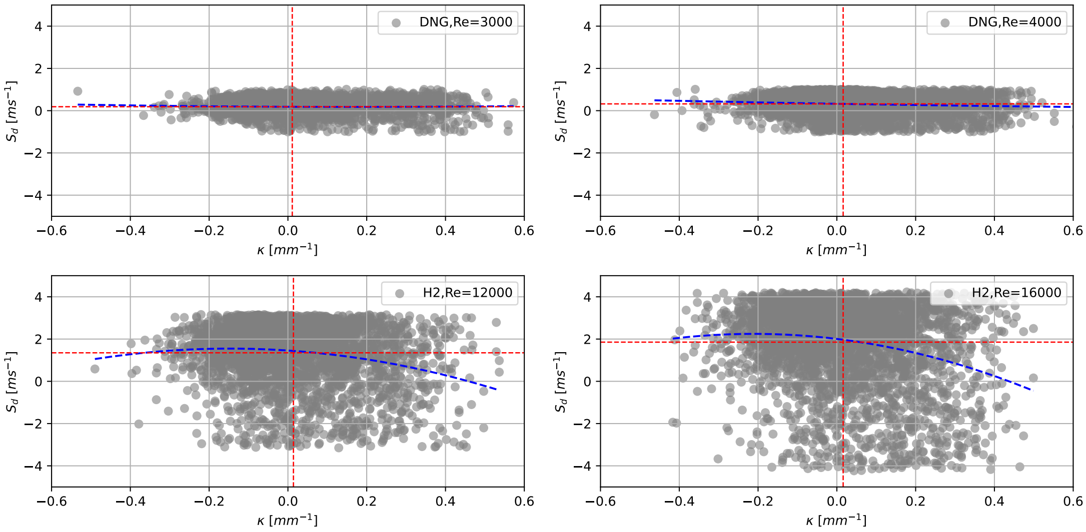

Figure 4.19: Correlation Analysis for $\kappa - S_d$ for DNG and H_2 flames. The blue dashed line indicates a second-order polynomial fit to the data. The vertical and horizontal red dashed lines represent the mean values from histograms.

Figure 4.19 shows correlation between local curvature (κ) and local flame displacement speed (S_d) in DNG and H_2 flames. For DNG flames, the correlation between curvature (κ) and local flame displacement speed (S_d) is characterized by a relatively stable trend. As shown in the analysis, the transition of curvature from negative to positive values does not significantly affect the local flame displacement speed. This observation suggests that, in DNG flames, the displacement speed is less sensitive to changes in the curvature of the flame front. In contrast, H_2 flames reveals that the displacement speed slightly decreases when the curvature transitions from zero to -0.5 or $+0.5$, with a more noticeable decrement observed for transitions from zero to $+0.5$. This trend indicates that S_d in hydrogen flames tends to decrease, especially when the flame front curvature becomes extremely positive. Such behavior could be indicative of the tendency for segments with extreme positive curvature to propagate towards the unburnt mixture.

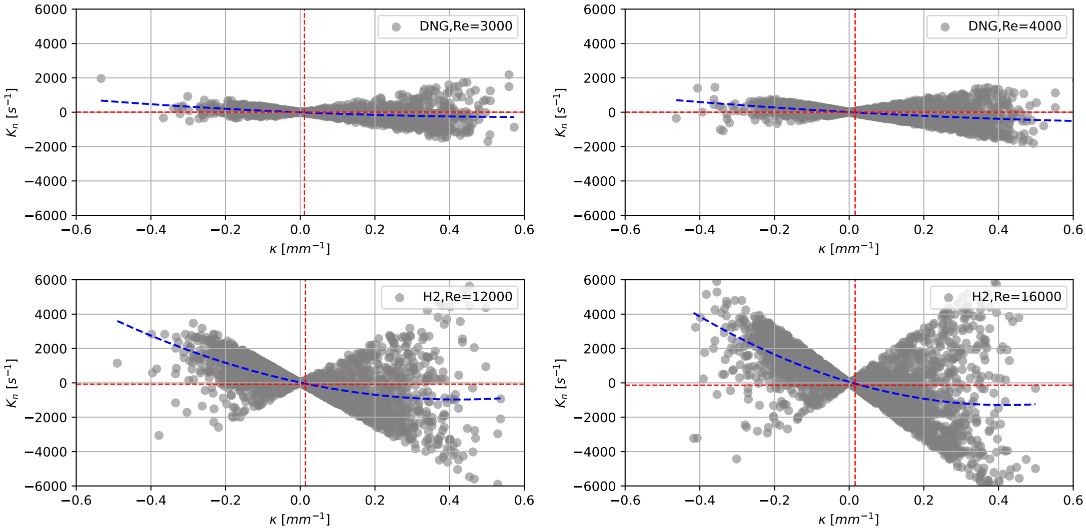

Figure 4.20: Correlation Analysis for $\kappa - K_n$ for DNG and H_2 flames. The blue dashed line indicates a second-order polynomial fit to the data. The vertical and horizontal red dashed lines represent the mean values from histograms.

Figure 4.20 presents the correlation between local curvature (κ) and local normal flame stretch (K_n) in both DNG and H_2 flames. Consistent with theoretical expectations, the observed correlation for DNG flames aligns well with anticipated behavior. Specifically, areas of the flame front exhibiting positive curvature, which are concave towards the burnt gases, are generally associated with negative normal stretch, indicative of localized flame compression. Conversely, areas with negative curvature, convex towards the unburnt gases, tend to show positive normal stretch, reflecting localized flame elongation. This pattern underscores the nuanced relationship between the physical shape of the flame front and its stretching characteristics. For H_2 flames, while the relationship between curvature (κ) and normal stretch (K_n) follows a similar trend to that of DNG flames, it is characterized by more extreme stretch values. This observation suggests that hydrogen flames, particularly at higher operating conditions, are subject to more increased stretching effects. The extreme stretch values in H_2 flames could be indicative of higher existence of displacement speed occurs in H_2 flame fronts.

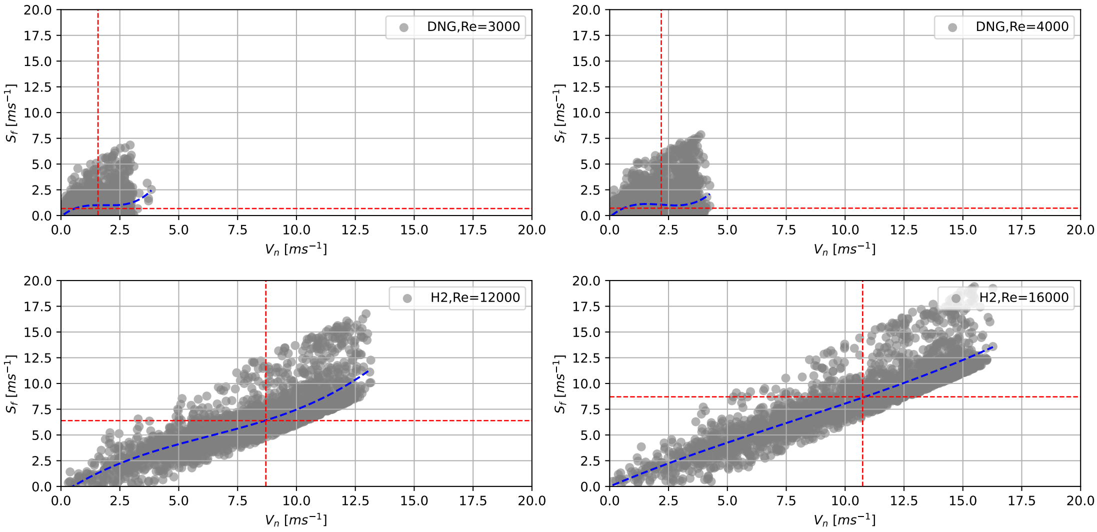

Figure 4.21: Correlation Analysis for $V_n - S_f$ for DNG and H_2 flames. The blue dashed line indicates a second-order polynomial fit to the data. The vertical and horizontal red dashed lines represent the mean values from histograms.

Figure 4.21 shows correlation between dynamic parameters called local flame speed (S_f) and local flow normal speed (V_n) in both DNG and H_2 flames. In DNG flames, a direct proportional relationship is observed between the flame speed (S_f) and the normal velocity (V_n). This correlation reveals that as the normal velocity increases, the flame speed typically rises in tandem. For H_2 flames, operating at higher Reynolds numbers than DNG flames, increased normal velocity component is evident. As the flame speed increases, a concurrent increase in the local flow velocity is observed. For H_2 flame particularly at higher Reynolds numbers, the relationship between normal velocity (V_n) and flame speed (S_f) tends to be more linear. This linear trend contrasts with the nonlinear behavior typically observed in other flame conditions. The relative speed or displacement speed (S_d), representing the difference between these two velocity components, aligns closely with the local flow velocity in these cases.

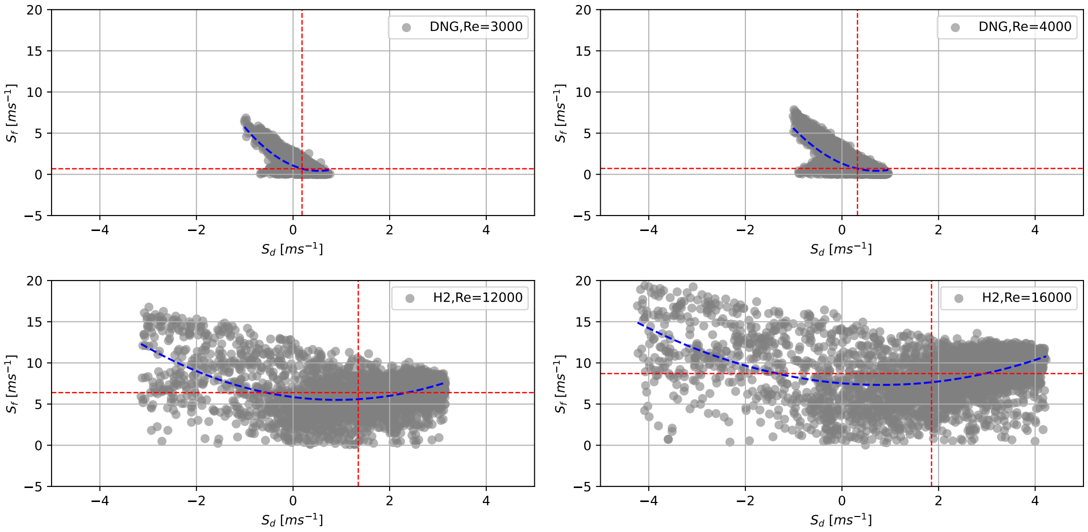

Figure 4.22: Correlation Analysis for $S_d - S_f$ for DNG and H_2 flames. The blue dashed line indicates a second-order polynomial fit to the data. The vertical and horizontal red dashed lines represent the mean values from histograms.

Figure 4.22 displays corrlation between local flame displacement (S_d) and local flame speed (S_f). For DNG flames, a notable correlation is observed; an increase in the negative displacement speed is accompanied by an increment in the flame speed. This non-linear relationship is consistent with the understanding that negative displacement indicates flame segments that propagate against the flow more faster, thereby enhancing flame speed. In H_2 flames, the impact of negative displacement speed on local flame speed is observed to be similar to that in DNG flames. However, a more pronounced effect is noted in positively displaced segments. These segments, when propagating positively, exhibit a significant increase in local flame speed. This could be attributed to the strong contribution of the local flow normal in positively displaced segments, further accelerating the flame speed. This observation highlights the dynamic response of hydrogen flames to displacement direction, emphasizing the role of local flow characteristics in influencing flame behavior, especially at higher Reynolds numbers.

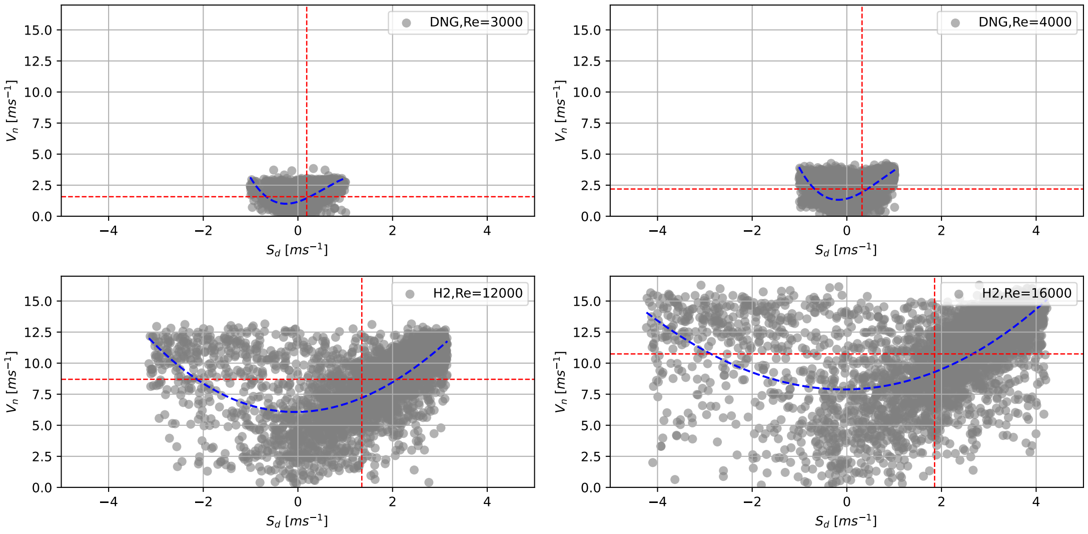

Figure 4.23: Correlation Analysis for $S_d - V_n$ for DNG and H_2 flames. The blue dashed line indicates a second-order polynomial fit to the data. The vertical and horizontal red dashed lines represent the mean values from histograms.

Figure 4.23 illustrates the correlation between displacement speed (S_d) and normal velocity (V_n) for DNG and H_2 flames. The data points suggest a relationship that appears exponential, particularly noticeable in the negative displacement speed domain where an increase in V_n is observed. In regions where S_d is minimal, V_n values are close to those of the stationary segments, indicating a consistent flow behavior across the flame front. H_2 flames, as shown in Figure 4.23 exhibit a wider spread in the data. Despite the dispersion, the fitted curve suggests a pattern similar to that of DNG flames. Notably, the lowest V_n is observed when the flame segments are stationary, while segments with positive displacement show a distinct increase in V_n, reflective of the strong influence of the local flow. This behavior is evident in the Re = 16000 case, where data points are more densely clustered at higher positive displacement speeds, suggesting an active interaction between the flame front and the flow field.

The graphs also reveal that for both DNG and H_2 flames, the regions of highest V_n do not necessarily coincide with the highest S_d, challenging the assumption that flame speed and flow velocity are directly proportional. This discrepancy could be explored further to understand the limits of flame-front stability and the mechanisms of flame holding in turbulent flows.

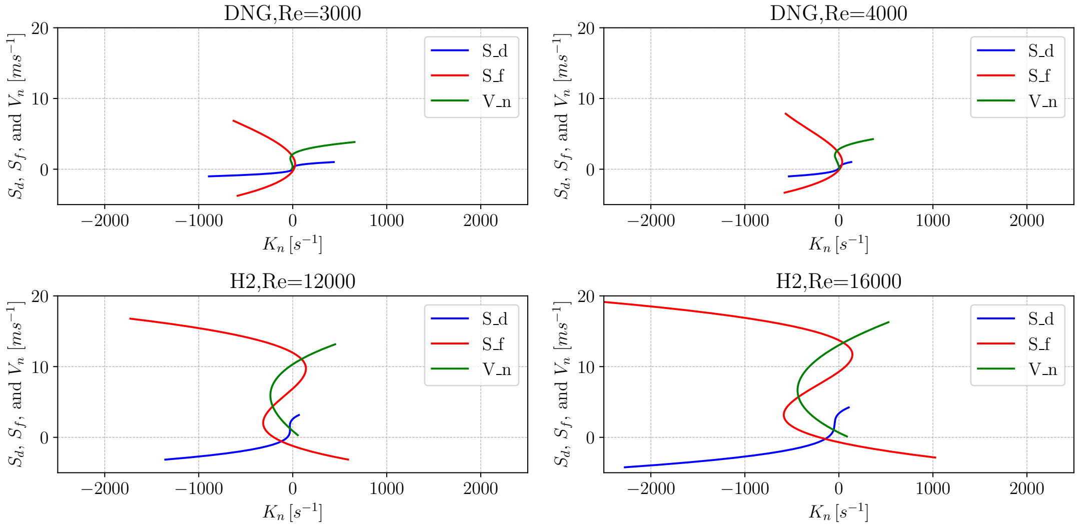

Figure 4.24: Correlation Analysis for local dynamic parameters - K_n for DNG and H_2 flames. The blue dashed line indicates a second-order polynomial fit to the data. The vertical and horizontal red dashed lines represent the mean values from histograms.

Figure 4.24 pertains to the DNG and H_2 flames in order to capture local flame dynamic parameters and normal stretch due to normal stretch (K_n). In assessing the correlation of normal stretch with dynamic parameters, a negative displacement speed (S_d) is observed to result in negative stretch for both flames. It is noteworthy that the DNG flame at $Re = 3000$ exhibits a higher displacement speed, which in turn induces a more pronounced negative stretch on the flame front when flame is close to flashback. When the displacement speed approaches zero, it implies an absence of normal stretch concerning frontal propagation. A positive flame displacement leads to positive stretch, with the DNG flame at $Re = 3000$ exhibiting a greater magnitude of positive stretch. For H2 flames, the increase in Reynolds number from 12000 to 16000 results in a steeper S_d values reflect pronounced stretch values, suggesting that H2 flames are more sensitive to changes in turbulence as reflected by Reynolds number.

For DNG flames, as the Reynolds number increases from 3000 to 4000, the S_f curves become broader and shift to the right, indicating that the local flame speed is increasing with higher turbulence. The peak of the curve flattens, which suggests a more uniform flame speed across different values of normal stretch. For H2 flames, the increase in Reynolds number from 12000 to 16000 results in a steeper S_f curve with a pronounced shift to the right, implying a significant increase in the local flame speed at higher normal stretch values, indicating that H2 flames are more sensitive to changes in turbulence as indicated by the Reynolds number. It's worth noting that negative values of S_f observed in the analysis may be due to artifacts where the segments display higher positive displacement speed and encounter with relatively lower normal flow velocity.

For V_n, the DNG flames exhibit a similar curve with an increase in Reynolds number. This suggests that the flow normal velocity on the flame front segments becomes less sensitive to normal stretch with an increase in turbulence. In contrast, the H2 flames display a steeper V_n curve with increasing Reynolds numbers, especially skewing towards the positive K_n values, which suggests an increased sensitivity of the flow normal velocity to positive normal stretch under more turbulent conditions. These observations highlight that both S_f and V_n are affected by changes in the Reynolds number, signifying the impact of turbulence on flame dynamics, with

H2 flames showing more significant responses than DNG flames.

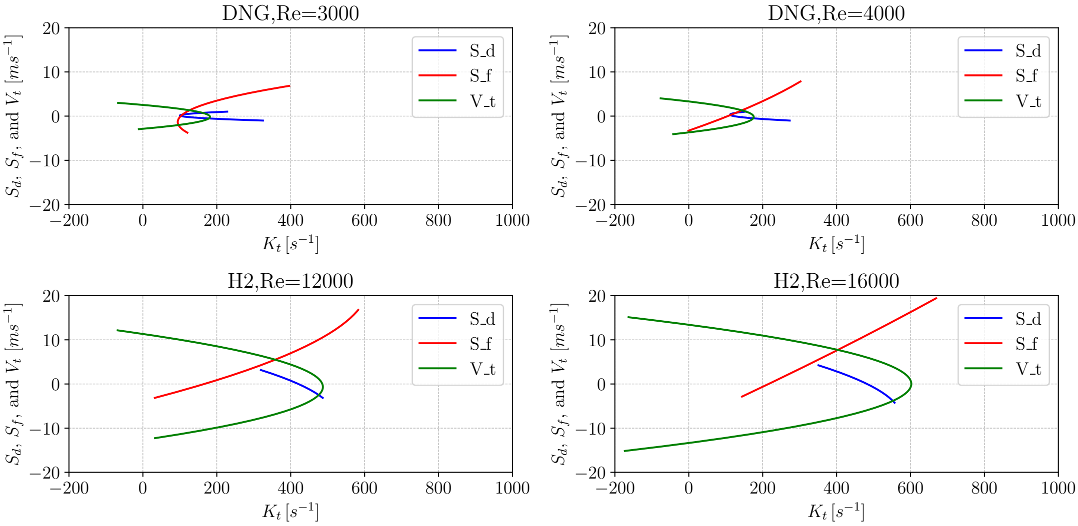

(a) Correlation Analysis for local dynamic parameters - K_t for DNG and H_2 flames. The blue dashed line indicates a second-order polynomial fit to the data. The vertical and horizontal red dashed lines represent the mean values from histograms.

In the analysis of tangential stretch correlation (K_t), the fitted curves can be seen in Figure 4.25a. For DNG flames, displacement speed shows minimal influence on tangential stretch, regardless of flame propagation direction. An exponential relationship is observed between tangential velocity (V_t) and K_t, with peak stretch occurring when V_t approaches zero. It's important to note that K_t is not directly calculated from V_t but is determined through advanced extrapolation analysis of tangential divergence. Flame speed (S_f) has a significant impact on tangential stretch, particularly at $Re = 3000$ for DNG flames. In contrast, for hydrogen flames, the transition from negative to positive displacement speed results in reduced tangential stretch, likely due to the increasing dominance of normal stretch. The relationship between global tangential velocity (V_t) and K_t follows an exponential trend in both DNG and hydrogen flames, with higher *Re* values leading to more pronounced tangential stretches.

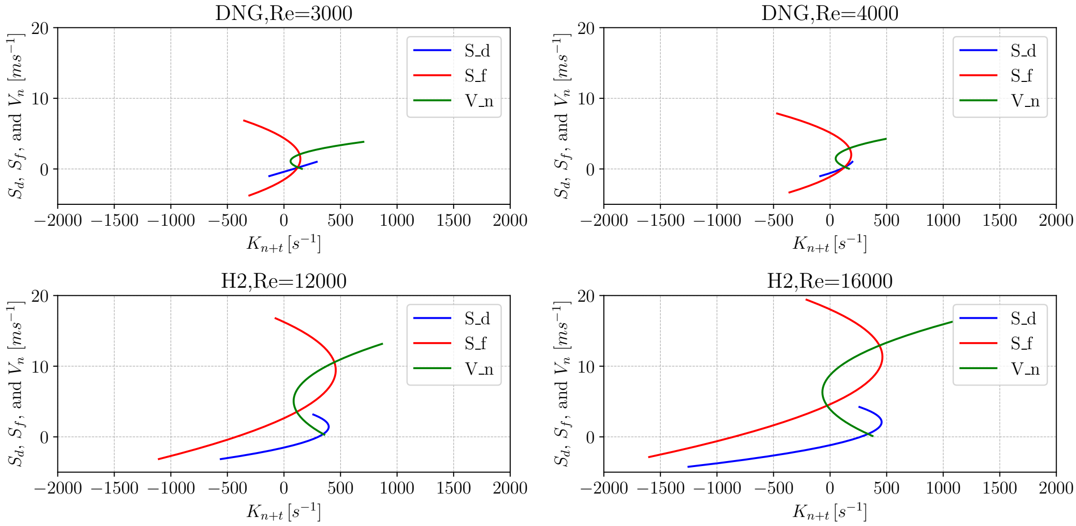

(a) Correlation Analysis for local dynamic parameters - K_{tot} for DNG and H_2 flames. The blue dashed line indicates a second-order polynomial fit to the data. The vertical and horizontal red dashed lines represent the mean values from histograms.

For DNG flames, the displacement speed (S_d) appears to have limited influence on total stretch denoted by K_{tot}, curves of the data fit display similar behavior as it was observed in normal stretch. Whether the flame propagates in positive or negative directions, the total stretch remains more or less consistent. The relationship between V_n and the total stretch seems to adhere to an exponential correlation, with significant stretches observed when V_n increases. As for the flame speed (S_f), an increase once again induces a heightened total stretch, especially pronounced for DNG with *Re* = 3000 higher than *Re* = 4000. In the case of hydrogen flames, the transition of displacement speed from negative to positive leads to a discernible increase in total stretch, similar to what was seen in displacement effects on normal stretch. The global normal velocity component V_n showcases an exponential relationship with the total stretch, analogous to its correlation with the tangential stretch. The influence of flame speed on the total stretch is more dominant for the H2 flame at *Re* = 16000, showing a near-linear relationship and overshadowing the effects observed in the H2 *Re* = 12000 scenario.

5

Conclusion

Quantitative analysis of flame kinematics has been captured in this study, comparing two distinct fuels: Dutch Natural Gas (DNG) and hydrogen (H_2). This analysis was conducted using Particle Image Velocimetry (PIV) measurements and flame front segmentation. A series of experiments were performed under varying conditions, including stable flames and flames close to flashback, while maintaining a constant unstretched laminar flame speed ($S_{L0} = 0.365\,\mathrm{m/s}$). Our findings, derived from both high-speed and low-speed recordings, reveal critical insights into the cold flow characteristics, turbulent flame behaviors, and the quantitative aspects of these fuels' flame dynamics and kinematics.

- Cold flow measurements: Experiments of flows with four different Reynolds number were conducted. The statistics of umean/ub, $u'u'/ub^2$, and $v'v'/ub^2$ were compared with LDA measurements from [60] to validate experimental setup.
- Turbulent flame characteristics: Low-speed recordings were performed on the flames for both DNG and H2 cases. This involved determining the average flame front position using Mie-scattering intensity, constructing Borghi diagrams, and comparing the flame's flow field in terms of absolute velocity, divergence field of the flames and their turbulent kinetic energy were analyzed.
- Quantitative analysis: High-speed recording methods were employed to capture precise dynamics between consecutive images. An in-house algorithm was developed for segmenting the flame front, providing insights into the flame-flow dynamics and kinematics.
  - Histograms: After completing PIV measurements and segmentation, histograms were plotted to display curvature, flame dynamics, and kinematic parameters. These histograms helped in determining average values, maximum and minimum ranges, and skewness values.
  - Correlation Analysis: Correlation analyses were conducted based on the histogram values of physical parameters, aiming to understand the interconnections between these parameters and their influence on flame sensitivity.

5.1. Conclusions on Cold flow statistics

There is an expected deviation in the centerline of the flow, where PIV results on centerline decreases with increasing Reynolds number. The magnitude of the differences for these peaks in terms of fluctuations in the axial and radial direction were small enough, indicating a good agreement in between PIV and LDA.

5.2. Conclusions on Turbulent Flame Characteristics

- Average Flame Front Location: H2 flames showed heightened intensity (count [-]) peaks in contour distribution, indicating regions of intense scattering and an increase in flame front area with rising Reynolds number. However, DNG flames tips are more close to the burner rim in the sense that their lower Reynolds number.

- Turbulent Flame Regimes: On the Borghi diagram, H2 and DNG flames occupy distinct regimes – corrugated flamelets for H2 and wrinkled flamelets for DNG. This difference is, the higher turbulence intensity in H2 flames leads to a corrugated, more surface-area-rich flame front. In DNG flames more moderately wrinkled front and larger cusps formation has been observed.

- Averaged Velocity Fields: H2 flames demonstrate higher flow velocities due to their higher operating Reynolds number. However, the normalized average velocity field reveals that the lower Reynolds number of DNG flames results in a higher normalized distribution near the flame front vicinity which yields on decreasing Reynolds numbers in DNG flames led to higher velocities and increased flow disturbances.

- Divergence Fields: The divergence field, indicative of density variations or velocity jump across a control surface. H2 flames with higher Reynolds numbers showed increased divergence due to higher velocity gradients at the flame front. However, a notable aspect emerges when normalizing these divergence values. Post-normalization, both H2 and DNG flames with close to flashback exhibited higher divergence comparing with stable conditions. This finding is pivotal in understanding the instability mechanisms in these flames, suggesting that lower Re number might be more prone to instability due to sharper velocity and normalized density gradients at the flame front.

- Turbulent Kinetic Energy: The Reynolds number significantly influences the normalized TKE as expected due to enhanced turbulence, particularly around the tip of the DNG flames, where higher Reynolds numbers lead to an increase in normalized TKE due to intensified turbulence. In contrast, even at lower Reynolds numbers, DNG flames show more normalized TKE than H_2 flames. This can be linked to the adjustments in the equivalence ratio needed to maintain constant laminar flame speeds, which affect the stoichiometry and thus the combustion dynamics.

5.3. Quantitative Analysis on Flame Kinematics

5.3.1. Flame slope change and local curvature

- Flame Front Curvature and Stability: Across all flames, the predominant near-zero curvature values indicate the substantial presence of largely uncurved segments. H2 flames can be characterized by smaller and more wrinkle cusps formation, leading to a higher degree of variability in slope change, indicative of higher variablity of local curvature. DNG flames exhibit maximum slope change mainly in regions with larger cusps. The side of the flame display more consistent segment formation and uniform curvature rather than tip of the flame.

5.3.2. Local Dynamics of Flames

- Dimensionless flow normal velocity V_n: An increase in the average flow normal to the flame segments (V_n) with rising Reynolds numbers is expected. While DNG flames show symmetric distributions around their averages, hydrogen flames exhibit a negative skewness distribution around higher values. Across all cases, the average V_n is slower than the bulk flow speed.

- Flow tangential on the segments V_t: All flames demonstrate a balanced tangential velocity profile, reflecting symmetrical swirling or rotational behavior within their turbulent flow structures. This symmetry is exemplified by nearly zero averages and flat skewness centered around 0 m/s for all flame types under study.
- Local Flame Displacement Speed S_d: The average displacement speeds findings for both DNG flames are found to be lower than their respective unstretched laminar flame speeds. A notable increase in average S_d is observed for DNG Re = 4000 compared to DNG Re = 3000, indicating faster or more extensive downstream propagation and hence, more frequent positive displacement and less frequent zero displacement. For hydrogen flames, there is an increase in average S_d along with the Reynolds number reflects higher magnitudes of displacement speed compared to the DNG flames.
- Local Flame Speed S_f: For the DNG flames, increasing Reynolds number also increses the average local flame speed. These speed changes in four flames correlate with the variations observed in the local displacement speed. While DNG flames show lower average speeds relative to hydrogen flames, the local flame speeds are directly influenced by the combined effects of displacement speed and flow normal on the segments. Due to the consideration of the local flame speed calculation in Equation 3.11, some of the detected segments exhibit higher local displacement speeds and relatively low flow normal velocities. Notably, this method occasionally resulted in the calculation of negative local flame speeds, which appears to be an artifact rather than an actual physical characteristic of the flames.

5.3.3. Local Kinematics of Flames

- Normal stretch: All flames exhibit symmetrical distribution around zero stretch. Particularly, the Hydrogen flames showed a broader local K_n variability on flame front. Interestingly, Hydrogen flames display more prone to local flame compression.
- Tangential Stretch: In examining tangential stretch (K_t), it was found to be a flow property, primarily influenced by the surrounding flow dynamics on flame front vicinity. Across the flames, increasing Reynolds number hinted at enhanced flow velocities in tangential direction, also increases local flame stretch in tangential direction.

5.4. Correlation Analysis

- $\kappa - S_f$: DNG flames depict a decline in flame speed as the flame front transitions from convex to linear. H_2 flames, exhibit a reverse behavior, showcasing an escalating flame speed across different curvatures. These variations suggest that while DNG flames possess a complex interaction between flame speed and curvature, H_2 flames with higher local flame speeds lean towards to conditions with concave flame fronts.
- $\kappa - S_d$: The displacement speed in DNG flames generally suggests a positive propagation with concave movement. Specifically, DNG flames exhibit more consistency in displacement speed across changing local curvatures. H2 flames, on the other hand, exhibit a notable trend: linear or slightly convex segments of the flame front results faster propagation.
- $\kappa - K_n$: Curve fit for four flames remains consistent with theoretical predictions. Concave segments on the flame front tend to experience compression, whereas convex segments have showing a tendency towards elongation. DNG Re = 4000 flames display a more

linear relationship in stretch-curvature, especially for convex segments. Contrarily, H2 flames at H2 Re = 12000 and H2 Re = 16000 are more stretched across similar curvatures, influenced by their higher displacement speeds.

- $S_f - V_n$: DNG flames delineate in specific regions, as S_f approaches zero or becomes negative, there's a coinciding surge in V_n values. In the context of H2 flames, due to the elevated Reynolds numbers when compared to DNG flames, they operate in regimes showcasing pronounced normal velocity components. Moreover, where flame speed escalates, an associated increase in local flow speed is discerned.
- $S_f - S_d$: Within DNG flames, both negative and positive displacement variations emerge at local negative flame speeds where it was noted that an unphysical artifact. For all flames, a non-linear relationship is observed that negative displacement indicates flame segments that propagate in negative direction, thereby enhancing flame speed.
- $S_d - V_n$: The curve fit suggests relationship that appears exponential with an origin close to zero displacement speed. It has been evident that segments with negatively displaced creates an increase in V_n. Where more detected data points clustered at higher positive displacement speeds, suggesting a direct proportionality in between displacement speed and flow normal velocity.
- $K_n - Dynamics$: Comparing DNG to H2 flames under varying Reynolds numbers unveils differential behaviors. The DNG flame at Re = 3000 showcases heightened sensitivity to dynamic parameters like V_n and S_d, resulting in more noticeable stretches. On the H2 flames at elevated Reynolds numbers represent influences, especially regarding S_d's impact on stretch. Increasing the Reynolds number makes more sensitive response for H2 flames. Additionally, H2 flames consistently respond to dynamic evaluations, lacking the anomalies evident in DNG flames for negative flame speeds.
- $K_t - Dynamics$: Both DNG and H2 flames demonstrates an exponential relationship between global V_t and K_t. Within DNG flames, the variations in displacement speed do not markedly increase tangential stretch. However, for H2 flames, a transition from negative to positive displacement speed is accompanied by a decrease in tangential stretch.
- $K_{n+t} - Dynamics$: DNG and hydrogen flames both exhibit correlations between V_n, S_d, and S_f when analyzing the interplay of total stretch where normal stretch becomes more dominant mechanism.

6

Future Recommendations

- **Streamline Analysis and Navier-Stokes Equations:** To gain a deeper understanding of the pressure and stability in flame dynamics, it is recommended for future research to track streamlines within the combustion flow field. Investigating these streamlines through the lens of the Navier-Stokes equations will be key to uncovering significant insights into how pressure fluctuations influence the stability of flames.
- **Three-Dimensional Flame Topology Studies:** For a more detailed understanding of flame topology, future research should delve into tomographic studies. Such an approach would be invaluable in unraveling the three-dimensional structure of flame topology. Moreover, developing a methodology that can accurately capture the dynamic behavior of the flame front in three dimensions would enhance our understanding of flame dynamics and stability.
- **Impact of Different Fuel Mixtures:** Investigating the flame dynamics with varying fuel compositions of gradually increasing H2 content into DNG mixture, with additionally investigating pure fuels with different equivalence ratios might capture different flame characteristics.
- **Flame Front Instabilities:** By utilizing advanced optical techniques like Planar Laser-Induced Fluorescence (PLIF), researchers can gain detailed insights into the spatial and temporal evolution of flame front dynamics in terms of temperature and species distribution.
- **Real Life Gas Turbine Applications:** Specifically, these techniques can be utilized to analyze flame behavior in gas turbines, ensuring that the combustion process operates within optimal parameters. This not only enhances performance but also helps in minimizing emissions and improving fuel efficiency. Understanding the detailed flame dynamics, including flow interactions is essential in predicting and preventing issues like flame instabilities, flashback and blow-off limits, which are critical for the safe and efficient operation of gas turbines.

References

[1] URL: `https://ifrf.net/ifrf-blog/hydrogen-and-combustion-big-challenge-big-chance`.

[2] URL: `https://slideplayer.com/slide/3920812/`.

[3] URL: `https://www.bronkhorst.com/getmedia/98668a82-8d1c-4b7f-af8e-995be25641b3/EL-FLOW-Select_EN.pdf`.

[4] R. J. Adrian. “Particle-imaging techniques for experimental fluid mechanics”. In: *Annual Review of Fluid Mechanics* 23 (1 2011), pp. 261–304.

[5] Georg Baumgartner, Lorenz R Boeck, and Thomas Sattelmayer. “Experimental investigation of the transition mechanism from stable flame to flashback in a generic premixed combustion system with high-speed micro-particle image velocimetry and Micro-PLIF combined with chemiluminescence imaging”. In: *Journal of Engineering for Gas Turbines and Power* 138.2 (2016).

[6] M Bellenoue et al. “Direct measurement of laminar flame quenching distance in a closed vessel”. In: *Experimental thermal and fluid science* 27.3 (2003), pp. 323–331.

[7] Ernesto Bribiesca. “A geometric structure for two-dimensional shapes and three-dimensional surfaces”. In: *Pattern recognition* 25.5 (1992), pp. 483–496.

[8] Ernesto Bribiesca. “A new chain code”. In: *Pattern recognition* 32.2 (1999), pp. 235–251.

[9] Hugo J Burbano, Jhon Pareja, and Andrés A Amell. “Laminar burning velocities and flame stability analysis of syngas mixtures at sub-atmospheric pressures”. In: *International Journal of Hydrogen Energy* 36.4 (2011), pp. 3243–3252.

[10] Germain Chartier. *Introduction to optics*. Springer, 2005.

[11] Chun W Choi and Ishwar K Puri. “Contribution of curvature to flame-stretch effects on premixed flames”. In: *Combustion and flame* 126.3 (2001), pp. 1640–1654.

[12] P Clavin and G Joulin. “Premixed flames in large scale and high intensity turbulent flow”. In: *Journal de Physique Lettres* 44.1 (1983), pp. 1–12.

[13] Nur Çobanoğlu and Ziya Haktan Karadeniz. “Effect of nanofluid thermophysical properties on the performance prediction of single-phase natural circulation loops”. In: *Energies* 13.10 (2020), p. 2523.

[14] Marcus S Day et al. *Displacement speeds in turbulent premixed flame simulations*. Tech. rep. Lawrence Berkeley National Lab.(LBNL), Berkeley, CA (United States), 2007.

[15] Jeroen Dierickx et al. “Evaluation and extension of ignition delay correlations for dual-fuel operation with hydrogen or methanol in a medium speed single cylinder engine”. In: *Fuel* 345 (2023), p. 128254.

[16] RM Drake and JE Gordon. “Mie scattering”. In: *American Journal of Physics* 53.10 (1985), pp. 955–962.

[17] Sven Eckart et al. “Experimental study and proposed power correlation for laminar burning velocity of hydrogen-diluted methane with respect to pressure and temperature variation”. In: *International Journal of Hydrogen Energy* 47.9 (2022), pp. 6334–6348.

[18] Christian Eichler and Thomas Sattelmayer. “Premixed flame flashback in wall boundary layers studied by long-distance micro-PIV”. In: *Experiments in fluids* 52.2 (2012), pp. 347–360.

[19] Williams F.A. *Combustion Theory: the fundamental theory of chemically reacting flow systems*. Second. Combustion Science and Engineering Series. Menlo Park, California: The Benjamin/Cummings Publishing Company, 1985.

[20] Filippo Faldella. “Experimental investigation of Boundary Layer Flashback in high H2 concentration turbulent premixed jet flames”. In: (2020).

[21] Luming Fan et al. “Simultaneous stereo-PIV and OH× CH2O PLIF measurements in turbulent ultra lean CH4/H2 swirling wall-impinging flames”. In: *Proceedings of the Combustion Institute* 39.2 (2023), pp. 2179–2188.

[22] Burton Fine. *Further experiments on the stability of laminar and turbulent hydrogen-air flames at reduced pressures*. Tech. rep. 1957.

[23] Pierre Friedlingstein et al. “Global carbon budget 2019”. In: *Earth System Science Data* 11.4 (2019), pp. 1783–1838.

[24] Markstein G.H. *Nonsteady flame propagation*. Pergamon Press, 1964.

[25] Gerda Gahleitner. “Hydrogen from renewable electricity: An international review of power-to-gas pilot plants for stationary applications”. In: *international Journal of hydrogen energy* 38.5 (2013), pp. 2039–2061.

[26] Amiya Ghosh and S K Saha. *Measurement Techniques in Mechanical Engineering*. CRC Press, 2015.

[27] E Giacomazzi, FR Picchia, and N Arcidiacono. “On the distribution of Lewis and Schmidt numbers in turbulent flames”. In: *30th Italian Meeting on Combustion, Ischia, Italy*. 2007.

[28] Kristian Jack Grayson. “Laser characteristics and configurations for high quality PIV measurements”. PhD thesis. The University of Melbourne, 2018.

[29] Zuohua Huang et al. “Measurements of laminar burning velocities for natural gas–hydrogen–air mixtures”. In: *Combustion and flame* 146.1-2 (2006), pp. 302–311.

[30] B Jeanne et al. “Bunsen flame analysis using simultaneous tomographic images and PIV in the fresh and burnt gases”. In: *9th International Symposium on Flow Visualisation, Heriot-Watt University, Edimburgh, Editor GM Carlomagno and I. Grant*. 2000, pp. 376–1.

[31] Alireza Kalantari and Vincent McDonell. “Boundary layer flashback of non-swirling premixed flames: Mechanisms, fundamental research, and recent advances”. In: *Progress in Energy and Combustion Science* 61 (2017), pp. 249–292.

[32] Richard D Keane and Ronald J Adrian. “Theory of cross-correlation analysis of PIV images”. In: *Applied scientific research* 49.3 (1992), pp. 191–215.

[33] JO Keller et al. “Mechanism of instabilities in turbulent combustion leading to flashback”. In: *Aiaa Journal* 20.2 (1982), pp. 254–262.

[34] Tim Lambers. “Boundary Layer Flashback of Turbulent Premixed Hydrogen/DNG/Air Flames produced by a Bunsen Burner”. In: (2021).

[35] Chung K Law. *Combustion physics*. Cambridge university press, 2010.

[36] Bertrand Lecordier et al. “CCD recording method for cross-correlation PIV development in unstationary high speed flow”. In: *Experiments in fluids* 17 (1994), pp. 205–208.

[37] Sidney Leibovich. “The structure of vortex breakdown”. In: *Annual review of fluid mechanics* 10.1 (1978), pp. 221–246.

[38] Bernard Lewis. "Combustion". In: *Flames and Explosion of Gases* (1987).

[39] Bernard Lewis and Guenther Von Elbe. "Stability and structure of burner flames". In: *The Journal of Chemical Physics* 11.2 (1943), pp. 75–97.

[40] Ping Li. "Experimental Study on Flame Propagation Characteristics of Premixed Laminar Combustion of Hydrogen-rich Coke Oven Gas". In: *Journal of Physics: Conference Series*. Vol. 2247. 1. IOP Publishing. 2022, p. 012017.

[41] Edward James Long and Graham K Hargrave. "Experimental measurement of local burning velocity within a rotating flow". In: *Flow, turbulence and combustion* 86.3 (2011), pp. 455–476.

[42] Amy F Mielke et al. "Time-average measurement of velocity, density, temperature, and turbulence velocity fluctuations using Rayleigh and Mie scattering". In: *Experiments in fluids* 39 (2005), pp. 441–454.

[43] Sara Moein and Rajasvaran Logeswaran. "KGMO: A swarm optimization algorithm based on the kinetic energy of gas molecules". In: *Information Sciences* 275 (2014), pp. 127–144.

[44] Habib N Najm and Peter S Wyckoff. "Premixed flame response to unsteady strain rate and curvature". In: *Combustion and Flame* 110.1-2 (1997), pp. 92–112.

[45] FT Nieuwstadt, Jerry Westerweel, and Bendiks J Boersma. *Introduction to Theory and Applications of Turbulent Flows*. Springer, 2016.

[46] Marcus Ó Conaire et al. "A comprehensive modeling study of hydrogen oxidation". In: *International journal of chemical kinetics* 36.11 (2004), pp. 603–622.

[47] Clavin P. "Dynamic behavior of premixed flame fronts in laminar and turbulent flows". In: *Progress in Energy and Combustion Science* 11 (1985), pp. 1–59.

[48] Frank L Pedrotti, Leno M Pedrotti, and Leno S Pedrotti. *Introduction to Optics*. Cambridge University Press, 2017.

[49] N Peters. "Length and time scales in turbulent combustion". In: *Turbulent Reactive Flows*. Springer. 1989, pp. 242–256.

[50] Norbert Peters et al. "Statistics of flame displacement speeds from computations of 2-D unsteady methane-air flames". In: *Symposium (International) on Combustion*. Vol. 27. 1. Elsevier. 1998, pp. 833–839.

[51] T Poinsot, T Echekki, and MG Mungal. "A study of the laminar flame tip and implications for premixed turbulent combustion". In: *Combustion science and technology* 81.1-3 (1992), pp. 45–73.

[52] S.B. Pope. *Turbulent Flows*. Cambridge University Press, 2000. ISBN: 9780521598866. URL: `https://books.google.com/books?id=i0hOOkyph6IC`.

[53] M. Raffel et al. "Particle Image Velocimetry - A Practical Guide". In: *Experimental Fluid Mechanics* (2018).

[54] Andreas Schäfer, John B Heywood, and Malcolm A Weiss. "Future fuel cell and internal combustion engine automobile technologies: A 25-year life cycle and fleet impact assessment". In: *Energy* 31.12 (2006), pp. 2064–2087.

[55] Joseph A Schetz and Allen E Fuhs. *Fundamentals of fluid mechanics*. John Wiley & Sons, 1999.

[56] Shazia Shukrullah et al. "PIV and statistical analysis of a swirling bed process carried out using a hybrid model of axial blade distributor". In: *Processes* 7.10 (2019), p. 697.

[57] Jose O Sinibaldi, Charles J Mueller, and James F Driscoll. “Local flame propagation speeds along wrinkled, unsteady, stretched premixed flames”. In: *Symposium (International) on Combustion*. Vol. 27. 1. Elsevier. 1998, pp. 827–832.

[58] Poinsot T. and Veynante D. *Theoretical and numerical combustion*. Philadelphia: Edwards, 2001.

[59] Cameron Tropea, Alexander L Yarin, and John F Foss. *Springer handbook of experimental fluid mechanics*. Springer Science & Business Media, 2007.

[60] Mark Jeroen Tummers. “Investigation of a turbulent wake in an adverse pressure gradient using laser Doppler anemometry”. In: (1999).

[61] Stephen R. Turns. *An Introduction to Combustion: Concepts and Applications*. McGraw-Hill, 2012.

[62] Faizan H Vance, LPH De Goey, and Jeroen A van Oijen. “Development of a flashback correlation for burner-stabilized hydrogen-air premixed flames”. In: *Combustion and Flame* 243 (2022), p. 112045.

[63] Arley Cardona Vargas et al. “Burning velocity of turbulent methane/air premixed flames in subatmospheric environments”. In: *ACS omega* 5.39 (2020), pp. 25095–25103.

[64] Sebastian Verhelst and Thomas Wallner. “Hydrogen-fueled internal combustion engines”. In: *Progress in energy and combustion science* 35.6 (2009), pp. 490–527.

[65] Qiang Wang, Rongrong Li, and Hua Liao. *Toward decoupling: Growing GDP without growing carbon emissions*. 2016.

[66] Mark P Wernet. “Particle displacement tracking applied to air flows”. In: *International Conference on Laser Anemometry*. NAS 1.15: 104481. 1991.

[67] Charles R Wilke. “A viscosity equation for gas mixtures”. In: *The journal of chemical physics* 18.4 (1950), pp. 517–519.

[68] Gersom Willems. “Unraveling Flashback Phenomena of Turbulent premixed Hydrogen-Natural Gas-Air Flames”. In: (2022).

[69] Yun-Chao Wu and Zheng Chen. “Asymptotic analysis of outwardly propagating spherical flames”. In: *Acta Mechanica Sinica* 28.2 (2012), pp. 359–366.

[70] Yutao Zheng, Lee Weller, and Simone Hochgreb. “3D Flame surface density measurements via orthogonal cross-planar mie scattering in a low-turbulence bunsen flame”. In: *Proceedings of the Combustion Institute* (2022).

[71] Jingyu Zhu et al. “Simultaneous PIV/LIF-PIV measurements and numerical simulation of liquid flow and ambient gas flow for transient diesel spray”. In: *Fuel* 309 (2022), p. 122211.

[72] Thorsten Zirwes. “Effect of stretch on the burning velocity of laminar and turbulent premixed flames”. In: (2016).

A

Appendix

Table A.1: Dutch Natural Gas (DNG) and air compositions considered for the calculation of mixture properties and equivalence ratio. Data for DNG is taken from [20]

Component	Mole percentage %	Mixture
CH_4	81.27	DNG
N_2	14.44	DNG
C_2H_6	3.73	DNG
Rest	0.6	DNG
N_2	78	Air
O_2	21	Air
Ar	1	Air

Table A.2: Molar masses and molar volume.

Parameter	Value
M_H	$1.008\,\text{g/mol}$
M_{H_2}	$2M_H$
M_C	$12.011\,\text{g/mol}$
M_N	$14.007\,\text{g/mol}$
M_{N_2}	$2M_N$
M_O	$15.999\,\text{g/mol}$
M_{O_2}	$2M_O$
M_{Ar}	$39.948\,\text{g/mol}$
R_{gas}	$8.314\,\text{Pa} \cdot \text{m}^3/\text{mol} \cdot \text{K}$
V_m	$\frac{R_{gas}T}{p}$

Correction for Standard Temperature and Pressure (STP)

Standard conditions:

$$T_{STP} = 273.15\,\text{K}$$

$$p_{STP} = 101325\,\text{Pa}$$

Table A.3: Density of various species.

Density of Species	**Expression**
ρ_{H_2}	$\frac{2M_H}{V_m}$
ρ_{CH_4}	$\frac{M_C+4M_H}{V_m}$
$\rho_{C_2H_6}$	$\frac{2M_C+6M_H}{V_m}$
ρ_a	$\frac{f_{N_2}/air\cdot M_{N_2}+f_{O_2}/air\cdot M_{O_2}+f_{Ar}/air\cdot M_{Ar}}{V_m}$

Table A.4: Composition of air.

Parameter	**Value / Expression**
f_{N_2}/air	0.78
f_{O_2}/air	0.21
f_{Ar}/air	0.01
Number of moles of air (normalized for 1 mol of O_2)	$\frac{f_{N_2}/air}{f_{O_2}/air}+1+\frac{f_{Ar}/air}{f_{O_2}/air}=4.76$
n_{aAIR}	$\frac{f_{N_2}/air}{f_{O_2}/air}$ N2 +1 O_2 +$\frac{f_{Ar}/air}{f_{O_2}/air}$ Ar

Table A.5: Composition of fuel.

Parameter	**Value / Expression**
$x_{DNG}+x_{H_2}$	1
$x_{CH_4}+x_{C_2H_6}+x_{N_2}$	1
x_{CH_4}	0.8187
$x_{C_2H_6}$	0.0373
x_{N_2}	$1-(x_{CH_4}+x_{C_2H_6})$

Using the Ideal Gas Law:

$$\begin{aligned} pV &= nRT & \text{for}\quad n=1 \implies pV &= RT \\ V &= Q\cdot t \implies pQt & &= RT \end{aligned}$$

Under unburnt conditions:

$$\frac{p_u Q_X}{RT_u}=\frac{p_{STP}Q_{X,STP}}{RT_{STP}} \implies Q_X = Q_{X,STP}\cdot\frac{T_u}{T_{STP}}\cdot\underbrace{\frac{p_{STP}}{p_u}}_{STP}$$

For equivalence ratio ϕ:

$$\begin{aligned} \phi &= \left.\frac{\dot{m}_f}{\dot{m}_a}\middle/\frac{\dot{m}_f}{\dot{m}_{a\,stoich}}\right. \\ &= \left.\frac{Q_f}{Q_a}\middle/\frac{Q_f}{Q_{a\,stoich}}\right. \\ &= \left.\frac{n_f}{n_a}\middle/\frac{n_f}{n_{a\,stoich}}\right. \end{aligned}$$

Flow Rates and Velocity

$$
\begin{aligned}
Q_u &= Q_a + Q_f;\\
Q_u &= A_u u\\
Q_f &= \frac{uA}{1 + \frac{1}{\phi\left(\frac{n_f}{n_a}\right)_{stoich}}}\\
Q_a &= \frac{uA}{1 + \phi\left(\frac{n_f}{n_a}\right)_{stoich}}\\
\dot{m}_u &= \dot{m}_a + \dot{m}_f;\\
\dot{m}_u &= \rho_u \times Q_u\\
\dot{m}_f &= \rho_f Q_f\\
\dot{m}_a &= \rho_a Q_a\\
\rho_u &= \frac{\rho_f Q_f + \rho_a Q_a}{Q_u}\\
\rho_f &= \rho_{H_2} x_{H_2} + \rho_{CH_4} x_{DNG} x_{CH_4} + \rho_{C_2H_6} x_{DNG} x_{C_2H_6}
\end{aligned}
$$

Using Wilke's method [67] for dynamic viscosity of the mixture (extension in current labview panel):

$$
\mu_u = \sum_{j=1}^{n} \frac{\mu_i}{1 + \frac{1}{x_i} \sum_{\substack{j=1\\ j\neq i}}^{n} x_j \phi_{ij}}, Re = \frac{\rho_u u D_i}{\mu_u}
$$

A.1. Calibration Target

Calibration plays the initiation role for high speed camera in PIV experiments as it establishes the initial spatial coordinate system, necessary for the consistency and accuracy of further calculations. This section elucidates the calibration process of our PIV experiment.

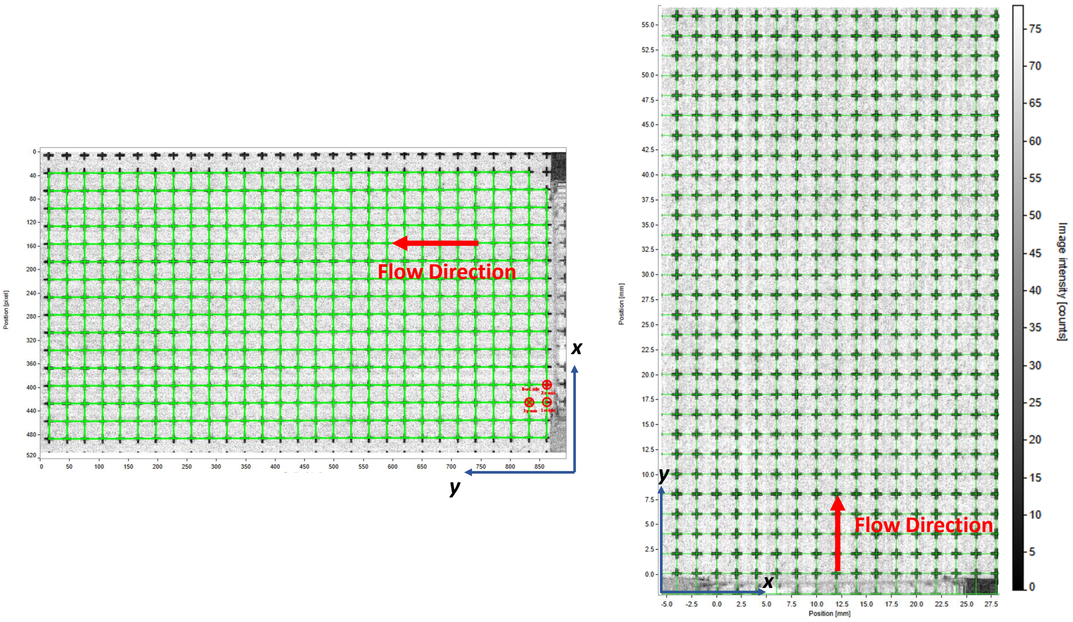

Figure A.1: Calibration Targets - (a) Initial Target: An image showing a square pixel by pixel calibration target. (b) Rotated and Metric-Spaced Target: A target rotated at a certain angle with defined metric spacing for calibration purposes.

As illustrated in Figure A.1, the calibration target comprises a grid of crosses, each 2mm long in both the horizontal and vertical dimensions with a spacing of 1mm in between. The target is initially represented in terms of $pixel$ spatial coordinates, a consequence of the sensor behind the camera lenses. In conventional conditions, the sensor possesses a resolution of 1024x1024 $pixel$. However, our experiment did not necessitate the use of the complete size of the sensor. We elected to crop the sensor resolution to 512x896 $pixel$ for both horizontal and vertical spacing, a size adequate for capturing the flame flow field under laboratory conditions. However, cropping the sensor eliminates unnecessary data on the field and enables more robust PIV post-processing. In our experiment, each pixel size corresponds to 20 micrometers. Consequently, the entire field approximates a size of 32x57.2 mm^2. After establishing the sensor size, the optical setup's magnification was approximated to be 1/3. This scale aids in capturing a more comprehensive view of the flame flow field without distorting the details. The final step of our calibration process involved intensity calibration, crucial for reducing the initial noise within the camera sensor. By calibrating the intensity of the sensor, aim was to improve the signal-to-noise ratio, leading to more reliable images. The calibrated system enabled us to capture accurate and reliable data from our PIV experiment, ensuring that subsequent calculations were based on a consistent spatial coordinate system.

A.2. Derivation of Particle Velocity Evolution in Stokes Flow

We consider the motion of small spherical particles in a fluid flow under Stokes' drag conditions. The equation of motion (force balance) for such a particle is:

$$m_p \frac{dV(t)}{dt} = F_d + F_g \tag{A.1}$$

Where:

- m_p is the particle's mass.
- F_d is the drag force.
- F_g is the buoyancy-corrected gravitational force.

For Stokes flow, the drag force F_d is:

$$F_d = 6\pi a\mu(U - V(t)) \tag{A.2}$$

Where U is the fluid velocity and $V(t)$ is the particle velocity. At terminal or steady-state velocity, $U = V_\infty$. Neglecting the gravitational force for small, nearly neutrally buoyant particles, we get:

$$m_p \frac{dV(t)}{dt} = 6\pi a\mu(V_\infty - V(t)) \tag{A.3}$$

Separating the terms and integrating:

$$\int \frac{dV(t)}{V_\infty - V(t)} = \int \frac{6\pi a\mu}{m_p} dt \tag{A.4}$$

This gives:

$$-\ln(V_\infty - V(t)) = \frac{6\pi a\mu}{m_p} t + C \tag{A.5}$$

Where C is the integration constant. Using the initial condition $V(0) = 0$:

$$C = -\ln(V_\infty) \tag{A.6}$$

Substituting for C:

$$-\ln(V_\infty - V(t)) = \frac{t}{\tau_p} - \ln(V_\infty) \tag{A.7}$$

Where the particle response time τ_p is defined as:

$$\tau_p = \frac{\rho_p a^2}{3\mu} \tag{A.8}$$

Which, considering $m_p = \rho_p \frac{4}{3}\pi a^3$, can also be written as:

$$\tau_p = \frac{m_p}{6\pi a\mu} \tag{A.9}$$

Finally, we solve for $V(t)$:

$$V(t) = V_\infty(1 - e^{-t/\tau_p}) \tag{A.10}$$

A.3. Optical Theory Background

The principles of optics form the bedrock of Particle Image Velocimetry (PIV), providing the means to visualize and track the motion of particles within a fluid medium. This technique unveils the complexities of fluid dynamics and their interactions with various components or structures. An optical system of PIV setup is determined by a plenty of parameters. Among these, the focal length of lenses plays a significant role as it is connected to the lens aperture which indicates amount of light income. To brighten the standard lens setup involving object and image planes, their orientation and distances - from the object to the lens and from the image to the lens. This underlying theory starts through the following focal length, a pivotal design parameter, is defined as:

$$f_{\#} = \frac{f}{D} \tag{A.11}$$

Here, $f_{\#}$ denotes the lens aperture size, which dictates the amount of light that can pass through the lens. A lower aperture setting allows more light, thereby augmenting the optical resolution [48]. Another essential parameter is magnification, which sets the ratio of image size to object size [10]. It can also be interpreted as the ratio of the distance from the object to the lens, to the distance from the image to the lens. The size of the aperture opening is closely related to the f-stop value, which characterizes the relative aperture size in a lens system. A smaller f-stop number, such as f/2.8, corresponds to a larger aperture opening, enabling more light to pass through and resulting in a shallower depth of field [26]. On the other hand, a larger f-stop number, such as f/16, indicates a smaller aperture opening, allowing less light and resulting in a greater depth of field.

Figure A.2: Apparture Size Opening

In the realm of Particle Image Velocimetry (PIV), it is customary to employ a magnification value of approximately 0.3. This particular value signifies a proportion where the size of the captured image is roughly one-third of the object size. In practical terms, this choice of magnification implies that the distance from the lens to the image is approximately three times the distance from the lens to the object. By adjusting for a magnification of approximately 0.3, one can successfully capture a suitable field of view that encompasses the necessary area of interest. Simultaneously, this magnification value ensures that particle details are adequately resolved with a desirable level of clarity. In essence, this magnification value strikes a harmonious balance between encompassing the required scene and obtaining sufficient detail for analysis purposes.

$$M = \frac{-y_i}{y_o} = \frac{s_i}{s_o} \tag{A.12}$$

By combining the relationships expressed in the two equations, we can establish a relationship known as the lens formula. The lens formula provides a comprehensive understanding of the behavior of light in a lens system. It states that the inverse of the focal length (f) is equal to the sum of the inverses of the object distance (s_o) and the image distance (s_i).

$$\frac{1}{f} = \frac{1}{s_i} + \frac{1}{s_o} \tag{A.13}$$

This lens formula plays a fundamental role in lens theory, enabling us to determine the position and characteristics of the image formed by the lens. It serves as a powerful tool for designing optical systems and understanding the relationships between object distance, image distance, and focal length. To further visualize these principles, a sketch illustrating the thin lens approximation is introduced immediately following the lens formula.

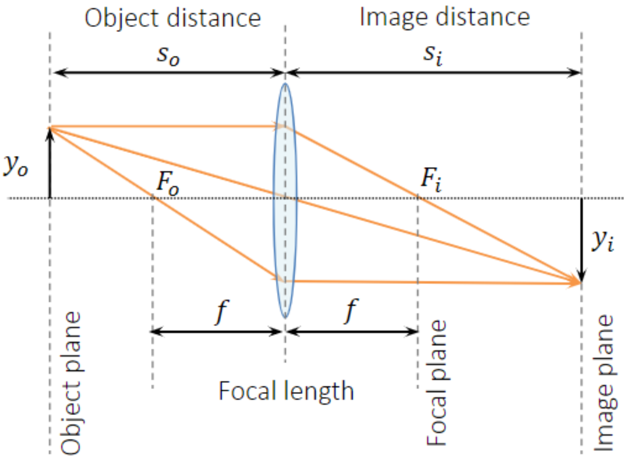

Figure A.3: Illustration of Thin Lens Approximation

This approximation simplifies the complexities of light refraction through the lens, and is integral to the derivation of several subsequent equations. Expanding upon these equations, we now address the geometric image of the particle (particle diameter), expressed as:

$$d_g = M d_p \tag{A.14}$$

This equation enables us to determine the size of the geometric image formed by the lens, where d_g represents the diameter of the image and d_p represents the diameter of the particle. Subsequently, we explore a key aspect of lens theory, the diffraction spot, which directly influences the optical resolution and the ability to identify particles in diagnostic experiments.

$$d_s = 2.44 f_{\#}(M+1)\lambda \tag{A.15}$$

Here, d_s refers to the diffraction spot of the geometric image, while λ symbolizes the wavelength of the visible optical spectrum. Incorporating the effects of both the geometric image and the diffraction spot, we can obtain a representation of the imaging of small particles. The total size of the image, denoted as d_{tot}, can be calculated using the following equation:

$$d_{tot} = \sqrt{(M d_p)^2 + (d_s)^2} \tag{A.16}$$

Through the application of convolution, above expression serves as a fundamental tool in quantifying the characteristics of the particle image.

A.4. Different Flame Front Detection Techniques

Besides, the accuracy of Mie-scattered flame visualization depends on interrogation window size. Figure A.4 illustrates the impact of varying the interrogation window size on the identification of the flame edge as per the number density method. The window sizes evaluated are wd = 24, 40, 56 pixels, corresponding to physical dimensions of 0.94, 1.57, and 2.20 mm, respectively. As the window size surpasses wd = 20, an increase in the window size results in a smoother flame edge due to a reduction in local variance. Although the spatial location of the flame edge does not significantly change as the window size increases from 24 to 56, a noticeable reduction in local curvature is observed. The selection of wd = 40, equivalent to 1.57 mm, optimally balances the accuracy of the flame edge location with the smoothness of the resulting curve.

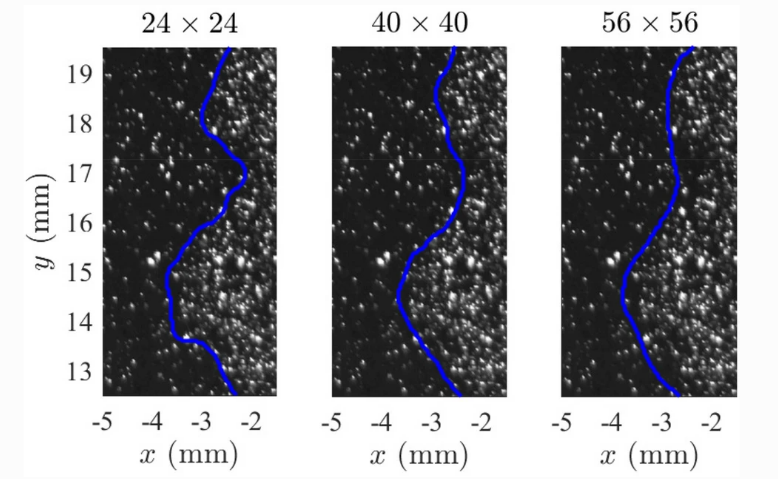

Figure A.4: Window Size Influence on Mie Scattering - A comparative study on the effects of window sizes of 24x24, 40x40, and 56x56 on Mie scattering results.

After investigating the influence of the interrogation window size, it becomes essential to delve into a comparative analysis with other prominent techniques for flame front detection, such as OH-PLIF. This comparative examination will furnish us with a nuanced understanding of the respective advantages and potential limitations of each methodology.

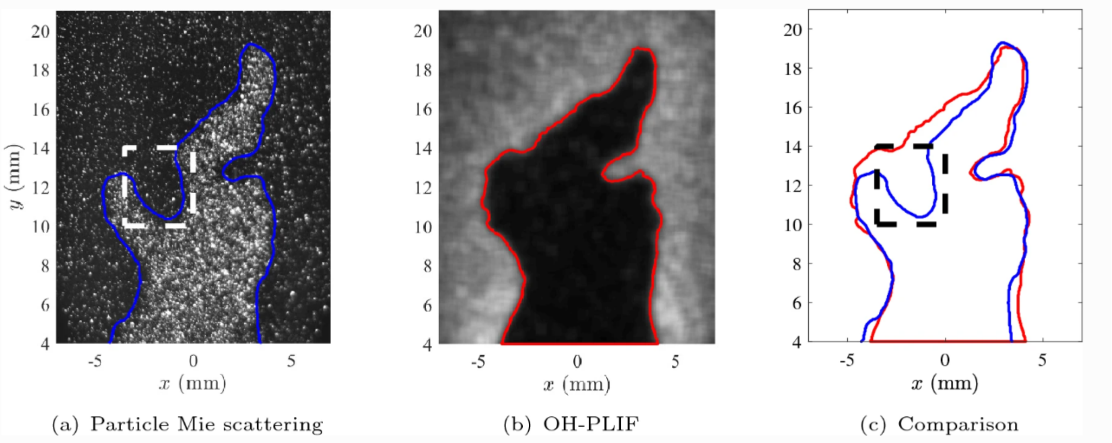

(a) Particle Mie scattering (b) OH-PLIF (c) Comparison

Figure A.5: Problem sample images obtained in case 1: a Single image of Mie scattering and edge using number density method with wd=40 pixels. b Single image of OH-PLIF using maximum gradient method with movmean filter 16×16 pixels. c Comparison of flame edges between (a) and (b)

Occasionally, disparities between the results from Mie scattering and OH-PLIF do emerge. For instance, one of the images showcases a concave shadow in the product region within the

Mie scattering area, corresponding to combustion products. This shadow is absent in the corresponding OH-PLIF signal where the same region suggests reactants instead. These variations may stem from the differing thicknesses of the laser sheets used in each technique. When the flame surface in the region of interest aligns almost parallel to the relatively thin OH-PLIF laser sheet, about 1 to 5 times thinner than its Mie scattering counterpart, the OH-PLIF image may just touch the interior of the reactant zone, resulting in a larger proportion of reactants. In contrast, the Mie scattering method, which averages particle density over a greater thickness, depicts lower particle density in the region. Such differences underscore some limitations of the Particle Image Velocimetry (PIV) method. To address these uncertainties, a possible solution could be to include a flame edge measurement on the horizontal plane to ascertain whether the flame surface overlaps with the vertical laser sheet, thereby resolving potential inconsistencies.

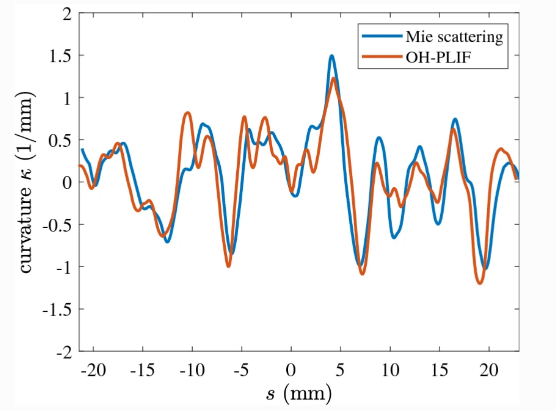

Figure A.6: Cubic Spline Curvature Comparison - An analytical comparison of results derived from Mie scattering and OH-PLIF techniques using cubic spline curvature.

Figure A.6 illustrates a substantial, but not complete, correlation between the two estimates. Across the entire flame, the absolute curvature values can still achieve a magnitude of $1.6\,mm^{-}1$, equating to a minimum radius of curvature of roughly 0.63 mm. Both curves in Figure A.6 exhibit curvatures that are less than $2mm^{-}1$, corresponding to the spatial resolution of OH-PLIF. Therefore, curvatures exceeding $2mm^{-}1$ are consequently diffused in both methodologies. This implies that when the center of curvature is located in the reactant side, the flame edges are identified more precisely using the number density methods. Conversely, the OH-PLIF technique performs better when the center of curvature is on the opposite side. An exception to this occurs when the flame edge extends into the reactant side. In these cases, OH-PLIF images tend to provide sharper detection of flame edges. In other words, the number density method excels in detecting sharp flame edges when the center of curvature is on the reactant side, whereas OH-PLIF shows a reversed behavior.

A.5. Background Theory of Bilatheral Filter

The filtered value of a pixel, denoted as $I_{\text{filtered}}(p)$, is obtained by taking a weighted average of the intensity values of its neighboring pixels within a filter window S. The weights are determined by two Gaussian functions, one that models the spatial distance between pixels and the other that models the tonal similarity between pixels. The bilateral filter can be expressed mathematically by starting the Spatial Gaussian function:

$$g_s(i,j) = exp(-\frac{||p-q||^2}{2\sigma_s^2}) \tag{A.17}$$

Where i, j are the pixel coordinates, p and q are the positions of the current pixel and its neighbors, σ_s is the standard deviation of the Gaussian function. The function $g_s(i,j)$ weights the contribution of the neighboring pixels to the filtered output based on their spatial distance from the current pixel.

$$g_t(i,j) = exp(-\frac{||I(p) - I(q)||^2}{2\sigma_r^2}) \tag{A.18}$$

In this equation, σ_r is the standard deviation of the tonal Gaussian function, and $I(p)$ and $I(q)$ represent the intensity values of the current pixel and its neighbors. The combined equation for the filtered value of a pixel with both the spatial and tonal Gaussian functions is:

$$I_{\text{filtered}}(p) = \frac{1}{W(p)} \sum_{q \in S} g_s(i,j) g_t(i,j) I(q) \tag{A.19}$$

The filtered value of a pixel, denoted as $I_{\text{filtered}}(p)$, is obtained by taking a weighted average of the intensity values of its neighboring pixels within a filter window S. The weights are determined by two Gaussian functions, one that models the spatial distance between pixels and the other that models the tonal similarity between pixels. Normalization factor becomes:

$$W(p) = \sum_{q \in S} (||g_s(i,j) g_t(i,j)||) \tag{A.20}$$

In the context of flame front contour detection, the bilateral filter can effectively suppress noise while preserving the sharpness of the contour edges as mentioned above. The filter is applied to the flame front image to remove noise while maintaining the spatial and tonal information of the flame front. This enables accurate detection of the flame front contour, which is essential for initializing local analysis of flame front contour.

A.6. Local Flame Stretch Computation

The fundamental objective of this study is to quantify the tangential stretch along a flame front, providing insights into the degree of deformation experienced by the flame in the tangential direction. This measure's significance lies in its ability to highlight the flame's intricate dynamical behavior, especially how it is influenced by the surrounding flow field. With these segmented sections and the flow field at disposal, a process that involves interpolation a unique vector decomposition, and averaging is embarked upon to ultimately compute the tangential stretch. The data under consideration for this study consists of the coordinates of detected flame front segments. A crucial step in preparing this data for analysis involves visualizing the dataset and identifying key features that will contribute to the computation of tangential stretch.

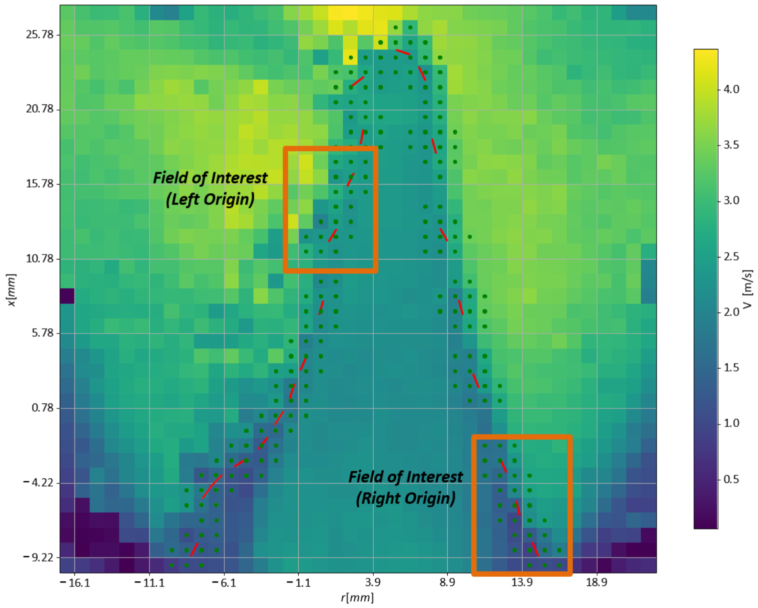

Figure A.7: Initial Velocity Mapping: The first rendition of velocity vector drawings, with a discussion on the significance of left and right origins to follow in the subsequent analysis.

As depicted in the Figure A.7, the flame front is represented by the selected segments from previous section with red linear lines. The green dots distributed across the field represent the grid cells where interpolation will be performed. A notable point is that the closest nine grid cells are identified for each endpoint of the flame front segments, setting the stage for the subsequent steps in the analysis. Central to the methodology of this study is the interpolation technique employed, specifically, cubic interpolation. This method allows the accurate computation of unknown values from a set of known data points.

A.6.1. Neighboring Cells with Interpolation

These nearest grid cells provide the basis for the calculation of velocity vectors, projection to tangential components, averaging, and, ultimately, the computation of tangential stretch. The utilization of cubic interpolation, coupled with the methods of vector projection and averaging, creates an accurate methodology for quantifying tangential stretch. To further elucidate the methodology and to demonstrate the applicability of the algorithm in different flame scenarios, two specific areas have been selected for detailed examination. These areas, indicated as the orange windows in the figure and referred to as the ’left origin’ and the ’right origin’, will serve as case studies. They are chosen to showcase how the algorithm performs on both the left and right sides of the flame.

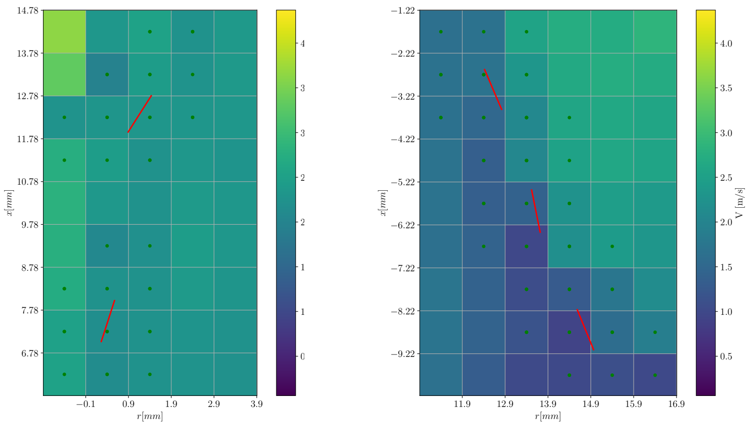

(a) (a) Left Origin **(b)** (b) Right Origin

Figure A.8: Neighboring Grid Detection: The detection process of adjacent grid cells on the flame front segment, depicted for both (a) left and (b) right origins.

The methodology for determining tangential stretch requires preparation and processing of grid cells. The initial step involves the identification of surrounding grid cells, depicted by the green dots in the associated Figure A.8. However, to isolate the effects of the unburnt flow properties on the flame front, it is necessary to filter out the grid cells that lie in the burnt region [72] [11]. This step aligns with the fundamental understanding that tangential stretch is influenced by the unburnt side of the flame, discussed in section 2.3, under flame stretch theory. To this end, the analysis incorporates a condition that eliminates grid cells in the burnt region from further calculations. These removed cells are represented by the color red in Figure A.9. This process effectively reduces the influence of burnt region dynamics, thereby ensuring that the calculated tangential stretch accurately reflects the influence of the flow conditions on the flame front before reaction occurs. This careful preparation of the grid cells lends credibility to the computation of the tangential stretch and the subsequent interpretation of results.

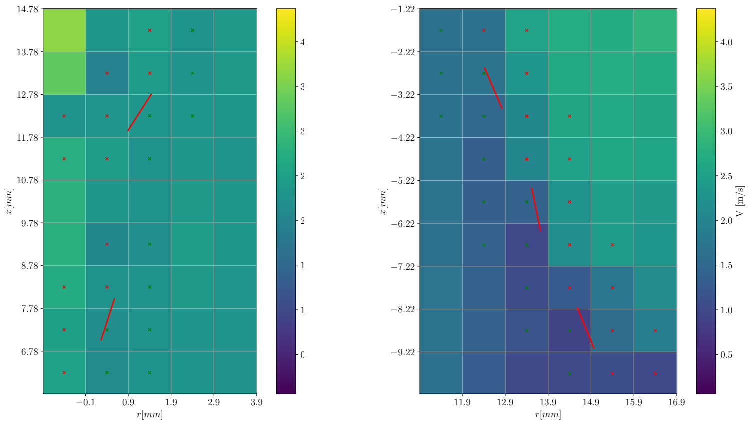

(a) (a) Left Origin **(b)** (b) Right Origin

Figure A.9: Burnt Side Elimination: Images showing the exclusion of the burnt side (depicted in red) with the accepted unburnt side remaining for (a) left and (b) right origins.

Velocity Vector Decomposition

The computation of velocity vectors is a key step following the data preparation and grid cell filtering. As shown in Figure A.10, the velocity vectors are computed at the green dot locations, i.e., the unburnt region. Each vector represents the direction and magnitude of the velocity at that specific grid cell. These vectors serve as a crucial input for the subsequent decomposition into tangential and normal components.

It is imperative to note an anomaly in this context: some vectors show discontinuity, failing to exhibit the expected smooth downstream propagation. Instead, these vectors appear to ”jump”, possibly due to their proximity to the burnt region, which influences their direction and magnitude. This issue signifies the need for further refining the data filtering process, ensuring only vectors truly representative of the unburnt region are incorporated in the subsequent analysis.

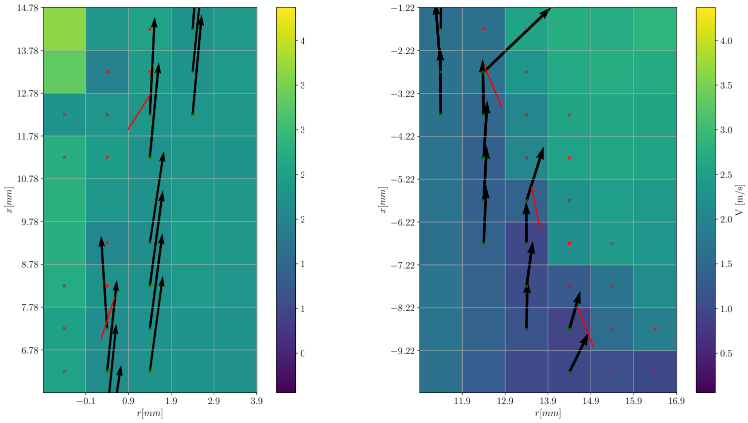

(a) (a) Left Origin

(b) (b) Right Origin

Figure A.10: Unburnt Side Velocity Vectors: Velocity vectors represented in the unburnt side, correlating to the neighboring cells for both (a) left and (b) right origins.

Following the computation of velocity vectors, their decomposition takes place. Each vector is decomposed into tangential and normal components with respect to the flame front segment. As shown in Figure A.11, the tangential component of the velocity vector, represented by blue arrows, aligns with the flame front segment, while the normal component, depicted by white arrows, is perpendicular to the flame front segment. This decomposition process is initiated by defining the flame front segments as unit vectors. Consequently, the parallel components of the velocity vectors can be calculated in the same direction as these unit vectors, with the orthogonal components falling perpendicular to them.

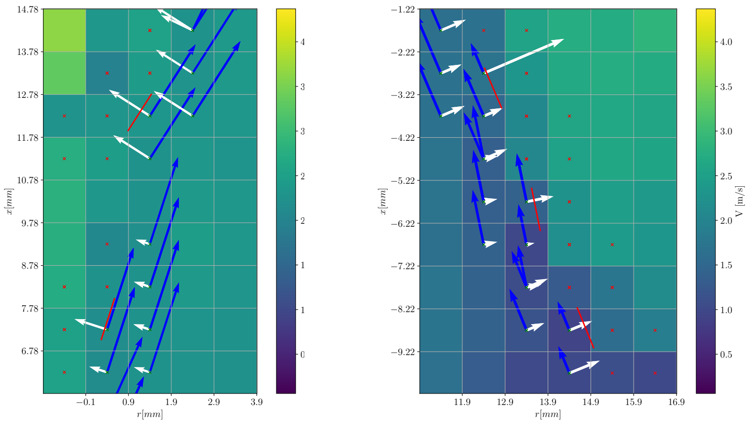

(a) (a) Left Origin

(b) (b) Right Origin

Figure A.11: Decomposed Velocity Vector Demonstration: A depiction of decomposed velocity vectors, with normal vectors in white and tangential vectors in blue, demonstrated for (a) left and (b) right origins.

The methodology employed in this study is centered around the computation of tangential velocities for each endpoint of a flame front segment. An integral aspect of this process is the averaging approach employed to determine these velocities. In this study, a straightforward arithmetic averaging is used, which offers a direct computation of the average from surrounding grid cells. After deducing the averaged tangential velocities at each endpoint of the flame front segments, the next step involves calculating the tangential stretch. This is determined by examining the difference in these velocities along the flame front segment and subsequently dividing by the length of the segment, set at 1mm for this study. This mathematical relationship can be expressed as:

$$K_t = \frac{\Delta \bar{V_t}}{\Delta x} \tag{A.21}$$

In this formula, K_t represents the tangential stretch. It's calculated by taking the difference ($\Delta \bar{V_t}$) in the averaged tangential velocities between the two endpoints defining the flame front segment and then dividing by the segment's length (Δx). The tangential stretch for each flame front segment provides a quantitative measure of the rate at which tangential velocity varies along the flame front. Gaining insights into this rate is crucial for comprehending the complex dynamics and behaviors of the flame front under differing circumstances.